Multi-junction solar cells and photovoltaic power converters: high-efficiency designs and effects of luminescent coupling

Matthew Wilkins

A thesis submitted to the

Faculty of Graduate and Postdoctoral Studies

in partial fulfillment of the requirements for the

Doctorate in Philosophy degree in Electrical Engineering

Ottawa-Carleton Institute for Electrical and Computer Engineering

University of Ottawa

Abstract

Multi-junction photovoltaic devices based on III-V semiconductors have applications in space power systems and terrestrial concentrating photovoltaics, as well as in power-over-fibre and optical power conversion systems. These devices have between two and twenty junctions arranged in tandem, connected in series with optically transparent tunnel diodes. In some cases, they may include as many as eight different materials, including ternary and quaternary alloys, and >100 epitaxial layers in total.

A general method for simulating performance of these devices using drift-diffusion based device simulation tools is reviewed. This includes discussion of the geometry, discretization, and physical equations to be solved. A set of material parameters for some important materials is listed, and solutions are shown for an example of a lattice-matched four-junction GaInP / (In)AlGaAs / InGaAsN(Sb) / Ge solar cell including a dilute nitride-based *p*-*i*-*n* junction with ~ 0.9 eV band gap.

A sample of this dilute nitride junction with a 650 nm absorber layer was grown by molecular beam epitaxy and was shown to have short-circuit current density of 15.1 mA/cm^2, sufficient for use in the 4-junction structure, while transmitting sufficient light through to the bottom (germanium) junction. Open-circuit voltage was up to 0.186 V at 1-sun, increasing to 0.436 V under 1500 suns concentration.

The device simulation methodology was extended to include effects of luminescent coupling and photon recycling. These effects are included by adding a term to the electron

and hole continuity equations, and the resulting coupled system of equations is solved. No external iterative loop is required, as has been the case in other efforts to model these effects. A five-junction photonic power converter (PPC) is simulated and it is shown that the quantum efficiency of the device is significantly broadened through luminescent coupling. There is a 350 mV reduction in simulated open-circuit voltage (70 mV per junction) if luminescent coupling is neglected. This work was later extended to a 12-junction PPC device, where the simulation predicts a wavelength sensitivity of -1.1%/nm in the absence of luminescent coupling; this is reduced to -0.4%/nm when luminescent coupling is included in the calculation. The latter result, and the overall shape of the simulated quantum efficiency curve agree closely with experimental measurements.

Finally, two specific applications of PPCs are demonstrated. The first is in a step-up DC-to-DC converter, where a linear regulator combined with a laser/PPC pair can convert a 3.3 V input (commonly available from a single lithium polymer battery cell) into 12 V. Unlike conventional switching boost converters, this 'photonic boost converter' is not a source of ripple. In testing, a >80 dB reduction in ripple was measured compared with an equivalent switching boost converter, limited only by input noise of the instrument.

The second application is in a 60 kW, 650 V switching circuit such as might be found in a hybrid or electric vehicle drivetrain. These circuits need several isolated power supplies to power gate drivers for the IGBT or SiC MOSFET switching components. This isolation is commonly provided by a small transformer, which inherently has a parasitic capacitance between primary and secondary windings and creates a path for EMI currents to flow from the high-power components to the power supply and control circuitry. By using a laser/PPC pair to provide the needed isolation, this parasitic capacitance can be largely eliminated; a 20 dB reduction in EMI current reaching the control FPGA is demonstrated.

Acknowledgments

I would like to extend my thanks to a number of people who have contributed and supported me in various ways during this work. Firstly, my parents and family who have been incredibly supportive over the past three years. I would like to thank my supervisor, Professor Karin Hinzer for her guidance and for encouraging and inspiring me to pursue the lines of inquiry that led to this thesis. I also owe both Karin Hinzer and Professor Henry Schriemer my gratitude for their generous support throughout my time at SUNLAB; they went to considerable personal effort to help me pursue my chosen career and for that I'm very grateful.

Thanks to Dr. James Gupta of the National Research Council Institute for Microstructural Sciences (NRC-IMS), who assisted with MBE growth of dilute nitride solar cells. At Université de Sherbrooke, Dr. Abderraouf Boucherif, Dr. Abdelatif Jaouad, Philippe-Olivier Provost, Dr. Boussairi Bouzazi and others assisted with fabrication and testing of the devices. Dr. Simon Fafard and Dr. Denis Masson of Azastra Opto Inc. allowed me to study their GaAs PPC devices which provided the best demonstration of luminescent coupling in multi-junction photovoltaics that I could have hoped for.

CMC Microsystems Inc. deserves special recognition for providing several important resources that helped to make this work possible. This includes arranging access to the simulation software tools used herein, loan of some invaluable pieces of test equipment which helped to make the experimental results as clear as possible, and also financial

support and assistance with epitaxial growth. Dr. Jessica Zhang at CMC was particularly helpful in making this collaboration happen. The value of these services – and the benefit that CMC provides to the scientific research community in Canada – cannot be overstated.

Dr. Christopher E. Valdivia has devoted an enormous amount of work to helping to edit these articles and make them as strong as possible. Finally, thanks to Dr. Joan Haysom, Mark Yandt, Dr. Alexandre W. Walker, Dr. Anna H. Trojnar and Dr. Ahmed M. Gabr and the remaining members of SUNLAB for their friendship and many helpful discussions.

Statement of Original Contributions

In this section I outline specific parts of the thesis which are original contributions to the field. Since this is a thesis by article, I will also clarify for each article the portion of work that was done by me and not by coauthors. In all cases, I was the main author of the text, and also planned and executed all experiments.

- Chapter 2: This chapter provides a background understanding of the operation of multi-junction solar cell devices, as well as an outline of how they are modeled using drift-diffusion based device simulators. It should provide a very good introduction to the technique, and also presents a table of all material parameters needed to simulate a four-junction GaInP / (In)AlGaAs / InGaAsN(Sb) / Ge solar cell. All text and figures were generated by me, and the modeling work was done by me. The theory that is presented is similar to that presented in a book chapter on simulation of multi-junction solar cells, authored by Matthew Wilkins and Karin Hinzer, to be included in *Handbook of Optoelectronic Device Simulation*, edited by Joachim Piprek and published by Taylor & Francis. It is planned for publication in 2017.

- Chapter 3: This chapter is a study of dilute nitride solar cell design, with a particular focus on the optimization for use in a 4-junction device. All simulation and design work prior to the growth and fabrication were performed by me. The epitaxial growth was done by James Gupta at the National Research Council Institute for

Microstructural Studies, and fabrication of finished device samples was done by the co-authors at Université de Sherbrooke, particularly Abdelatif Jaouad. I performed all AFM, EQE and *I-V* measurements. Other co-authors advised on the design of the solar cells and provided editing of the text.

- Chapter 4: This chapter presents a method for incorporating luminescent coupling effects in the simulation of multi-junction devices. It significantly improves on previously published methods by eliminating physical inconsistencies in the treatment of wave propagation in the layer stack; these inconsistencies would tend to both introduce error in the results and cause problems in the implementation of the algorithm. Additionally, the method integrates more cleanly with the device solver, eliminating the need for an iterative step in the solution process. I originally conceived of the modelling approach that is presented in this chapter, including the internal-source transfer matrix calculation and the method of integrating the resultant coupling factors into the device simulation through the nonlocal generation-recombination model interface in Sentaurus. I developed the theory which is presented in the appendix, implemented the code needed to execute the algorithm, and performed all modelling work. The devices in question were designed and fabricated by Simon Fafard and Denis Masson of Azastra Opto Inc.

- Chapter 5: This chapter applies the luminescent coupling model to explain the remarkably broad spectral response of 12-junction, monolithic photonic power converter (PPC) devices. Devices with so many junctions have never been studied previously in the literature, and they show very strong effects due to luminescent coupling. Again, all modelling work was done by me. An undergraduate student, Sanmeet Chahal assisted with quantum efficiency measurements under my supervision. These devices were also designed and fabricated by Simon Fafard and Denis

Masson of Azastra Opto Inc.

- Chapter 6: This chapter outlines two possible applications for PPCs in common electrical systems. I conducted all of the experiments and calculations, designed the two boost converter circuits shown, and wrote the text. Masanori Ishigaki conceived of the switching experiment and contributed the test circuit in Fig. 6.4. Christopher Valdivia contributed to results analysis and provided editing of the manuscript. Again, the PPC devices were designed and fabricated by Simon Fafard and Denis Masson of Azastra Opto Inc., and Pierre-Olivier Provost designed the coupled laser/PPC package.

List of Publications

Appearing in this thesis

1. **Matthew Wilkins**, James Gupta, Simon Fafard, Abdelatif Jaouad, Boussairi Bouzazi, Abderraouf Boucherif, Christopher E. Valdivia, Richard Arès, Vincent Aimez, Henry P. Schriemer, and Karin Hinzer. Design of thin InGaAsN(Sb) p-i-n junctions for use in 4-junction concentrating photovoltaic devices. *J. Photonics Energy*, pages 3–6, 2017.

2. **Matthew Wilkins**, Christopher E. Valdivia, Ahmed M. Gabr, Denis P. Masson, Simon Fafard, and Karin Hinzer. Luminescent coupling in planar opto-electronic devices. *J. Appl. Phys.*, 118(14):143102, 2015.

3. **Matthew Wilkins**, Christopher E. Valdivia, Sanmeet Chahal, Masanori Ishigaki, Denis P. Masson, Simon Fafard, and Karin Hinzer. Performance impact of luminescent coupling on monolithic 12-junction phototransducers for 12 V photonic power systems. In *Proc. SPIE 9743*, San Francisco, CA, 2016.

4. **Matthew Wilkins**, Masanori Ishigaki, Christopher E. Valdivia, Philippe-Olivier Provost, Denis Masson, Simon Fafard, and Karin Hinzer. Ripple-free photonic boost converter. Not yet accepted for publication. 2017.

Publications preceding the results featured in this thesis

5. **Matthew Wilkins** and Karin Hinzer. Multi-junction Solar Cells. In J. Piprek, editor, *Handbook of Optoelectronic Device Simulation*, chapter 40. Taylor & Francis, planned for publication in 2017.

6. Sanmeet Chahal, **Matthew Wilkins**, Denis P. Masson, Simon Fafard, Christopher E. Valdivia, and Karin Hinzer. 20-junction photonic power converter performance under non-uniform illumination calculated by 3D distributed circuit model. In *Proc. SPIE Photonics West 2017*, San Francisco, CA, 2017.

7. Simon Fafard, Mark C. A. York, F. Proulx, **Matthew Wilkins**, Christopher E. Valdivia, M Bajcsy, D. Ban, R. Ares, Vincent Aimez, K. Hinzer, M. Ishigaki, and Denis P. Masson. Ultra-efficient N -junction photovoltaic cell with V_{oc} >14 V at high optical input powers. In *IEEE Photovolt. Spec. Conf. 2016.*, pages 5–7, 2016.

8. **Matthew Wilkins**, A. M. Gabr, A. H. Trojnar, H. Schriemer, and K. Hinzer. Effects of Luminescent Coupling in Single- and 4-Junction Dilute Nitride Solar Cells. In *Proc. 40th Photovolt. Spec. Conf.*, pages 6–9, Denver, CO, 2014.

9. **Matthew Wilkins**, A. G. Gabr, P. Sharma, H. P. Schriemer, S. Fafard, and K. Hinzer. 4-junction solar cells with dilute nitrides: optimization with luminescent coupling. In *Proc. 29th EU PVSEC*, Amsterdam, NL, 2014.

10. **Matthew Wilkins**, Alexandre W. Walker, Jeffrey F. Wheeldon, Gilbert Arbez, Henry P. Schriemer, and Karin Hinzer. Design constraints of *n-p* InGaAsN dilute nitride sub-cells for 3- and 4- junction solar cell applications under concentrated illumination. In *Proc. 39th IEEE Photovoltaics Spec. Conf.*, Tampa, 2013.

11. S. Fafard, F. Proulx, M. C. A. York, **Matthew Wilkins**, C. E. Valdivia, M. Bajcsy, D. Ban, J. Jaouad, B. Bouzazi, R. Arès, V. Aimez, K. Hinzer, and D. P. Masson. Advances with vertical epitaxial heterostructure architecture (VEHSA) phototransducers for optical to electrical power conversion efficiencies exceeding 50 percent. In *Proc. SPIE 9743*, 2016.

12. Christopher E. Valdivia, **Matthew Wilkins**, Sanmeet S. Chahal, Francine Proulx, Philippe-Olivier Provost, Denis P. Masson, Simon Fafard, Karin Hinzer. Many-junction photovoltaic device performance under non-uniform high-concentration illumination. Abstract submitted to the CPV-13 conference, Ottawa, Canada 2017.

13. Christopher E. Valdivia, **Matthew Wilkins**, Boussairi Bouzazi, Abdelatif Jaouad, Vincent Aimez, Richard Arès, Denis P. Masson, Simon Fafard, and Karin Hinzer. Five-volt vertically-stacked, single-cell GaAs photonic power converter. In Alexandre Freundlich, Jean-François Guillemoles, and Masakazu Sugiyama, editors, *Proc. SPIE 9358*, volume 9358, page 93580E, 2015.

14. Karin Hinzer, Christopher E. Valdivia, **Matthew Wilkins**, Ross Cheriton, Pratibha Sharma, Anna H. Trojnar, Henry P. Schriemer, Boussairi Bouzazi, Gitanjali Kolhatkar, Abderraouf Boucherif, Abdelatif Jaouad, Simon Fafard, Vincent Aimez, Richard Ares, and James Gupta. Design Optimisations for Concentrated Solar Systems using Dilute nitride Four-junction Photovoltaics. In *Can. Semicond. Sci. Technol. Conf.*, Sherbrooke, QC, 2015.

15. S. Fafard, M. C. A. York, F. Proulx, C. E. Valdivia, **Matthew Wilkins**, R. Arès, V. Aimez, K. Hinzer, and D. P. Masson. Ultrahigh efficiencies in vertical epitaxial heterostructure architectures. *Appl. Phys. Lett.*, 108(7):071101, Feb 2016.

16. Ross Cheriton, **Matthew Wilkins**, Pratibha Sharma, Christopher E. Valdivia, Anna H. Trojnar, Henry Schriemer, Karin Hinzer, James Gupta, Boussairi Bouzazi, Gitanjali Kolhatkar, Abderraouf Boucherif, Abdelatif Jaouad, Simon Fafard, Vincent Aimez, and Richard Arès. Design optimizations of InGaAsN(Sb) subcells for concentrator photovoltaic systems. *J. Vac. Sci. Technol. B*, 34(2):02M103, 2016.

17. Christopher E. Valdivia, **Matthew Wilkins**, Pratibha Sharma, Ross Cheriton, Anna H. Trojnar, Gitanjali Kolhatkar, Abderraouf Boucherif, Abdelatif Jaouad, Boussairi Bouzazi, Simon Fafard, Vincent Aimez, Richard Arès, and Karin Hinzer. Towards CPV Systems using Dilute Nitride-Containing 4-junction Solar Cells. In *Proc. CPV-11*, Aix-les-Bains, France, 2015.

18. Karin Hinzer, **Matthew Wilkins**, Anna H. Trojnar, and Alexandre W. Walker. Material selections for high-efficiency lattice-matched and metamorphic multi-junction solar cell designs. In *Int. Mater. Res. Soc.*, Cancun, Mexico, 2014.

19. K. Hinzer, **Matthew Wilkins**, A. H. Trojnar, P. Sharma, C.E. Valdivia, J.P.D Cook, J.E. Haysom, H. Schriemer, and A.W. Walker. High efficiency multi-junction solar cell designs and their Integration in high concentration Solar Systems. In *Photonics North 2014*, Montreal, Canada, 2014.

20. G. Arbez, A. Walker, **Matthew Wilkins**, J. F. Wheeldon, R. Li, A. Trojnar, K. Hinzer, and H. Schriemer. 4 Junction Dilute Nitride Solar Cell Optimization: Comparing Current Matching Approaches in Detailed Balance Algorithms. In *Proc. 39th Photovolt. Spec. Conf.*, Tampa, FL, 2013.

21. Pratibha Sharma, **Matthew Wilkins**, Henry P. Schriemer, and Karin Hinzer. Modeling nonuniform irradiance and chromatic aberration effects in a four junction solar cell

using SPICE. In *2014 IEEE 40th Photovolt. Spec. Conf.*, pages 3293–3297, Denver, CO, June 2014.

Contributions not directly related to this thesis

22. Pratibha Sharma, **Matthew Wilkins**, Henry P. Schriemer, and Karin Hinzer. Concentrating optical system optimization for 3- and 4-junction solar cells: Impact of illumination profiles. *J. Photonics for Energy*, 7(1):014501, 2017.

23. Pratibha Sharma, **Matthew Wilkins**, Henry P. Schriemer, and Karin Hinzer. Optimization of three and four junction solar cell CPV systems using ray tracing and SPICE modeling. In *2015 IEEE 42nd Photovolt. Spec. Conf. PVSC 2015*, 2015.

24. A. W. Walker, O. Thériault, **Matthew Wilkins**, J. F. Wheeldon, and K. Hinzer. Tunnel-Junction-Limited Multijunction Solar Cell Performance Over Concentration. *IEEE J. Sel. Top. Quantum Electron.*, 19(5):4000508, 2013.

25. Pratibha Sharma, Anna H. Trojnar, **Matthew Wilkins**, Alexandre W. Walker, Henry Schriemer, and Karin Hinzer. Comparative Analysis of Nonuniform Illumination and Chromatic Aberration. In *29th Eur. Photovolt. Sol. Energy Conf. Exhib.*, pages 3–7, Amsterdam, NL, 2014.

26. Abderraouf Boucherif, Abdelatif Jaouad, Ross Cheriton, Shuo Han, **Matthew Wilkins**, C. E. Valdivia, Joan E. Haysom, Karin Hinzer, Simon Fafard, Vincent Aimez, and Richard Arès. GaAs solar cells on mesoporous silicon templates. In *Proc. CPV-11*, Aix-les-Bains, France, 2015.

27. Ahmed M. Gabr, Anna H. Trojnar, **Matthew Wilkins**, Trevor J. Hall, Rafael N. Kleiman, and Karin Hinzer. Optimization of anti-reflection coatings for bifacial so-

lar cells with upconversion layers. In *2014 IEEE 40th Photovolt. Spec. Conf.*, pages 2230–2233. IEEE, June 2014.

28. Ross Cheriton, **Matthew Wilkins**, Abderraouf Boucherif, Joan E. Haysom, Richard M. Beal, Christopher E. Valdivia, Olivier Thériault, Alexandre W. Walker, Abdelatif Jaouad, Jeffrey F. Wheeldon, Vincent Aimez, Richard Arès, Trevor J. Hall, and Karin Hinzer. Design, simulation and characterization of gallium arsenide solar cells on silicon substrates. In *Proc. CPV-10*, Albuquerque, NM, 2014.

Contents

List of Acronyms

AFM	Atomic force microscopy
ARC	Anti-reflective Coating
BHF	Buffered hydrofluoric acid solution
CMOS	Complementary metal-oxide silicon
CPV	Concentrating photovoltaics
EMI	Electromagnetic interference
EQE	External quantum efficiency
FFT	Fast fourier transform
FW90M	Full width at 90% of maximum
FWHM	Full width at half of maximum
IGBT	Insulated gate bipolar transistor
IQE	Internal quantum efficiency
LC	Luminescent coupling
LED	Light emitting diode
LPC	Laser power converter
MBE	Molecular beam epitaxy
MDF	Model dielectric function
MJSC	Multi-junction solar cell

MOCVD	Metal-organic chemical vapour deposition
MOSFET	Metal-oxide-silicon field effect transistor
PECVD	Plasma enhanced chemical vapour deposition
PMI	Physical model interface
PPC	Photonic power converter
PR	Photon recycling
SCM	Scanning capacitance microscopy
SPM	Scanning probe microscopy
SRH	Shockley-Read-Hall recombination
SSRM	Scanning spreading resistance microscopy
TCAD	Technology computer aided design
TE	Transverse electric field (polarization)
TM	Transverse magnetic field (polarization)
TMM	Transfer matrix method
VCSEL	Vertical cavity surface emitting laser
VEHSA	Vertical epitaxial heterostructure architecture

List of Symbols

h	Planck's constant
c	Speed of light
q	Electron charge
k	Boltzmann's constant
m_0	Electron mass
ϵ_0	Permittivity of free space
j	$\sqrt{-1}$

Solar cell fundamentals

E_{g}	Energy band gap
X	Concentration factor (relative to 1 sun)
P_{max}	Maximum power on the locus of an I-V curve
$E_{1-\mathrm{sun}}$	Optical intensity at 1 sun
J_{SC}	short-circuit current density
V_{OC}	open-circuit voltage
FF	Fill factor
J	Current density
I	Current

$J_{\text{ph},i}$	Photocurrent density in sub-cell i at 1 sun
$J_{0,i}$	Saturation current density in sub-cell i
V_i	Voltage across subcell i
$n_{\text{ideal},i}$	Diode deality factor for subcell i
T	Temperature
V	Voltage
η	Power conversion efficiency

Optics: Transfer matrix method

N	Number of material layers
m	Index of a specific layer. Layers 0 and $N + 1$ are the surrounding media, typically air.
z	Axis normal to the layer surfaces and interfaces
y	Axis transverse to the layer surface
$E^+_{m,\text{top}}$	y-component of electric field in layer m. 'Top' refers to field at top of the layer, '+' indicates the forward propagating wave (into the device)
$E^+_{0,\text{bot}}$	Phasor for wave incident on top surface of the device
$E^-_{0,\text{bot}}$	Phasor for wave reflected from top surface of the device
$E^+_{N+1,\text{top}}$	Phasor for wave emerging from bottom surface of the device
λ_0	Wavelength in external medium
θ_m	Angle of propagation
n_m	complex index of refraction
$k_{y,m}$	y-component of wave vector
d_m	Layer thickness

P_m	Propagation matrix for layer m
$t_{m-1,m}$	Fresnel transmission coefficient between layers $m-1$ and m
$r_{m-1,m}$	Fresnel reflection coefficient between layers $m-1$ and m
$\mathrm{T}_{m-1,m}$	Transmission matrix for interface of layers $m-1$ and m

Device physics

ϵ	Permittivity
A	Absorbed optical power per unit depth
G	Carrier generation rate
ϕ	Electrical potential
$\vec{P}$	Electrical polarization
n, p	Electron and hole concentrations, respectively
$N_\mathrm{D}, N_\mathrm{A}$	Donor and acceptor concentrations, respetively
$\vec{J}_n, \vec{J}_p$	Electron and hole current densities, respectively
R_net	Net recombination rate
μ_n, μ_p	Electron and hole mobilities, respectively
E_F	Fermi energy
$E_{\mathrm{F}n}, E_{\mathrm{F}n}$	Electron and hole quasi-Fermi energies
$E_\mathrm{C}, E_\mathrm{V}$	Conduction and valence band energies
E_g	Semiconductor band gap
$E_\mathrm{g,eff}$	Effective band gap including effect of band gap narrowing
$\mathcal{F}_{1/2}^{-1}$	Inverse Fermi-Dirac integral of order $1/2$
$N_\mathrm{C}, N_\mathrm{V}$	Conduction and valence band effective densities of states
F	Local electric field strength

Semiconductor material parameters

α, β	Varshni parameters for temperature dependence of band gap
T_{ref}	Reference temperature for Varshni parameters
$E_{\text{g,ref}}$	E_{g} at reference temperature T_{ref}
ΔE_{g}	Change in E_{g} due to band gap narrowing
χ	Electron affinity
χ_{ref}	Electron affinity at reference temperature T_{ref}
$\Delta\chi$	Change in χ due to band gap narrowing
m_n, m_p	Electron and hole density-of-states effective masses
$n_{\text{i,eff}}$	Effective intrinsic carrier concentration
μ_{min1}, μ_{min2}, P_{c}, μ_{max}, ξ, μ_1, α, β	Parameters for Masetti model of doping-dependent mobility
N_0, A_N, α_N, A^*, A_{a}, α_{a}, μ_{min}, A_{min}, α_{m}, μ_{d}, A_{d}, α_{d}	Parameters for Arora model of doping-dependent mobility
$R_{\text{rad}}, R_{\text{SRH}}, R_{\text{Auger}}$	Recombination rates via radiative, Shockley-Read-Hall, and Auger mechanisms
B_{rad}	Radiative recombination coefficient
γ_n, γ_p	Corrections to carrier concentrations, needed for Fermi-Dirac statistics
τ_{SRH}	Minority carrier lifetime for Shockley-Read-Hall recombination
τ_{min}, τ_{max}, N_{ref}, γ	Parameters used to calculate τ_{SRH}

E_{trap}	Energy of trap level relative to the intrinsic Fermi level
C_n, C_p	Auger recombination coefficients
R_{surf}	Surface/interface recombination rate
S_n, S_p	Electron and hole surface recombination velocities
R^{bb}	Recombination rate via band-to-band tunneling
A, F_0, σ	Material-dependent band-to-band tunneling parameters

List of Figures

CHAPTER 1

Introduction

Solar cells based on monocrystalline III-V materials hold overall records for power conversion efficiency at one-sun conditions and under concentration [1,2], due to a combination of properties: (1) materials are available with a variety of band gaps including in the range of 1.3-1.4 eV needed for maximum efficiency in a single junction [3,4]; (2) diffusion lengths are long relative to absorption length; and (3) many different materials can be grown lattice matched, allowing for engineered energy barriers within a device to contain generated carriers. The highest efficiencies are achieved in multi-junction solar cells consisting of a series of junctions operating in tandem. Recently these have been demonstrated with devices of 4, 5 or 6 junctions, each of a different material. The highest solar cell efficiency reported to date is 46.0% under 508 suns concentration [5], for a four-junction wafer-bonded structure employing GaInP, GaAs, GaInAsP and GaInAs junctions. The GaInP and GaAs junctions are grown on one wafer, while GaInAsP and GaInAs are grown on a second wafer of a different lattice constant. The wafers are bonded together to form a complete structure.

While concentrator photovoltaics (CPV) are now cost-effective in certain parts of the world where the cumulative direct normal irradiance is >2000 kWh/m^2/year [2,6] (in arid desert regions for example), Richard King *et al.* have argued that a cell-level efficiency

approaching 50% is needed to make CPV cost-effective when compared with other available energy sources in locations near major North American population centers [7]. King estimated achievable efficiencies for a series of different multi-junction structures [8]; as the number of junctions and the target efficiency increases, the material band gaps must be finely tuned in order to achieve an equal distribution of photogenerated current in the junctions [9, 10]. This leads to increasingly complicated designs which often include wafer bonds, transparent metamorphic buffer layers and quaternary alloys [7]. There is a clear need for new, high-quality materials to make these junctions, and also for simulation tools which are capable of accurately representing the physical processes at work in these devices, in order to be able to optimize designs for maximum energy conversion efficiency.

Alloys of InGaAs with dilute amounts of nitrogen (N) added have long been proposed as a suitable material for ~1 eV photovoltaic junctions lattice matched to GaAs [11]. In 2007 the first InGaAsN junctions with adequate performance to be integrated into a multi-junction device were reported [12], and in 2012 the overall record in solar cell efficiency was claimed by a GaInP/GaAs/InGaAsN(Sb) cell at 43.5% under high concentration [13].

Development of this material system continues, and improved growth techniques are leading to improved diffusion lengths [14–16]. Meanwhile through the mid-2000s, researchers at University of Ottawa and the National Research Council Institute for Microstructural Sciences (NRC-IMS) in Canada were successful in the development of InGaAsN dilute nitride materials for 1.3 to 1.55 μm laser diodes [17–19]. Chapter 3 of this thesis describes the application of these same materials developed at NRC to *p*-*i*-*n* junctions for solar cells.

A spinoff of III-V solar cell technology is multi-junction photonic power converters (PPCs), sometimes referred to as laser power converters (LPCs) or phototransducers. These are designed for monochromatic illumination and have recently been demonstrated with as many as 20 epitaxially grown GaAs junctions for an open-circuit voltage >23 V and

power conversion efficiency of 60% [20–22]. They are used in power-over-fiber (PoF) applications [23], and also with a direct coupling between laser and PPC.

Multi-junction solar cells, and even more importantly multi-junction PPCs, exhibit a phenomenon called 'luminescent coupling' where excess photocurrent in certain junctions is re-emitted as light and propagates to other junctions, equalizing light absorption within each of the junctions. Several articles published in 2012-2014 demonstrated that this effect is important for the efficient operation of solar cells, helping to reduce sensitivity to changes in the illuminating spectrum and also to process variations in thickness of the absorbing layers [24–27]. It also has implications for the optimal design of solar cells [28–31]. A related phenomenon, 'photon recycling', is the process where a subcell emits photons through radiative recombination, but they are re-absorbed in the same sub-cell before they can escape the device. This can also lead to higher device efficiencies than would be expected if the emissions due to radiative recombination escape from the device and are lost.

Generally, physics-based device simulators do not include the capability to model the effects of luminescent coupling and photon recycling within a drift-diffusion simulation. One publication in 2006 demonstrated the modeling of photon recycling in a drift-diffusion simulation of a single-junction solar cell [32], but the process required a time-consuming iterative loop where the simulator was run hundreds of times with successive approximations of the recycled photocurrent. More recently this technique has been applied to devices with two GaAs junctions [33]. Other simulations of photon recycling and luminescent coupling in photovoltaic cells have all been implemented with equivalent circuit models [34,35], using circuit simulators such as SPICE which do not provide insight into the internal operation of a device and do not allow for optimization of design parameters such as layer thicknesses. Evidently, in order to be able to model these luminescent coupling and photon recycling effects effectively in a device-level simulation, we require a method for incorporating the

effects into a drift-diffusion based device simulator, and ideally without adding an additional iterative loop to the simulation process. That development is a major focus of this thesis.

Concurrent with the development of this luminescent coupling modeling technique, the state of the art in PPC technology has been significantly advanced through developments led by Azastra Opto Inc. Until recently, multi-junction PPCs were typically designed as a single, planar *p*-*n* junction divided into segments through microfabrication (etched isolation trenches and conformal metallization to interconnect the junctions) [36–38]. Another approach involves a number of silicon *p*-*n* junction bars stacked by wafer bonding and illuminated from the side of the junctions [23]. This technology was demonstrated with a peak efficiency of 43%, but required a highly uniform source of illumination (<1% variation in intensity across the PPC).

Azastra Opto has developed a technology which it calls vertical epitaxial heterostructure architecture (VEHSA), where optically thin junctions are epitaxially grown in tandem in a manner similar to an MJSC. These results are reported in [20,21,39,40] and were supported by the device simulation techniques described here. A 5-junction GaAs PPC with open-circuit voltage of 6.2 V was demonstrated in 2014, followed by 6-, 12- and 20-junction devices in 2015 and 2016. These devices all have an optical-to-electrical power conversion efficiency of 60 to 65%, and can operate at much higher power densities than previous generations of devices [22]. They are also insensitive to nonuniform illumination, unlike the segmented and side-illuminated structures [38,41].

With these significant advances comes the possibility of applying PPCs in new applications. In particular, a laser diode coupled to a 12-junction PPC provides a step up in voltage while operating at DC. It also has a minimal stray capacitance between input and output. These qualities enable a floating, 12 V power supply with no ripple and high immunity to electromagnetic interference (EMI).

This work is organized as a series of published articles relating to the development

of advanced multi-junction photovoltaic devices. Chapter 2 provides background on the operation of single- and multi-junction solar cells and widely accepted simulation techniques used to study these devices. Based on simulations performed using those methods, Chapter 3 reports on the design and characterization of InGaAsN(Sb) dilute nitride solar cells, which could be a component in a lattice-matched 4-junction solar cell. Chapter 4 extends the simulation technique with the development of a method for incorporating luminescent coupling and photon recycling effects into semiconductor device simulations. The method is verified experimentally with 5-junction PPCs. In chapter 5 the luminescent coupling model is applied to 12-junction PPCs and it is demonstrated that these effects can be quantitatively predicted after calibrating to single-junction devices. Finally, chapter 6 proposes two applications of the PPC devices in power electronics systems.

Chapter 2

Background: Modeling of multi-junction solar cells

Matthew Wilkins

Some of the theory outlined here has been presented previously, though in a different form, in a book chapter to be included in 'Handbook of Optoelectronic Device Simulation' edited by Joachim Piprek and published by Taylor & Francis in 2017. In that chapter results for a 3-junction GaInP / (In)GaAs / Ge cell are presented.

Traditional solar cells with a single *p-n* junction have two major loss mechanisms, thermalization and transmission. Thermalization occurs as a photon is absorbed in a semiconductor and generates a free carrier with energy greater than the band gap E_g. The excess energy is quickly converted to heat and the carrier relaxes into thermal equilibrium with the free carrier population. Transmission losses occur as photons with energy less than E_g pass through the absorber material without being absorbed. These two competing loss

mechanisms result in an optimal band gap of ~ 1.3 eV [3,4]. In his book 'Third Generation Photovoltaics' in 2003 [42], Martin A. Green proposed that significant advancements in photovoltaic efficiency must come through development of solar cell technologies capable of avoiding these losses. These technologies include multi-junction (tandem) structures, intermediate-band materials, multiple-exciton generation, and hot-carrier cells. All of these have received significant research effort in the ensuing 14 years, however to date only multi-junction devices have realized significant improvement over single *p*-*n* junctions and have a demonstrated commercial market. Most devices which are commercially available today are lattice matched GaInP/(In)GaAs/Ge structures [43]. In space applications, GaInP/GaAs/InGaAs structures with a metamorphic buffer layer and a lattice-mismatched InGaAs junction are also well established. A three-junction lattice matched cell with a GaInP/GaAs/InGaAsN(Sb) structure has been demonstrated with 44% under concentration [44].

Efforts to improve cell efficiencies above the 44% mark generally are focused on larger numbers of junctions which further reduces thermalization and transmission losses, along with a reduction in current density which leads to reduced ohmic losses in the cell and metallization. These many-junction devices are very complex and require careful optimization to achieve their full potential efficiency. This chapter will outline some basic operating principles of multi-junction photovoltaic devices. Simulation can be used to perform these optimizations and study potential new designs. Simulation techniques based on the coupled drift-diffusion and Poisson equations are also discussed. Throughout the chapter, a hypothetical four-junction, lattice matched solar cell with a GaInP / Al(In)GaAs / InGaAsN(Sb) / Ge structure (Fig. 2.1) is used as an example. Some results from an earlier version of this model have been published elsewhere [45, 46], and were also used to inform the design of the devices presented in Chapter 3.

When photons are absorbed in a semiconductor they excite electrons from the valence

band into the conduction band, creating a population of minority carriers. These minority carriers diffuse throughout the cell; carriers which reach the depletion region at the p/n interface are collected by the built-in field of the junction and driven towards the contacts. An efficient single junction can have nearly perfect internal quantum efficiency, meaning that at short circuit every absorbed photon results in an electron collected at the contacts. High quality solar cells have an open-circuit voltage ~ 0.4 V less than E_g.

Under the low frequency conditions that are relevant for solar cells, a single p-n junction can be modeled as a diode in parallel with a current source representing the generated photocurrent $J_{ph,i}$. When several junctions are connected in series, the equivalent circuit is as shown in Fig. 2.1b. The model can be made more accurate by adding a second diode in parallel with each junction, as well as resistive elements [4]. For a given illumination, the maximum power, P_{max} that can be extracted from the cell can be stated as

$$P_{max} = J_{SC}\, V_{OC}\, FF, \tag{2.1}$$

where J_{SC} is the short-circuit current density, V_{OC} is the open-circuit voltage, and FF is the fill factor. The power conversion efficiency, η is

$$\eta = \frac{P_{max}}{X E_{1-sun}} = \frac{J_{SC}\, V_{OC}\, FF}{X E_{1-sun}}, \tag{2.2}$$

where E_{1-sun} is the reference intensity of illumination under 1-sun conditions, and X is the concentration factor relative to 1-sun.

If we neglect resistive effects, each of the junctions, indicated with a subscript i, follows the diode equation

$$J_i = X J_{ph,i} - J_{0,i}\left(\exp\frac{qV_i}{n_{ideal,i}kT} - 1\right) \quad \forall\, i, \tag{2.3}$$

where J_i is the current density through the junction. $J_{0,i}$ is the saturation current density, $n_{ideal,i}$ is the diode ideality factor, V_i is the potential difference across the junction, k is Boltzmann's constant and T is the temperature of the junction.

(a)

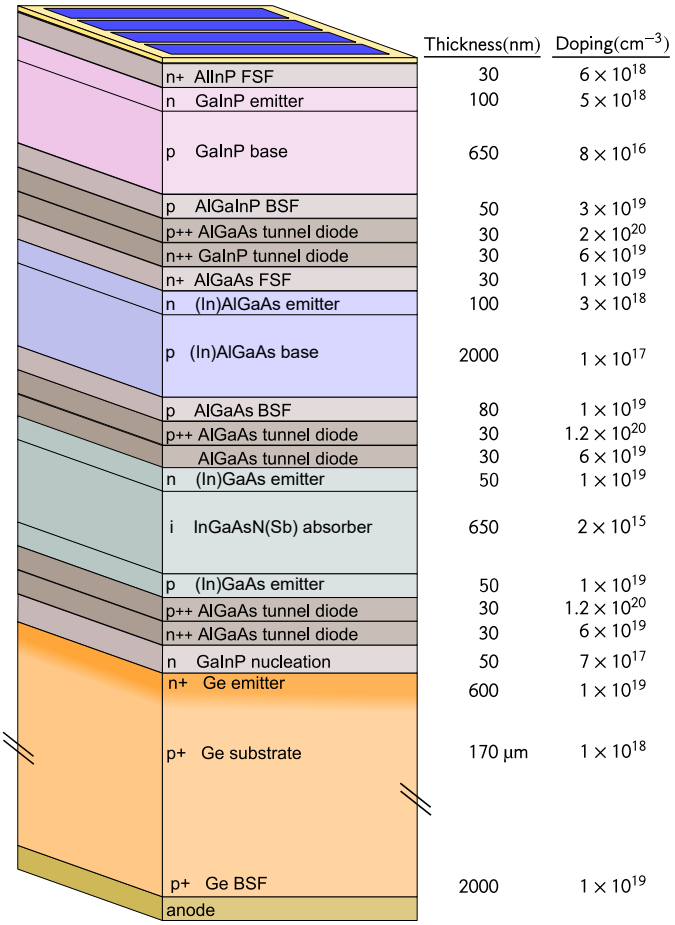

(b)

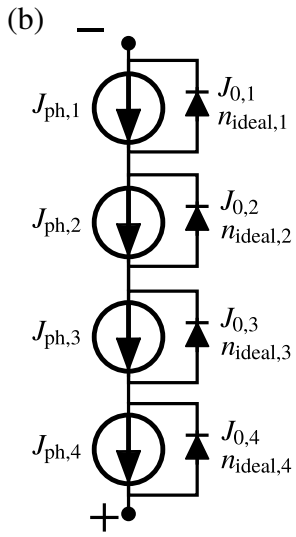

Figure 2.1: (a) Structure of the GaInP / Al(In)GaAs / InGaAsN(Sb) / Ge solar cell. (b) Lumped equivalent circuit model for the 4-junction cell.

As concentration increases, J_{SC} increases proportionately while V_{OC} increases as [8]

$$V_{OC} = \frac{kT}{q}\left[\sum_i n_{ideal,i} \ln\left(\frac{J_{ph,i}}{J_{0,i}}\right) + \ln X \sum_i n_{ideal,i}\right]. \tag{2.4}$$

The fill factor FF also tends to increase with concentration until the point where resistive losses become important. The overall effect is that the cell's power conversion efficiency η reaches a maximum; for multi-junction solar cells this is usually in the range of X=300 to 1200.

The four-junction example in this chapter, shown in 2.1a, could be grown epitaxially starting from a slightly ($\sim 2°$) miscut, p-doped Ge substrate. The thin, highly doped tunnel

diode layers are best grown in a metal-organic chemical vapour deposition (MOCVD) reactor, while the dilute nitride material InGaAsN(Sb) can only be grown with high quality in a molecular-beam epitaxy (MBE) reactor. For this reason, a three-step growth process is used for this structure.

In the first step, MOCVD is used to grow a lattice-matched GaInP layer on the Ge substrate. During the growth, phosphorous diffuses in the Ge, creating an n-doped region at the top of the substrate [47, 48]. Careful control of growth conditions is important at this stage to allow the III-V GaInP material to nucleate properly on the group-IV Ge material. The first (bottom) tunnel diode, consisting of degenerately doped n- and p-type AlGaAs, is also grown at this stage.

The second growth step involves use of an MBE reactor to grow the dilute nitride *p-i-n* heterojunction. Emitter and base layers are composed of (In)GaAs lattice matched to the Ge substrate; they provide the built-in voltage for the junction. The InGaAsN(Sb) dilute nitride absorber layer itself is undoped, maximizing diffusion length while allowing an electric field to form throughout the absorber. This electric field improves carrier collection, as dilute nitride materials frequently have a diffusion length shorter than the absorption length. As a result, dilute nitride cells cannot rely on diffusion alone to transport absorbed carriers to the space charge region of the junction. Besides providing built-in voltage, the base and emitter layers also form barriers preventing minority carriers from diffusing out of the absorber region. Effectively they serve the double duty of base/emitter and window layers.

The third growth step involves growth of the top two photovoltaic junctions, GaInP and (In)AlGaAs, along with the top two tunnel diodes. These two junctions are simpler in design, being made of materials with diffusion length greater than their respective absorption lengths, and are each clad with larger-band gap front-surface field (FSF) and back-surface field (BSF) layers.

Above the FSF of the top junction, a highly doped GaAs cap layer is grown, but etched

away everywhere except where the top gridlines and busbars are to be deposited. An anti-reflective coating (ARC) layer is deposited by chemical vapour deposition (CVD) in the etched areas, and metallic contacts are deposited on the top (cathode) and bottom (anode) of the wafer to form a complete cell. Finished solar cells for concentrating photovoltaic (CPV) applications are typically on the order of 5 mm × 5 mm in size, with a total of ~ 4 μm of epitaxial material on a 170 μm substrate.

Several techniques have been used to simulate multi-junction photovoltaic devices, including semi-analytic methods and equivalent-circuit models [4] as well as distributed-parameter models [49, 50]. Where a more detailed analysis is needed including as many physical processes as possible, and perhaps also two- and three-dimensional effects, a numerical solution of the coupled Poisson and drift-diffusion equations is a useful technique and can provide a great deal of insight into the operation of relatively complex devices. One of the first reports of a numerical simulation of a diode using the drift-diffusion model was by Scharfetter and Gummel with their analysis of an impact ionization avalanche transit-time (IMPATT) diode in 1968 [51]. Since then, the technique has been extended to include optical generation, Fermi-Dirac statistics, tunneling mechanisms, and a large variety of other physical phenomena. Bank, Rose and Fichtner in 1983 showed how the equations can be expressed robustly in three dimensions [52, 53] and that formulation is widely used to this day including in the simulation software (Synopsys Sentaurus) used for this work. Palankovski provides an overview of simulation of heterostructure devices [54]. Piprek's handbook offers an overview of simulations of many different optoelectronic devices [55, 56], and examples of solar cell simulations are avaiable from most of the simulation software vendors [57–59].

	J-V		**QE**
1.	Specify device geometry.	1.	Specify device geometry.
2.	Generate Mesh.	2.	Generate Mesh.
3.	Set material parameters in each region.	3.	Set material parameters in each region.
4.	Specify contact surfaces.	4.	Specify contact surfaces. Define internal 'virtual contacts' between subcells.
5.	Solve Poisson equation at equilibrium.	5.	Solve Poisson equation at equilibrium.
6.	Set zero bias; use Poisson solution for initial guess at electron & hole concentrations.	6.	Set zero bias; use Poisson solution for initial guess at electron & hole concentrations.
7.	Solve optical problem for generation rate profile. Repeat for all wavelengths in spectrum and sum contributions.	7.	Solve optical problem for generation rate profile at starting wavelength.
8.	Solve coupled Poisson and drift-diffusion equations.	8.	Solve coupled Poisson and drift-diffusion equations.
9.	Iterate step 8 with increasing bias.	9.	Iterate steps 7 & 8 with increasing wavelength.
10.	Post-processing: Plot contact current as a function of bias voltage.	10.	Post-processing: plot QE as a function of wavelength.

Table 2.1: General process for calculating *J-V* characteristics and quantum efficiency of multi-junction solar cells.

2.1 Device Geometry and Simulation Process

Multi-junction photovoltaics typically are a stack of thin, laterally uniform layers. The only features in the lateral directions are at the edges of the device, as well as the metal gridlines and busbars that are deposited on the top surface. The procedure needed to perform a device simulation is outlined in Table 2.1, for both current-voltage and quantum efficiency calculations. In both cases, the geometry of the simulation domain is defined, and material parameters including doping density are specified for each material region. The domain is discretized with a mesh density sufficient to accurately resolve all input and

output fields. An initial solution of the Poisson equation under equilibrium conditions is calculated, providing initial estimates of the electron and hole concentrations as a function of position in the device.

At this point, the procedures diverge. For the current-density calculation, the incident optical spectrum is used to calculate optical generation rate as a function of position, and ohmic contacts are defined at the cathode and anode. Starting from equilibrium, the coupled Poisson and drift-diffusion equations are solved repeatedly using the iterative Newton-Raphson method, with generation gradually increasing to the required level. The Newton-Raphson method requires an initial guess at the carrier concentrations, and works best when the guess is close to the final result. Ramping the intensity gradually permits the initial guesses for electron and hole concentrations and potential to be updated at each step so that the problem converges strongly. Finally, the voltage bias at the contacts is ramped to generate the data points of the J-V curve. Again, the initial guesses are updated at each step.

In the quantum efficiency calculation, ohmic contacts are defined at points between each subcell. All subcells are kept at short-circuit and the device is illuminated with a single wavelength. Again, intensity is ramped up gradually at the initial wavelength, and then wavelength is varied to cover the required range of wavelengths. The optical problem must be re-calculated at each wavelength.

2.2 Simplification and Discretization of the Simulation Domain

Rather than modeling the entire volume of a semiconductor device, the problem can usually be reduced to a smaller, representative element by taking advantage of symmetry and

periodicity in the structure. A typical solar cell with busbars along two edges and a series of thin gridlines in the perpendicular direction can be accurately represented with a model representing one quarter of the complete structure [60].

Further reductions in size of the problem can be made, at the expense of ability to model certain aspects of cell performance (Table 2.2). A two-dimensional model representing half of the device cross section will include most important phenomena, but cannot fully model perimeter recombination, the resistivity of gridlines and busbars, and the dark junction area under the busbar. An even smaller model representing just half of a single gridline and the illuminated area next to it is often used and can be a good compromise of model size and fidelity [32]. Finally, one-dimensional models are useful at early stages of design but ignore some important effects including emitter sheet resistivity [61]. 1D models can also overestimate recombination at the front contact, as its area is taken to cover 100% of the surface rather than ~3%.

An example of the 2D, semi-gridline mesh generated for the four-junction device is shown in Fig. 2.2. Mesh density is chosen such that the optical generation profile can be accurately resolved at all wavelengths; this means that the top of each absorbing region should have an element size less than the absorption length at the shortest wavelength of interest. High mesh density is also needed at the p-n junctions and tunnel diodes in order to resolve steep gradients in potential and carrier concentration. Towards the middle of a material region, where the conduction and valence bands are flat and concentrations are slowly varying, the mesh density may be driven by a need to resolve standing-wave oscillations in the optical intensity. There are discontinuities in the band edges and quasi-Fermi levels at heterointerfaces; consequently the mesh must include separate nodes for each region at the heterointerface boundaries. Quantities on each side of the boundary will be related with a boundary condition. Lastly, the areas at the edges of the top contact metal should be resolved so that the optical generation is properly resolved in the lateral direction.

Table 2.2: Limitations of reduced model geometries.

	1D	2D semi-gridline	2D one-quarter	3D
Nonuniform illumination			✔	✔
Shading due to gridlines		✔	✔	✔
ARC/window interface		✔	✔	✔
Grid ohmic losses				✔
Busbar regions			partial	✔
Emitter sheet resistance		✔	✔	✔
Nonuniform bias due to grid resistance				✔
p-n junctions and tunnel diodes	✔	✔	✔	✔
Perimeter recombination			partial	✔

2.3 Optical Generation

Most simulations of solar cells neglect the effects of photon recycling and luminescent coupling. In that case the rate of optical generation of carriers throughout the device is independent of the drift-diffusion problem, and so it can be calculated in advance. At longer wavelengths, multi-junction cells show significant etalon effects due to standing waves resonating in cavities formed by the layers of the upper sub-cells. For this reason a wave-based optical treatment is needed, rather than a simple Lambert-Beer law approach or raytracing which may be applicable in thick single junctions. Options include finite-

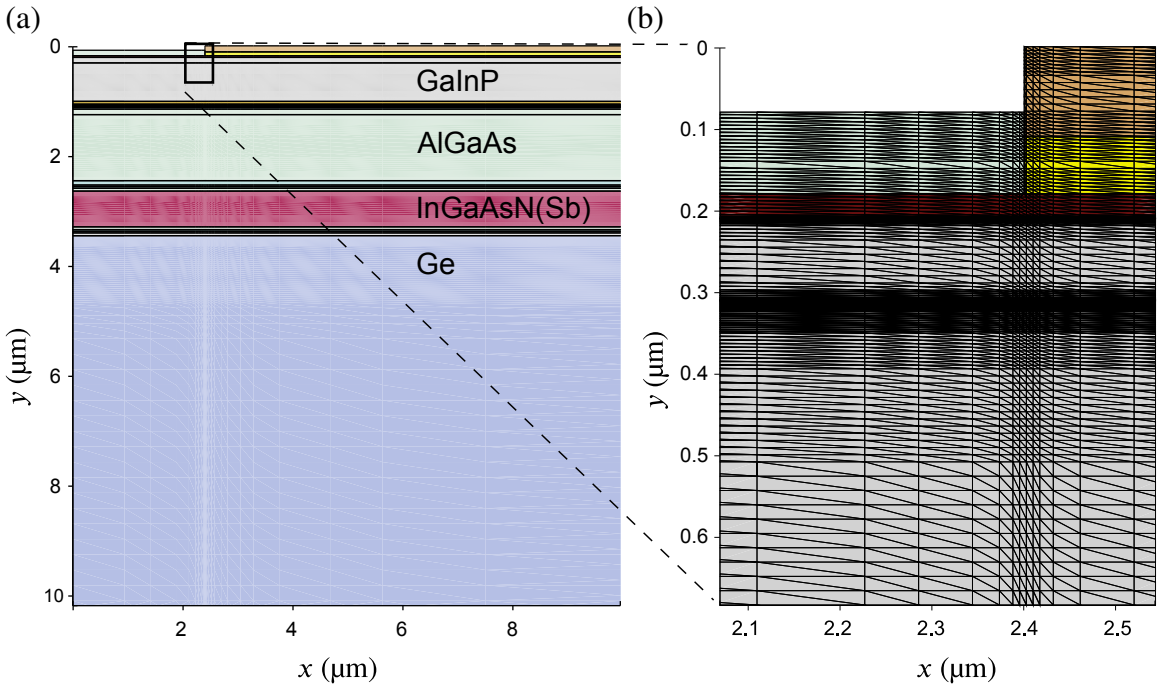

Figure 2.2: (a) A two dimensional, semi-gridline mesh for the four-junction solar cell. The full simulation region extends to 60 × 170 μm. (b) Detail of the area near the cathode.

difference time-domain simulation (FDTD) [60], rigorous coupled wave analysis (RCWA), and the transfer matrix method (TMM).

The finite difference time domain method involves a three-dimensional simulation of Maxwell's equations, integrated over time to determine the electric field propagating through space. Arbitrary geometries can be handled with this method, however it is a very expensive technique from a computational point of view and is generally avoided if other techniques are applicable. RCWA allows the treatment of layered structures which are patterned in the lateral dimensions, making it interesting for some nanostructured designs. It also may be suitable to model diffraction from gridlines and off-normal incidence illumination in planar solar cells, though these are minor considerations. This technique uses a truncated Fourier series approximation to represent the spatial variations in the lateral directions, while an exact treatment is used for the vertical direction.

TMM offers a 1D treatment of the wave propagation through the device, and can be set

up to illuminate only those areas not covered by the grid. It is well suited to the typical multi-junction solar cell (MJSC) structure with uniform planar layers of different materials and flat interfaces. The TMM is used throughout this work, and a full description of the calculation is included in the appendix to chapter 4.

Optical Material Properties

A major challenge in setting up a simulation of this type is the collection of suitable material properties. This is particularly true of the optical properties (i.e. complex refractive index, n), which must be specified as a table of data points over a range of wavelengths, approximately 300 to 2000 nm. While some materials such as GaAs and Si are very well characterized, many more exotic materials are proposed in MJSC designs and their properties may not be well known, or may be known only over a subset of the required wavelength range [62]. For GaAs, doping is known to change the extinction coefficient at wavelengths near the band edge [63] due to a combination of band gap narrowing and the Burstein-Moss effect [64]. Band gap narrowing is a reduction in the band gap that results from carrier-carrier interactions and carrier-dopant interactions, while the Burstein-Moss effect causes an increase in the apparent band gap as carriers fill up the lowest-energy states in the conduction and valence bands. Band gap narrowing prevails in heavily doped p-type GaAs and causes a red-shift in the absorption edge [64], while the Burstein-Moss effect prevails in n-type GaAs and causes a blue-shift in the absorption edge. $Ga_{0.49}In_{0.51}P$ lattice matched to Ge, which is often used as the top junction, can be grown with a variable amount of disorder and this has a significant effect on the optical properties, changing the absorption edge by as much as 0.1 eV.

Ternary and quaternary alloys with variable compositions can further complicate matters; one useful approach is to use empirical, parametric models for the variation of the

dielectric function with composition [65–70]. These model dielectric functions (MDF) are built up of a series of Lorentzian oscillators and other terms which are intended to represent the contributions to the dielectric function from each of the possible band-to-band transitions in the material. The parameters of these oscillators can be fitted as a function of material composition, allowing the composition to be varied continuously rather than using only those compositions where experimental data is available. A review of this work is covered by Djurišić *et al.* in [71]. Experience shows that these MDFs always include excessive absorption below the band gap and require some manual correction. Also, in some published results the fitting has been done in a way that puts very little weight on the quality of the fit near the absorption band edge. Any of these models should be evaluated by comparison with experimental data before using them.

References to the sources of optical properties used in the four-junction cell model are included in the appendix to this chapter.

Absorption and Carrier Generation Rate

With the optical problem solved using the TMM and the intensity as a function of position known, the absorbed energy density is written

$$A = -\nabla \left(\frac{1}{2} n^2 \epsilon_0 |\mathrm{E}|^2 \right), \tag{2.5}$$

where ϵ_0 is the vacuum permittivity and E is the local electric field amplitude.

For the III-V materials of interest here, we assume a unity quantum yield, meaning that 100% of absorbed photons yield free electron-hole pairs. This assumption could be invalid for very thick, highly doped layers where free-carrier absorption becomes significant. The generation rate is

$$G = -\frac{\lambda}{hc} \nabla \left(\frac{1}{2} \epsilon |\mathrm{E}|^2 \right). \tag{2.6}$$

The result is an exponentially decaying generation rate through the thickness of each absorbing layer. When the incident light has a broad spectrum, such as the solar spectrum as defined by the ASTM G173 standard [72], the optical calculation is repeated for each wavelength and the contributions are summed to find the broad-spectrum generation profile. The profile for the four-junction device, illuminated by an AM1.5D spectrum is shown in Fig. 2.3. As should be expected, the generation rate in each junction decays to nearly zero, meaning that the majority of photons with energy greater than the bang gap of that junction have been absorbed. The exception is the dilute nitride junction J3, which has been designed to allow some transmission into the Ge junction below it.

2.4 Semiconductor Material Properties

Material Band Structures

The purpose of this section is to outline all of the material parameters needed as input for device simulations of MJSCs including GaInP, AlGaAs, GaAs, InGaAsN and Ge junctions. Tables of all parameters and their values are included at the end of the chapter.

It is interesting to note that, while the band gaps and effective masses of most relevant materials are known to a high degree of accuracy, it wasn't until the early 2000s that the intrinsic carrier concentration, n_i of silicon was known to two significant digits of precision [73]. Altermatt argues that recombination rates are strongly dependent on the *effective* intrinsic carrier concentration $n_{\mathrm{i,eff}}$, and that for solar cell simulations it is more important to use a self-consistent set of parameters (a combination of band gap E_{g}, effective masses, m_n and m_p, a band gap narrowing model, and treatment of carrier statistics) that yield an accurate value of $n_{\mathrm{i,eff}}$ than it is to have any one of these correct in itself [74].

The intention here is to outline the physical models and parameters as they are used

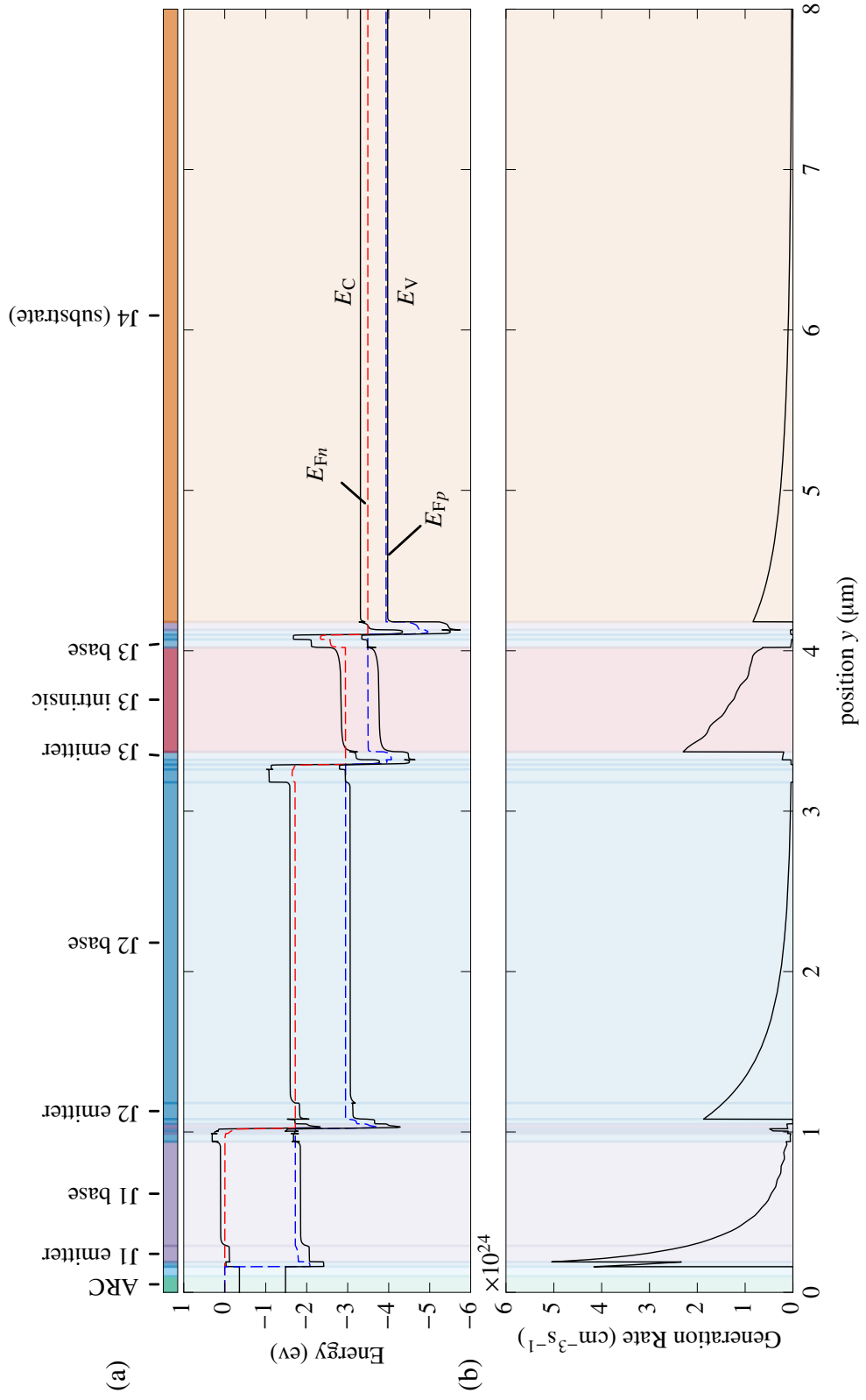

Figure 2.3: (a) Simulated band diagram at maximum power point for the four-junction solar cell. (b) Profile of optical generation rate through the depth of the four-junction solar cell, as calculated using the TMM. Illumination is broadband (AM1.5D spectrum) and uniform across the illuminated portion of the device.

in the device simulator, Synopsys Sentaurus Device, and so the information below closely follows that presented in the manual although it is simplified to cover exactly the set of physical models that were used in this work. Sentaurus Device derives $n_{\mathrm{i,eff}}$ from several other parameters [75]. First, the effective band gap is parameterized relative to the intrinsic band gap $E_{\mathrm{g,ref}}$ at a reference temperature T_{ref},

$$E_{\mathrm{g,eff}} = E_{\mathrm{g,ref}} - \frac{\alpha T^2}{T+\beta} + \frac{\alpha T_{\mathrm{ref}}^2}{T_{\mathrm{ref}}+\beta} - \Delta E_{\mathrm{g}}. \tag{2.7}$$

α and β are parameters for the Varshni temperature dependence of the band gap [76], and ΔE_{g} is the amount of band gap narrowing due to doping. The electron affinity, χ is parameterized in a similar way, as

$$\chi = \chi_{\mathrm{ref}} + \frac{\alpha T^2}{T+\beta} - \frac{\alpha T_{\mathrm{ref}}^2}{T_{\mathrm{ref}}+\beta} + \Delta E_{\mathrm{g}} \cdot \left(\Delta\chi/\Delta E_{\mathrm{g}}\right), \tag{2.8}$$

where χ_{ref} is the electron affinity at a reference temperature and the parameter $(\Delta E_{\mathrm{g}}/\Delta\chi)$ is the fraction of band gap narrowing that will be applied to the electron affinity. A value of $\Delta E_{\mathrm{g}}/\Delta\chi$=0.5 implies that half of the band gap narrowing will appear as a shift in the conduction band, and half will be applied to the valence band.

The conduction and valence band effective densities of states, N_{C} and N_{V}, respectively, are written as

$$N_{\mathrm{C}} = 2\left(\frac{2\pi m_n kT}{h^2}\right)^{3/2}, \tag{2.9}$$

$$N_{\mathrm{V}} = 2\left(\frac{2\pi m_p kT}{h^2}\right)^{3/2}, \tag{2.10}$$

where m_n and m_p are the density-of-states effective masses for the conduction and valence bands, respectively. The valence band density-of-states effective mass m_p combines contributions from degenerate light- and heavy-hole subbands. In indirect-gap semiconductors,

the effective mass for the conduction band m_n lumps together the density of states due to elliptical isopotential surfaces near the conduction band minima; in direct-gap semiconductors there is a single, spherical isopotential surface at the zone center.

The intrinsic carrier concentration can then be found from

$$n_{\mathrm{i,eff}} = \sqrt{N_{\mathrm{C}} N_{\mathrm{V}}} \exp \frac{-E_{\mathrm{g,eff}}}{2kT}. \tag{2.11}$$

This is the concentration of carriers in the conduction and valence bands of intrinsic material, due to thermal generation. Although we generally use Fermi-Dirac statistics to find carrier concentrations, intrinsic semiconductors are nondegenerate by definition and so eq. 2.11 applies.

Band Structures of Ternary and Quaternary Alloys

Multi-junction solar cells contain many alloys, including $\mathrm{In}_x\mathrm{Ga}_{1-x}\mathrm{As}$, $\mathrm{Al}_x\mathrm{Ga}_{1-x}\mathrm{As}$ and $(\mathrm{Al}_x\mathrm{Ga}_{1-x})_{0.5}\mathrm{In}_{0.5}\mathrm{P}$. The properties of these alloys can generally be interpolated from the binary compounds at the limits of the compositional range (i.e. at x=0 and x=1), using a quadratic interpolation [76],

$$E_{\mathrm{g}}(A_{1-x}B_x) = (1-x)E_{\mathrm{g}}(A) + xE_{\mathrm{g}}(B) - x(1-x)C. \tag{2.12}$$

Vurgaftman reviews the required parameters for a broad range of III-V compounds and alloys. Typically, it is best to apply this interpolation separately to each of the subbands of the conduction band (the valleys at the Γ, X and L points of the Brillouin zone) and find the temperature-corrected energy of each valley. The band gap of the semiconductor at any given composition is then the minimum of each of those valleys. The same formula can also be used to interpolate other parameters of the band structure, such as electron affinity and Varshni parameters.

Quaternary alloys can be treated in a similar way; for the $(Al_xGa_{1-x})_{0.5}In_{0.5}P$ material mentioned above we can simply use the ternary formula above with $Al_{0.5}In_{0.5}P$ and $Ga_{0.5}In_{0.5}P$ as compositional endpoints. For more general quaternary alloys, Vurgaftman offers several formulae depending on how the composition is stated [76].

Band Structure of Dilute Nitrides

The dilute nitride InGaAsN(Sb) alloy that is proposed here as the third absorber material of the four-junction cell cannot be treated using the method above [77]. The introduction of small concentrations of nitrogen (N), substituting for group-V atoms in a host InGaAs alloy, creates a new subband located just above the conduction band minimum. Interaction between this band and the conduction sub-bands of the host material has the effect of splitting the original conduction band in two. One of the newly formed bands is distorted and shifted downwards, making a smaller band gap for the material overall [78].

In his review of dilute nitride material band structures [79], Vurgaftman provides data on the shift in the conduction band energy as a function of nitrogen concentration, expressed using a band anticrossing model,

$$E_{\pm} = \frac{1}{2}\left(\left[E^C(k) + E^N\right] \pm \sqrt{\left[E^C(k) - E^N\right]^2 + 4V^2x}\right). \tag{2.13}$$

The E_- root of this expression is the newly formed, downward-shifted subband which forms the new conduction band minimum. $E^C(k)$ is the conduction band energy of the host material (i.e. InGaAs in this case), E^N is the energy of the nitrogen impurity level, and V is the interaction potential between the two bands and x is the nitrogen concentration. These last two parameters can be found in Table V of reference [79]. Although Sb is introduced in very small concentrations in the growth of this material, it is not expected to be incorporated into the material in any significant concentration. Instead, it remains on the surface of the

growing crystal and acts as a surfactant, improving the quality of the resulting InGaAsN material. For that reason, effects of Sb on the material properties are not considered.

Doping-Dependent Electron and Hole Mobilities

The doping dependence of electron and hole drift mobilities μ_n and μ_p are parameterized using one of two models, depending on what provides the best fit to experimental data and/or what can be found in the literature. The Masetti parameterization [80] has the form

$$\mu = \mu_{\mathrm{min1}} \exp\left(\frac{-P_{\mathrm{c}}}{N_{\mathrm{A}} + N_{\mathrm{D}}}\right) + \frac{\mu_{\mathrm{max}}\left(\frac{T}{300\ \mathrm{K}}\right)^{\zeta} - \mu_{\mathrm{min2}}}{1 + \left[\frac{N_{\mathrm{A}}+N_{\mathrm{D}}}{C_{\mathrm{r}}}\right]^{\alpha}} - \frac{\mu_1}{1 + \left[\frac{C_{\mathrm{s}}}{N_{\mathrm{A}}+N_{\mathrm{D}}}\right]^{\beta}}, \tag{2.14}$$

where N_{D} and N_{A} are donor and acceptor concentrations, and the remaining symbols (μ_{min1}, μ_{min2}, μ_{max}, μ_1, P_{c}, C_{r}, C_{s}, α, β, and ζ) are fitting parameters which can be found in the literature for many materials.

Alternatively the doping dependence of mobility can be fitted to the Arora model [81], which has four temperature-dependent factors,

$$N_0 = A_N \left(\frac{T}{300\ \mathrm{K}}\right)^{\alpha_N} \quad A^* = A_{\mathrm{a}} \left(\frac{T}{300\ \mathrm{K}}\right)^{\alpha_{\mathrm{a}}} \tag{2.15}$$

$$\mu_{\mathrm{min}} = A_{\mathrm{min}} \left(\frac{T}{300\ \mathrm{K}}\right)^{\alpha_{\mathrm{m}}} \quad \mu_{\mathrm{d}} = A_{\mathrm{d}} \left(\frac{T}{300\ \mathrm{K}}\right)^{\alpha_{\mathrm{d}}}. \tag{2.16}$$

Again, N_{D} and N_{A} are donor and acceptor concentrations and the remaining symbols are parameters which are specified separately for electrons and holes. Mobility is then calculated with

$$\mu = \mu_{\mathrm{min}} + \frac{\mu_{\mathrm{d}}}{1 + [(N_{\mathrm{A}} + N_{\mathrm{D}})/N_0]^{A^*}}. \tag{2.17}$$

Recombination Processes

With some basic material properties defined, we can now discuss recombination mechanisms. Again, this discussion follows the nomenclature of Synopsys Sentaurus, but similar theory can be found in [54] for example. The simplest mechanism is radiative recombination, where an electron recombines with a hole via photon emission. The rate of this process is given by

$$R_{\text{rad}} = B_{\text{rad}}(np - \gamma_n \gamma_p n_{\text{i,eff}}^2), \tag{2.18}$$

where B_{rad} is a radiative recombination coefficient which can be derived from the joint density of states of the conduction and valence bands and is tabulated in the appendix to this chapter. γ_n and γ_p are correction factors, defined as

$$\gamma_n = \frac{n}{N_{\text{C}}} \exp \frac{E_{\text{C}} - E_{\text{F}n}}{kT}, \tag{2.19}$$

$$\gamma_p = \frac{p}{N_{\text{V}}} \exp \frac{E_{\text{F}p} - E_{\text{V}}}{kT}. \tag{2.20}$$

They represent the relative difference in free electron and hole concentrations under Fermi-Dirac statistics, compared with the Boltzmann approximation. The $-n_{\text{i,eff}}^2$ term is intended to account for thermal generation, allowing the net radiative recombination rate to be zero at thermal equilibrium. Out of equilibrium however, if carrier concentrations reach the level where Pauli blocking is significant, then thermal generation must be inhibited by a reduction in available states; this is represented via the γ_n and γ_p factors.

Recombination via the Shockley-Read-Hall (SRH) mechanism has a characteristic lifetime which is dependent on the mean free path between interactions with impurities. Lifetime decreases, and recombination rate increases, strongly at higher doping levels. The lifetime is parameterized as

$$\tau_{\text{SRH}} = \tau_{\text{min}} + \frac{\tau_{\text{max}} - \tau_{\text{min}}}{1 + \left(\frac{N_{\text{A}} + N_{\text{D}}}{N_{\text{ref}}}\right)^{\gamma}}. \tag{2.21}$$

The recombination rate via the SRH process is then

$$R_{\mathrm{SRH}} = \frac{np - \gamma_n \gamma_p n_{\mathrm{i,eff}}^2}{\tau_{\mathrm{SRH},p}(n + \gamma_n n_1) + \tau_{\mathrm{SRH},n}(p + \gamma_p p_1)}, \tag{2.22}$$

with

$$n_1 = n_{\mathrm{i,eff}} \exp\left(\frac{E_{\mathrm{trap}}}{kT}\right), \tag{2.23}$$

$$p_1 = n_{\mathrm{i,eff}} \exp\left(\frac{-E_{\mathrm{trap}}}{kT}\right). \tag{2.24}$$

Again, γ_n and γ_p are used to correct for degeneracy which must be considered when using Fermi-Dirac statistics. E_{trap} is the energy level of the recombination centers relative to the middle of the band gap, and is usually near zero. In some devices with steep gradients at junctions, a more sophisticated recombination model using 'trap-assisted tunneling' may be more appropriate than SRH. This process works in a very similar way, but allows for some lateral motion (tunneling) of carriers as they transition between band edges and traps. With this model for a given carrier lifetime, the recombination rate can be significantly increased in regions where there is a strong electric field.

Auger recombination occurs where two carriers interact, with energy being transferred from one carrier into the other. This change in energy can excite a free electron to a higher potential within the conduction band, while the other loses enough energy to transition into the valence band. Because it requires three carriers (either two electrons and a hole or two holes and and electron), the Auger recombination rate is written

$$R_{\mathrm{Auger}} = (C_n n + C_p p)(np - \gamma_n \gamma_p n_{\mathrm{i,eff}}^2), \tag{2.25}$$

where C_n and C_p are capture coefficients for electrons and holes, respectively.

Finally, recombination at a surface or an interface can be stated in a very similar way to the SRH mechanism, with the lifetimes replaced with surface recombination velocities S_n

and S_p. The resulting rate is

$$R_{\text{surf}} = \frac{np - \gamma_n \gamma_p n_{\text{i,eff}}^2}{(n + \gamma_n n_1)/S_p + (p + \gamma_p p_1)/S_n}, \tag{2.26}$$

with n_1 and p_1 defined as for the SRH mechanism above. The resulting rate is defined only at interfaces, and has units of $\text{cm}^{-2}\text{s}^{-1}$, rather than $\text{cm}^{-3}\text{s}^{-1}$ as for the bulk recombination processes. Typical values for surface recombination velocities can be found in [82], or specific to MJSCs in [83].

Tunnel Diodes

Each of the photovoltaic *n*-*p* junctions are interconnected with $p++/n++$ tunnel diodes which are intended to provide an ohmic conductive path from the *p*-type base of one junction into the *n*-type emitter of the next junction [84]. Degenerate doping in the tunnel diode layers ensures that carriers can tunnel directly from the conduction band on the *n*-type side to the valence band on the *p*-type side with no change in energy [85]. In simulation, this is represented as an additional recombination process which is active only in the tunnel diode layers. More detail on simulating tunnel diodes can be found in [86–88].

2.5 Boundary Value Problem: Poisson and Continuity Equations

As described in section 2.1, the simulation begins with a solution of Poisson's equation under equilibrium conditions, which will serve as an initial guess for the coupled Poisson/drift-diffusion equations at non-equilibrium. Poisson's equation relates local charge density with variations in the electric field and potential [75]:

$$\nabla \cdot (\epsilon \nabla \phi + \vec{P}) = -q(p - n - N_{\text{A}} + N_{\text{D}}), \tag{2.27}$$

where ϕ is the electrostatic potential, $\vec{P}$ is the ferroelectric polarization and ϵ is static permittivity. $\vec{P}$ is generally zero for the materials considered here. In order to solve this equation as a boundary-value problem, we must state the charge density $\rho = q(p - n - N_A + N_D)$ in terms of the potential ϕ.

Relating the conduction and valence band energies E_C and E_V to the local potential,

$$\begin{aligned} E_C &= -\chi - q(\phi - \phi_{ref}) \\ E_V &= -\chi - E_{g,eff} - q(\phi - \phi_{ref}) \end{aligned} \tag{2.28}$$

where ϕ_{ref} is an arbitrarily chosen reference potential. Typically this is chosen to be the intrinsic Fermi potential of GaAs referenced to the vacuum level. Then using Fermi-Dirac statistics for the electron and hole concentrations, the quasi-Fermi levels for the electron and hole populations are

$$\begin{aligned} n &= N_C \mathcal{F}_{1/2}\left(\frac{E_{Fn} - E_C}{kT}\right), \\ p &= N_V \mathcal{F}_{1/2}\left(\frac{E_V - E_{Fp}}{kT}\right). \end{aligned} \tag{2.29}$$

At equilibrium, the quasi-Fermi levels are uniform throughout the domain and are equal to the Fermi level, $E_{Fn} = E_{Fp} = E_F$. We can arbitrarily set E_F to zero throughout the device and substitute (2.28) into (2.29). Then substituting (2.29) into (2.27), we have a self-consistent partial differential equation that can be solved numerically for the electrostatic potential profile (and carrier concentrations) at equilibrium. A charge neutrality boundary condition ($n - p = N_D - N_A$) is enforced in areas that are defined as 'ohmic' electrical contacts, and a homogenous Neumann boundary condition ($\nabla\phi = 0$) is enforced at non-contact boundaries.

Having found initial values of the potential and the carrier concentrations, the next step is to assemble a coupled set of equations describing electron and hole transport under non-equilibrium conditions. The continuity equations ensure that charge carriers are properly

accounted for,

$$\begin{aligned} \nabla \cdot \vec{J}_n &= qR_{\text{net}} + q\frac{\partial n}{\partial t}, \\ -\nabla \cdot \vec{J}_p &= qR_{\text{net}} + q\frac{\partial p}{\partial t}. \end{aligned} \tag{2.30}$$

where $\vec{J}_n$ and $\vec{J}_p$ are the electron and hole current densities, respectively, and R_{net} is the net recombination rate, including all recombination and generation processes. In steady-state solutions which are usually of interest for solar cells, the time derivatives will be zero. This includes recombination rates from radiative, Auger and SRH processes, minus the optical generation rate obtained from the TMM calculation. Within the tunnel diodes which connect each *p*-*n* junction, band-to-band tunneling is also included in R_{net}.

In its most general form, the drift-diffusion model in Sentaurus defines the electron and hole current densities as

$$\begin{aligned} \vec{J}_n &= \mu_n \left(n\nabla E_{\text{C}} - \frac{3}{2}nkT\ \nabla \ln m_n \right) + D_n \left(\nabla n - n\nabla \ln \gamma_n \right), \\ \vec{J}_p &= \mu_p \left(p\nabla E_{\text{V}} + \frac{3}{2}nkT\ \nabla \ln m_p \right) - D_p \left(\nabla n - n\nabla \ln \gamma_p \right) \end{aligned} \tag{2.31}$$

where D_n and D_p signify the diffusivities of electrons and holes. The equations in this form allow for drift currents due to variations in band gap and density of states. If the band gap and effective masses are constant throughout a region, the equations simplify to

$$\begin{aligned} \vec{J}_n &= -nq\mu_n \nabla\phi + D_n \left(\nabla n - n\nabla \ln \gamma_n \right), \\ \vec{J}_p &= -pq\mu_p \nabla\phi - D_p \left(\nabla p - p\nabla \ln \gamma_p \right). \end{aligned} \tag{2.32}$$

For low electric fields and non-degenerate semiconductors, the diffusivities can be related to the mobilities by the Einstein relation,

$$D = \frac{\mu kT}{q}, \tag{2.33}$$

however this does not hold under more general conditions. Lacking a more general model for the diffusivity though, in this work (2.33) is applied in all conditions. Applying (2.32)

with (2.30), we have a coupled set of three nonlinear partial differential equations in three variables, the potential ϕ and the carrier concentrations n and p.

$$\nabla \cdot \epsilon \nabla \phi = -q(p - n - N_{\mathrm{D}} - N_{\mathrm{A}}), \tag{2.34}$$

$$\begin{aligned} \nabla \cdot [-nq\mu_n \nabla \phi + D_n (\nabla n - n \nabla \ln \gamma_n)] &= qR_{\mathrm{net}}, \\ \nabla \cdot \left[-pq\mu_p \nabla \phi - D_p \left(\nabla p - p \nabla \ln \gamma_p\right)\right] &= qR_{\mathrm{net}}. \end{aligned} \tag{2.35}$$

These equations apply within the bulk of each material region, however there are discontinuities in the conduction and valence band energies at material interfaces. Consequently, the values of n, p and ϕ on each side of the interfaces are related with interface boundary conditions [82, 89].

The coupled set of equations can be discretized on the mesh, resulting in a set of nonlinear equations relating charge and recombination terms, which are integrated over a small volume, with flux terms crossing the volume boundaries. These equations can be solved by applying Newton's method using the initial guess which was found using the equilibrium Poisson solution. Because Newton's method is only expected to converge when the initial guess is very close to the final solution, it is advantageous to start with boundary conditions close to equilibrium and gradually increase them to the desired level, calculating new solutions (and a new initial guess for the next iteration) at each step.

A cross-sectional band diagram of the four-junction cell calculated using the drift-diffusion equations is shown in Fig. 2.3a, with the input optical generation in Fig. 2.3b. The incident intensity was 1000 suns with an AM1.5D solar spectrum. The potential boundary conditions at the contacts are set such that the device is biased at its maximum power point.

2.6 *J-V* Characteristics

The current-voltage characteristic (*J-V* curve) of a solar cell is calculated by solving the drift-diffusion problem at a series of bias voltages. Currents at the contacts are found by integrating the flux of electrons and holes across the contact surface. The net current is then the difference between the hole and electron currents; for a well-designed device the current of minority carriers reaching the contacts should be low.

It can also be useful to calculate *J-V* curves of individual subcells by defining 'virtual' ohmic contact boundary conditions at interfaces above and below the subcell of interest. Typically these contacts would be placed just above the front surface field layer, or just below the back surface field of the subcell in question. The solution is usually more stable if contacts are still defined at the top and bottom of the device. The current through the subcell in question is then the sum of currents at all of the contacts above it. *J-V* curves for the four-junction device and each of the subcells at 1000 suns, AM1.5D are plotted in Fig. 2.4a.

Some of the recombination processes which limit a subcell's open-circuit voltage V_{OC} have a distinctive voltage dependence [4]. For this reason, it can be useful to plot the dark *J-V* curve on a log-current axis (a Gummel plot). This is shown for each of the subcells in Fig. 2.4b. Additionally, the contributions to the *J-V* curve from individual processes can be calculated by integrating the recombination rates over the volume of a particular junction. For example the SRH recombination current density in junction i is

$$J_{i,\mathrm{SRH}} = \frac{q}{A}\int_i R_{\mathrm{SRH}} dV. \tag{2.36}$$

At steady state, the sum of all generation and recombination currents should equal the contact currents. A breakdown of recombination processes contributing the dark current density in the (In)AlGaAs subcell of the four-junction device is shown in Fig. 2.4c.

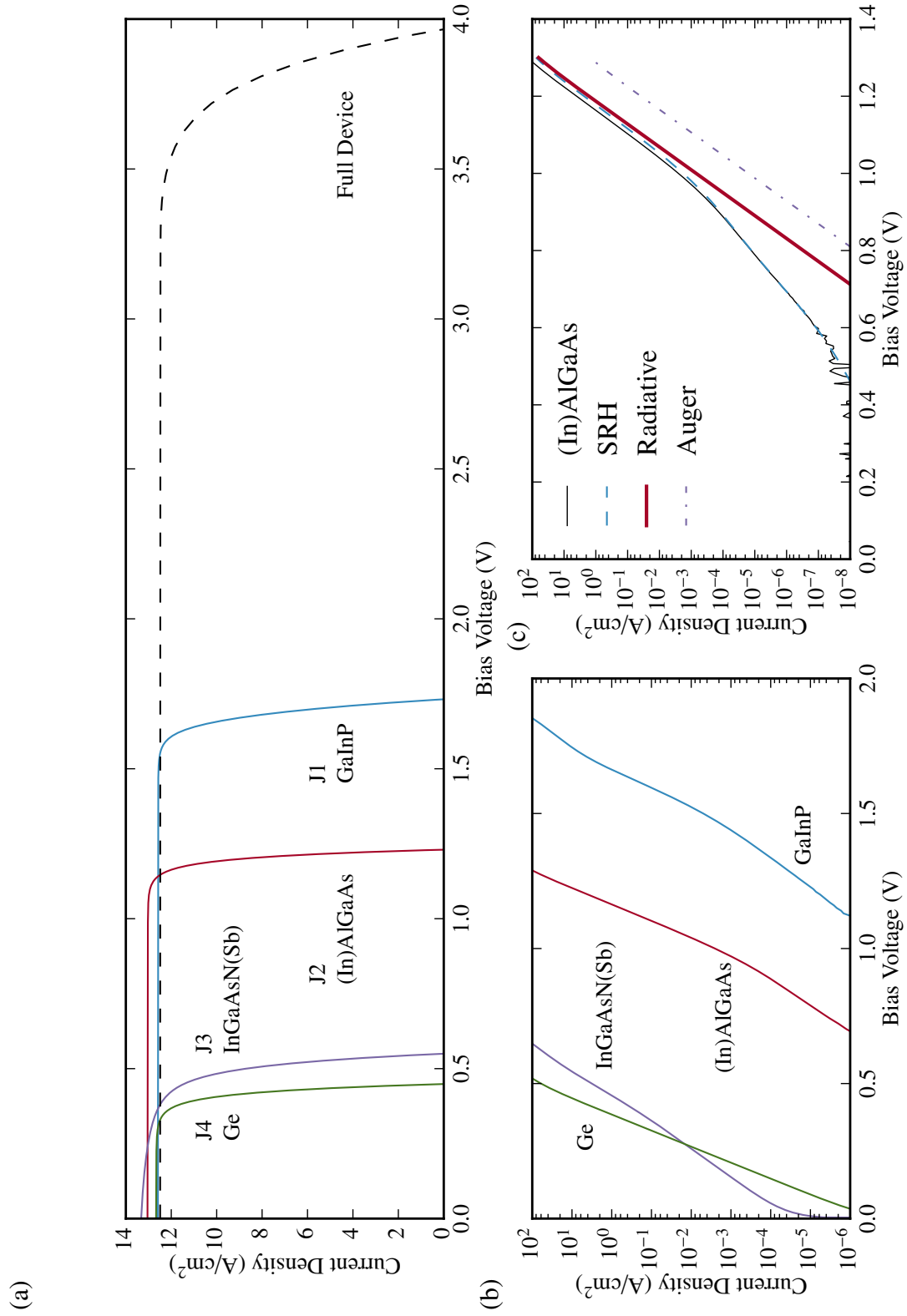

Figure 2.4: (a) J-V curves of the sub-cells and the four-junction device, extracted from simulations with illumination of 1000 suns, AM1.5D spectrum. (b) Dark current curves of each of the sub-cells. (c) Dark J-V curve of (In)AlGaAs with the contributions from individual processes.

Table 2.3: Extracted parameters of the J-V curves in Fig. 2.4.

	J1	J2	J3	J4	Full Device	
J_{SC}	12.6	13.05	13.3	12.67	12.5	A/cm^2
V_{OC}	1.73	1.23	0.55	0.45	3.97	V
FF	89.5	89.7	70.1	77.9	86.0	%
η	19.5	14.4	5.1	4.43	42.6	%

Finally, performance parameters can be calculated from the J-V curves: J_{SC}, V_{OC}, FF, P_{max} and power conversion efficiency. Invariably there will not be a data point calculated exactly at the maximum power point, so it must be interpolated using a fit to adjacent data points.

2.7 Quantum Efficiency

Quantum efficiency is a measure of the fraction of incident photons at a given wavelength which yield electrons collected at the device terminals. For a given incident photon rate $\Phi(\lambda)$, *External* quantum efficiency (EQE) is defined as

$$EQE(\lambda) = \frac{J_{SC}(\lambda)}{q\Phi(\lambda)}. \tag{2.37}$$

A related quantity is *internal* quantum efficiency (IQE). This latter term is usually defined in one of two ways. The first is as the ratio of *absorbed* photons to electrons,

$$IQE(\lambda) = \frac{J_{SC}(\lambda)}{q\Phi(\lambda)} \frac{1}{1 - R(\lambda) - T(\lambda)}, \tag{2.38}$$

where $R(\lambda)$ and $T(\lambda)$ are the reflectance and transmittance of the device. The quantity as defined in (2.38) is readily measurable, making it a useful way to characterize solar cells and compare with simulations while discounting losses due to reflectance and transmittance. With this definition, absorption mechanisms which do not yield electron-hole pairs, such as

absorption in an ARC layer or free-carrier absorption in the p-n junction layers, will result in reduced internal quantum efficiency.

The second definition is as the ratio of generated electron-hole pairs in the p-n junction to electrons

$$IQE(\lambda) = \frac{J_{SC}(\lambda)}{q \int G(\lambda) dV}. \tag{2.39}$$

IQE as defined in (2.39) is not directly measurable, but can be estimated through a combination of measurements of (2.38) and modeling of the other loss mechanisms. Because this definition excludes many non-ideal loss mechanisms, IQE of real devices as estimated with this definition can match predictions of semi-analytical p-n junction models such as in [4].

Quantum efficiency is also defined for individual subcells in a multi-junction device. Experimentally, it is measured by applying bias lights of wavelengths such that they are absorbed in all of the subcells except the one being measured [90]. This ensures that the subcell in question is limiting the overall current through the device. A probe beam from a monochromator is then scanned over all wavelengths of interest to produce the measurement. Unfortunately this method is not practical in the case of PPCs with >2 junctions absorbing in the same wavelength band, as it is impossible to bias the subcells independently.

In simulation, it is possible to replicate the conditions of the experiment as described above, however a simpler method is to introduce 'virtual contacts' in between subcells as described in section 2.6. This technique allows a single scan across the wavelengths of interest to produce results for all subcells, and is fully applicable to PPCs with many junctions.

Simulated subcell *EQE* and *IQE* for the four-junction device is shown in Fig. 2.5. Evidently *EQE* of the InGaAsN(Sb) junction is low; this is because it is so thin that it transmits a portion of the photons in its wavelength range through to the Ge junction. The reasons for this are discussed in chapter 3.

Quantum efficiency results as simulated using the method described here often show large Fabry-Perot type oscillations at wavelengths longer than the substrate bandgap. These oscillations do not appear in measurements, partly because the illuminating beam is not perfectly collimated in the experiment and partly because the monochromator has a finite wavelength resolution and is unable to resolve the <0.1 nm period of these oscillations. In order to be able to compare experimental results with simulations, we can convolve the simulated QE with a lineshape function $w(\lambda)$ representing the roughly triangular lineshape of the instrument. $w(\lambda)$ should be centered at zero and integrate to unity:

$$EQE_{\text{eff}}(\lambda) = \int_{-\infty}^{\infty} EQE(\lambda + l)w(l)dl. \tag{2.40}$$

Along with the experimentally measurable quantities R, T, EQE and IQE, device simulations can be used to calculate spectrally-dependent quantities which are internal to the device and cannot be directly measured. Each of the recombination rates can be integrated over the volume of a junction to give the component of QE loss due to that mechanism. The same can be done for parasitic absorption in non-active regions of the device. For example, the loss of EQE due to SRH recombination in the ith junction is

$$L_{\text{SRH},i}(\lambda) = \frac{1}{A\Phi(\lambda)} \int_{V_i} R_{\text{SRH}}(\lambda)dV. \tag{2.41}$$

Similarly for interface recombination at the interfaces above and below subcell i,

$$L_{\text{surf},i}(\lambda) = \frac{1}{A\Phi(\lambda)} \left(\int_{A_{\text{em},i/\text{fsf},i}} R_{\text{surf}}dA + \int_{A_{\text{base},i/\text{bsf},i}} R_{\text{surf}}dA \right). \tag{2.42}$$

In this case the integration is done over the emitter/front surface field and base/back surface field interfaces. The sum of all QE losses and all junction EQEs is unity. A breakdown of all losses in the four-junction simulation is shown in Fig. 2.6. Accounting for losses in this way makes it very clear where there may be room for improvement in a given

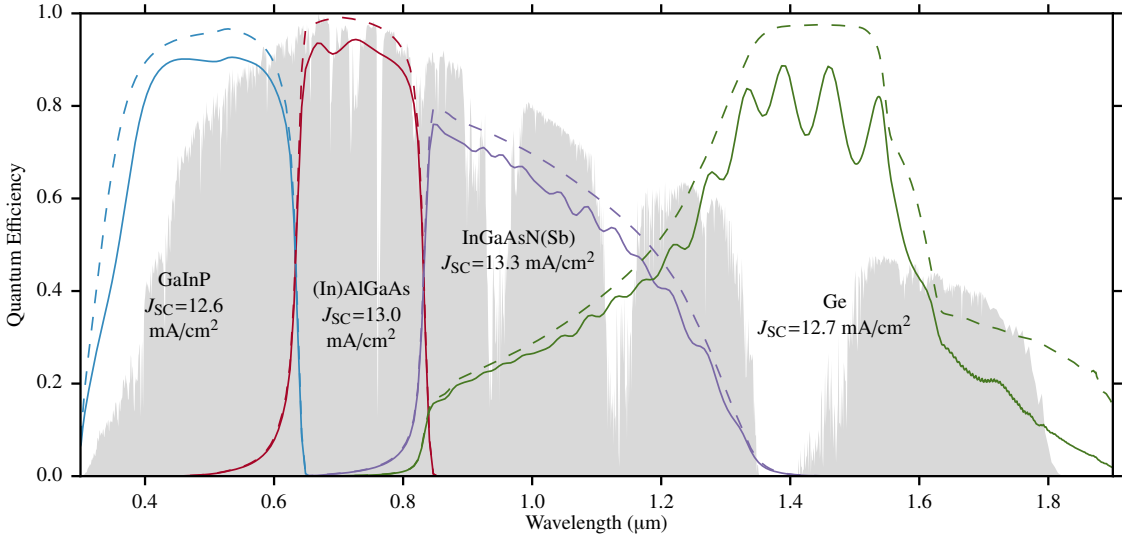

Figure 2.5: External (solid) and internal (dashed) quantum efficiency (EQE and IQE) of the four-junction solar cell. The normalized AM1.5D solar spectral irradiance is filled in the background. IQE is calculated using (2.38).

design. Although there is a sharing of photocurrent between the InGaAsN(Sb) and Ge junctions as noted earlier, the photons are collected efficiently overall; the only significant loss in the 1 to 1.4 μm range of wavelengths is reflectivity at <15%.

2.8 Summary

Current high-efficiency MJSC and PPC structures are often made up of six to ten different materials, with as many as 100 layers (in the case of a 20-junction PPC) and a similar number of heterointerfaces. Changes in the design of one junction can have impacts on the performance of other junctions, and so a comprehensive simulation of the entire device is important in order to maximize the efficiency of a given design.

Simulations are only as good as the input parameter set, and while a complete set of parameters are presented here based on data reported in the literature, efforts to grow actual

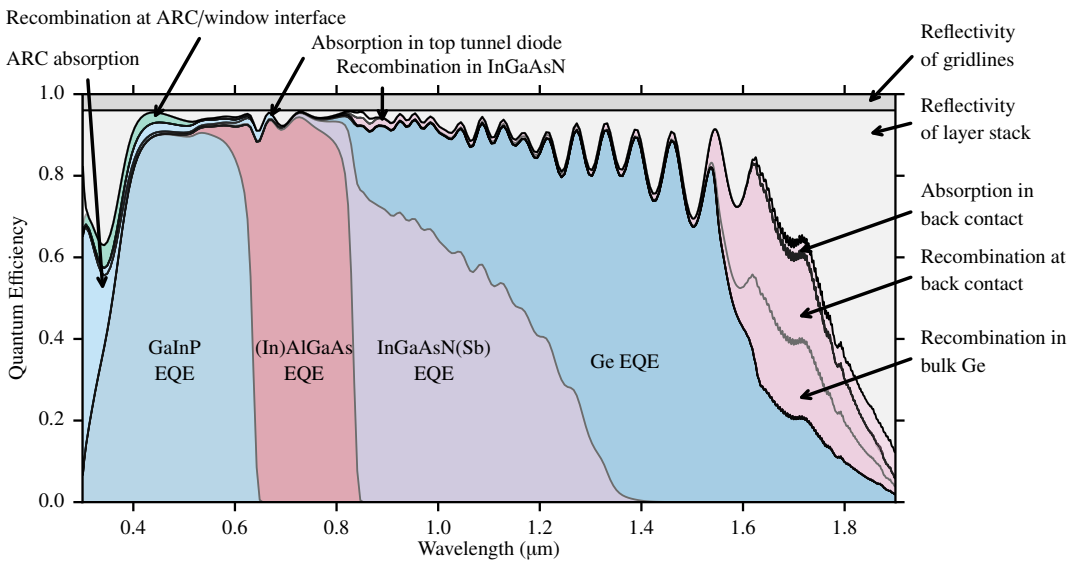

Figure 2.6: Quantum efficiency plot showing the breakdown of losses.

solar cells should be accompanied by calibration against as-grown material. This applies particularly to the complex refractive index of ARC layers, whose porosity tends to vary from lab to lab with significant effects on the optical properties, and to minority carrier lifetimes which can be dependent on material quality.

Ohmic losses in the top emitter and gridlines, and uneven bias across the surface of the cell significantly impact efficiency. These effects are driving a trend towards smaller cells in CPV applications, and cannot be studied using a standard diode model. In general, simulations based on the drift-diffusion have no presupposition of diode-like behaviour, and as such they are useful for exploring the performance of devices in extremes of operating conditions, or in device designs where closed-form diode models are not supported.

Table 2.4: Table of material parameters for the GaInP / (In)AlGaAs / InGaAsN(Sb) / Ge solar cell example. Paired values in parentheses are specified for electrons and for holes respectively.

	Symbol	**Units**	**$Ga_{0.49}In_{0.51}P$**	**$In_{0.01}Ga_{0.99}As$**	**Germanium**
	ϵ/ϵ_0		12.005	12.91	16.0
			ref. [55]	ref. [55]	ref. [54, 85]
	n, k		ref. [69]	ref. [91]	ref. [92]
Band gap	$E_{g,0}$	eV	1.88	1.40	0.744
	α	eV/K	1.82×10^{-4}	5.405×10^{-4}	4.77×10^{-4}
	β	K	81	204	235
	T_{ref}	K	300	300	0
	χ_0	eV	3.924	4.07	3.960
	ΔE_g	eV	ref. [55]	ref. [64]	ref. [55]
	$\Delta\chi/\Delta E_g$		0.5	0.5	0.5
			ref. [93]	ref. [76]	ref. [54]
Density of states	m_n/m_0		0.08515	0.06553	0.5438
	$N_{C,300}$	cm^{-3}	6.235×10^{17}	4.210×10^{17}	1.0063×10^{19}
	m_p/m_0		0.7125	0.5236	0.3406
	$N_{V,300}$	cm^{-3}	1.5093×10^{19}	9.509×10^{18}	4.9883×10^{18}
			ref. [55, 93]	ref. [76, 93]	ref. [55, 93]
Mobility (Masetti model)	μ_{max}	$cm^2/V.s$		(9400, 491.5)	
	ζ			(2.1, 2.2)	
	μ_{min1}	$cm^2/V.s$		(500.0, 20.0)	
	μ_{min2}	$cm^2/V.s$		(500.0, 20.0)	
	μ_1	$cm^2/V.s$		(0, 0)	
	P_c	cm^{-3}		(0, 0)	
	C_r	cm^{-3}		$(6 \times 10^{16}, 1.48 \times 10^{17})$	
	C_s	cm^{-3}		(0, 0)	
	α			(0.394, 0.38)	
	β			(0, 0)	
				ref. [94]	
Mobility (Arora model)	A_{min}	$cm^2/V.s$	(400.0, 15.0)		(850.0, 300.0)
	α_m		(0, 0)		(0, 0)
	A_d	$cm^2/V.s$	(3900, 135)		(2950, 1500)
	α_d		(0, 0)		(0, 0)
	A_N	cm^{-3}	$(2 \times 10^{16}, 1.5 \times 10^{17})$		$(2.6 \times 10^{17}, 1 \times 10^{17})$
	α_N		(1.955, 1.47)		(0, 0)
	A_a		(0.7, 0.8)		(0.56, 1.0)
	α_a		(0, 0)		(0, 0)
			ref. [94]		ref. [54]
Recombination	B_{rad}	cm^3/s	1×10^{-10}	2×10^{-10}	6.4×10^{-14}
	τ_{max}	s	$(2 \times 10^{-8}, 2 \times 10^{-8})$	$(1 \times 10^{-7}, 2 \times 10^{-8})$	(0.001, 0.001)
	τ_{min}	s	(0, 0)	(0, 0)	(0, 0)
	N_{ref}	cm^{-3}	$(1 \times 10^{19}, 1 \times 10^{19})$	$(1 \times 10^{16}, 2 \times 10^{18})$	$(1 \times 10^{16}, 1 \times 10^{16})$
	γ		(1.0, 1.0)	(1.0, 3.0)	(1.0, 1.0)
	T_α	K	(0, 0)	(0, 0)	(0, 0)
	T_{coeff}		(0, 0)	(0, 0)	(0, 0)
	C_n,C_p	cm^6s^{-1}	$(3 \times 10^{-30}, 3 \times 10^{-30})$	$(5 \times 10^{-30}, 5 \times 10^{-30})$	$(1 \times 10^{-30}, 1 \times 10^{-30})$
			ref. [93]	ref. [93]	ref. [93]
Nonlocal tunneling	g		(0.21, 0.4)	(0.21, 0.4)	
	m_t/m_0		(0.24, 0.48)	(0.085, 0.34)	
			ref. [87]	ref. [86]	

Table 2.5: Table of material parameters for the GaInP / (In)AlGaAs / InGaAsN(Sb) / Ge solar cell example. Paired values in parentheses are specified for electrons and for holes respectively.

	Symbol	Units	$Al_{0.5}In_{0.5}P$	$Al_{0.3}Ga_{0.7}As$	$Al_{0.2}Ga_{0.8}As$
	ϵ/ϵ_0		11.355	12.055	12.34
			ref. [55]	ref. [55]	ref. [55]
	n, k		ref. [69]	ref. [65]	ref. [65]
Band gap	$E_{g,0}$	eV	2.382	1.7976	1.6726
	α	eV/K	1.76×10^{-4}	4.98×10^{-4}	5.12×10^{-4}
	β	K	134.2	142.8	163.2
	T_{ref}	K	300	300	300
	χ_0	eV	3.75	3.756	3.877
	ΔE_g	eV	ref. [55]	ref. [64]	ref. [64]
	$\Delta\chi/\Delta E_g$		0.5	0.5	0.5
			ref. [76]	ref. [76, 93]	ref. [76, 93]
Density of states	m_n/m_0		0.23	0.0879	0.0796
	$N_{C,300}$	cm^{-3}	2.768×10^{18}	6.540×10^{17}	5.636×10^{17}
	m_p/m_0		0.36	0.5842	0.5593
	$N_{V,300}$	cm^{-3}	5.4203×10^{18}	1.1206×10^{19}	1.0496×10^{19}
			ref. [76]	ref. [76, 93]	ref. [76, 93]
Mobility (Masetti model)	μ_{max}	$cm^2/V.s$	(150.0, 180.0)	(3721.1, 240)	(5896.6, 308.21)
	ζ		(1.0, 1.0)	(1.74, 1.83)	(1.81, 1.9)
	μ_{min1}	$cm^2/V.s$	(0, 0)	(195.09, 5.0)	(313.6, 8.8571)
	μ_{min2}	$cm^2/V.s$	(0, 0)	(195.09, 5.0)	(313.6, 8.8571)
	μ_1	$cm^2/V.s$	(0, 0)	(0, 0)	(0, 0)
	P_c	cm^{-3}	(0, 0)	(0, 0)	(0, 0)
	C_r	cm^{-3}	$(5 \times 10^{17}, 2.75 \times 10^{17})$	$(1.16 \times 10^{17}, 1.00 \times 10^{17})$	$(9.33 \times 10^{16}, 1.07 \times 10^{17})$
	C_s	cm^{-3}	(0, 0)	(0, 0)	(0, 0)
	α		(0.436, 0.397)	(0.5758, 0.324)	(0.5152, 0.33425)
	β		(0, 0)	(0, 0)	(0, 0)
			ref. [94]	ref. [94]	ref. [94]
Mobility (Arora model)	A_{min}	$cm^2/V.s$			
	α_m				
	A_d	$cm^2/V.s$			
	α_d				
	A_N	cm^{-3}			
	α_N				
	A_a				
	α_a				
Recombination	B_{rad}	cm^3/s	1×10^{-10}	1×10^{-10}	1×10^{-10}
	τ_{max}	s	$(2.5 \times 10^{-8}, 2.5 \times 10^{-8})$	$(1 \times 10^{-6}, 1 \times 10^{-8})$	$(1 \times 10^{-6}, 1 \times 10^{-8})$
	τ_{min}	s	$(5 \times 10^{-10}, 5 \times 10^{-10})$	(0, 0)	(0, 0)
	N_{ref}	cm^{-3}	$(1 \times 10^{16}, 1 \times 10^{16})$	$(1 \times 10^{16}, 2 \times 10^{18})$	$(1 \times 10^{16}, 2 \times 10^{18})$
	γ		(1.0, 1.0)	(1.0, 3.0)	(1.0, 3.0)
	T_α	K	(0, 0)	(0, 0)	(0, 0)
	T_{coeff}		(0, 0)	(0, 0)	(0, 0)
	C_n,C_p	cm^6s^{-1}	$(3 \times 10^{-30}, 3 \times 10^{-30})$	$(1 \times 10^{-30}, 1 \times 10^{-30})$	$(1 \times 10^{-30}, 1 \times 10^{-30})$
			ref. [93]	ref. [93]	ref. [93]
Nonlocal tunneling	g			(0.21, 0.4)	
	m_t/m_0			(0.09, 0.37)	
				ref. [86]	

Table 2.6: Table of material parameters for the GaInP / (In)AlGaAs / InGaAsN(Sb) / Ge solar cell example. InGaAsN(Sb) parameters are specific to the alloy composition of 11% In, 3.6% N. Some parameters are estimated from an InGaAs alloy with equal In composition. Paired values in parentheses are specified for electrons and for holes respectively.

	Symbol	**Units**	**$Al_{0.25}Ga_{0.25}In_{0.5}P$**	**InGaAsN(Sb)**	**MgF**	**TiOx**
	ϵ/ϵ_0		11.84	13.4	5.3	6
			ref. [55]	ref. [55]	ref. [95]	ref. [96]
	n, k		ref. [69]	[11,55]	ref. [97]	ref. [98,99]
Band gap	$E_{g,0}$	eV	1.984	0.9617		
	α	eV/K	1.76×10^{-4}	5.05×10^{-4}		
	β	K	134.2	189		
	T_{ref}	K	300	0		
	χ_0	eV	3.997	4.32		
	ΔE_g	eV	ref. [55]	0		
	$\Delta\chi/\Delta E_g$		0.5	0.5		
			ref. [76]	ref. [79]		
Density of states	m_n/m_0		0.1214	0.0391		
	$N_{C,300}$	cm^{-3}	1.061×10^{18}	1.968×10^{17}		
	m_p/m_0		0.6244	0.471		
	$N_{V,300}$	cm^{-3}	1.24×10^{19}	8.23×10^{18}		
			ref. [55, 93]	[79]		
Mobility (Masetti model)	μ_{max}	$cm^2/V.s$				
	ζ					
	μ_{min1}	$cm^2/V.s$				
	μ_{min2}	$cm^2/V.s$				
	μ_1	$cm^2/V.s$				
	P_c	cm^{-3}				
	C_r	cm^{-3}				
	C_s	cm^{-3}				
	α					
	β					
Mobility (Arora model)	A_{min}	$cm^2/V.s$	(400.0, 15.0)	(220,220)		
	α_m		(0, 0)	(1,1)		
	A_d	$cm^2/V.s$	(3900, 135)	(0,0)		
	α_d		(0, 0)	(0,0)		
	A_N	cm^{-3}	$(2 \times 10^{16}, 1.5 \times 10^{17})$	$(1 \times 10^{18}, 1 \times 10^{18})$		
	α_N		(1.955, 1.47)	(0,0)		
	A_a		(0.7, 0.8)	(0,0)		
	α_a		(0, 0)	(0,0)		
			ref. [94]	ref. [100]		
Recombination	B_{rad}	cm^3/s	1×10^{-10}	1×10^{-8}		
	τ_{max}	s	$(1 \times 10^{-9}, 1 \times 10^{-9})$	$(0.5 \times 10^{-9}, 0.5 \times 10^{-9})$		
	τ_{min}	s	(0, 0)	(0, 0)		
	N_{ref}	cm^{-3}	$(1 \times 10^{19}, 1 \times 10^{19})$	$(1 \times 10^{16}, 1 \times 10^{16})$		
	γ		(1.0, 1.0)	(1.0, 1.0)		
	T_α	K	(0, 0)	(0, 0)		
	T_{coeff}		(0, 0)	(0, 0)		
	C_n,C_p	cm^6s^{-1}	$(3 \times 10^{-30}, 3 \times 10^{-30})$	$(3 \times 10^{-30}, 3 \times 10^{-30})$		
			ref. [93]	[12,93]		
Nonlocal tunneling	g					
	m_t/m_0					

Table 2.7: Table of interface parameters for the GaInP / (In)AlGaAs / InGaAsN(Sb) / Ge solar cell example. Paired values in parentheses are specified for electrons and for holes respectively.

	Symbol	**Units**	**TiOx/AlInP**	**AlInP/GaInP**	**GaAs/AlGaAs**	**GaInP/Ge**
Interface recombination	S_0	cm/s	0 fitted	$(2\times10^5, 2\times10^5)$ ref. [83]/fit to data	(200, 200) ref. [83]	$(1\times10^5, 1\times10^5)$ ref. [47]/fit to data

Chapter 3

Dilute nitride single junctions

Matthew Wilkins, James Gupta, Simon Fafard, Abdelatif Jaouad, Boussairi Bouzazi, Abderraouf Boucherif, Christopher E. Valdivia, Richard Arès, Vincent Aimez, Henry P. Schriemer and Karin Hinzer

This is a reproduction of an article published in SPIE Journal of Photonics for Energy *in a special section on tandem solar cells. It describes experiments with design, growth and characterization of dilute nitride solar p-n junctions for use in multi-junction solar cells.*

3.1 Introduction

Multi-junction solar cells achieve the highest power conversion efficiency of any solar power technology as a result of their improved harvesting of the solar spectrum by absorbing different wavelengths in different *p-n* junctions, called subcells. Three-junction lattice matched solar cells grown by molecular beam epitaxy (MBE) and incorporating a ~1 eV

dilute nitride subcell have shown excellent power conversion efficiency, including a result of 44.0% under 942 suns concentration [13, 44] and 29% at 1 sun [101]. *Non-lattice matched* approaches using wafer bonding, metamorphic composition-graded buffers and/or epitaxial liftoff have shown the greatest efficiency overall with successful four-junction devices reaching up to 46.0% under concentration using a wafer bonded architecture [1, 5], and 45.7% using an inverted metamorphic architecture [30]. In contrast, a *lattice matched* four-junction cell could yield near-record efficiency while avoiding the added costs associated with those techniques.

Previous numerical modeling studies on lattice-matched four-junction $Ga_{0.5}In_{0.5}P$/ $Al_{0.05}GaAs$/InGaAsN(Sb)/Ge cells incorporating dilute nitrides highlighted the importance of using photons efficiently, absorbing only those photons that have a high probability of being collected [102]. Hence, photons at wavelengths that cannot be collected efficiently are best used by transmitting through to the bottom germanium junction. In general, the lower junctions should have a slightly higher J_{SC} than the upper junctions in order to preserve the fill factor and efficiency of the multi-junction device [103]. Due to the short diffusion length in InGaAsN(Sb), an *n*-*i*-*p* structure is commonly used to enhance carrier collection and provide an effective 'collection length' which is longer than the diffusion length; furthermore, thick *n*-*i*-*p* InGaAsN(Sb) and InGaAsN(Bi) junctions are highly sensitive to background doping levels, and those doping levels are strongly dependent on annealing conditions [104, 105]. In some cases annealing can convert the background doping from *p*-type to *n*-type, causing the *p*-n junction to be located at the back of the absorber and reducing the quantum efficiency [104]. Consequently, these subcells with materials having lower mobilities must be carefully considered within the context of operating characteristics of the complete device.

In this article, we present an experimental study of dilute nitride InGaAsN(Sb) junction designs to be incorporated in four-junction solar cells. To that end, the design of the

Table 3.1: Layer structures of the three designs. Differences are in bold face.

		D1		D2		D3	
Layer	material	doping (cm^{-3})	thick. (μm)	doping (cm^{-3})	thick. (μm)	doping (cm^{-3})	thick. (μm)
Cap	GaAs			n 5×10^{18}	0.05		
Filter	$Al_{0.05}Ga_{0.95}As$			n 1×10^{18}	2.00		
Window	$Al_{0.5}Ga_{0.5}As$			n 5×10^{18}	0.05		
n-Emitter	GaAs			n 5×10^{18}	0.05		
Absorber	InGaAsN(Sb)	***i***	**1.00**	***i***	**0.65**	***p*** 1×10^{16}	**0.65**
p-Base	GaAs			p 1×10^{19}	0.05		
Sacrif.	InGaAsN(Sb)	***p*** 1×10^{17}	**0.20**	***p*** 1×10^{17}	**0.20**	**layer omitted**	
Buffer	GaAs			p 1×10^{18}	0.20		
Substr.	GaAs			p	650		

InGaAsN(Sb) subcell is optimized for concentrating photovoltaic applications, and the surrounding layers are designed to replicate the optical environment of a $Ga_{0.5}In_{0.5}P$/ $Al_{0.05}GaAs$/InGaAsN(Sb)/Ge device. A filter layer is included to block light that would be absorbed in the top two junctions, with its material and thickness chosen to match that of the second junction of our hypothetical four-junction structure. We use a relatively thin InGaAsN(Sb) junction to make it more robust with respect to varying material quality. This thin junction avoids negatively impacting the performance of other junctions, is current-matched to a fully lattice matched four-junction cell, and could be easily adapted for devices of five junctions or more.

3.2 Method

Following the design study that was conducted in simulation [45, 46], a nominal design (D1) and two variants (D2 and D3) were prepared to cover the design space that would provide adequate short-circuit current density with minimal collection losses. In the D1 design, a nominally intrinsic InGaAsN(Sb) absorber layer of 1.0 μm thickness was used, similar to many previous works on InGaAsN(Sb) cells [12, 104]. D2 is identical except for the use of a thinner absorber of 0.65 μm thickness, as listed in Table 3.1. Both D1 and

D2 include a 0.2 μm sacrificial dilute nitride layer to incorporate any pre-existing surface impurities, as suggested by Ptak [106]. As an added benefit, this layer helps to replicate operating conditions in the middle of a 4-junction device with a germanium bottom junction by absorbing some of the light which might otherwise be reflected from the back surface of the wafer and be absorbed on a second pass through the InGaAsN(Sb) junction.

The D3 design also included a thin 0.65 μm absorber, which was intentionally *p*-doped to 1×10^{16} cm^{-3}, but the sacrificial layer was omitted. Given that InGaAsN(Sb) material can often have n-type background doping, this ensures that we have a p-type cell, with the junction near the front, to compare against. For each design, a simulated cross-sectional band diagram is shown in Fig. 3.1. These are calculated using drift-diffusion based simulations which have been described in references [45, 46].

Three wafers (one wafer of each design) were grown by molecular beam epitaxy (MBE) in a custom V90 system containing valved cracker sources for As_2 and Sb_2 and conventional effusion cells for the group-III elements and dopants. Active nitrogen was provided by a radio frequency plasma source using N_2/Ar dynamic gas switching. Details of the growth method can be found in references [17, 18]. Biased deflector plates such as those used in reference [12] were not employed here. The growths were performed on 76 mm diameter, single-side polished Zn-doped GaAs substrates with (100)±0.1° orientation.

We prepared samples of each design, using a complete fabrication process*, including grid deposition and rapid thermal anneal. The GaAs cap layer was removed by etching, but no anti-reflective coating was applied.

*Photolithography was used to define the contact patterns with a positive resist. The grid lines and busbar regions were protected by the photoresist and the GaAs cap layer was etched selectively relative to the window layer in a NH_4OH:H_2O_2:H_2O solution. The photoresist was stripped and the sample was cleaned. The surface was deoxidized using a BHF solution and the samples were immediately introduced into a PECVD reactor. A second photolithography process using double resist layers was performed, followed by a standard deposition/lift-off process to define the ohmic contact (a Ni/Ge/Au/Ni metal structure prepared by e-beam evaporation). The backside contact was obtained by e-beam evaporation of Ti/Pt/Au. The contacts were annealed for one minute at 430 °C in a forming gas atmosphere. A thick contact layer of Ti/Au (20 nm/4000 nm) was evaporated on the back side.

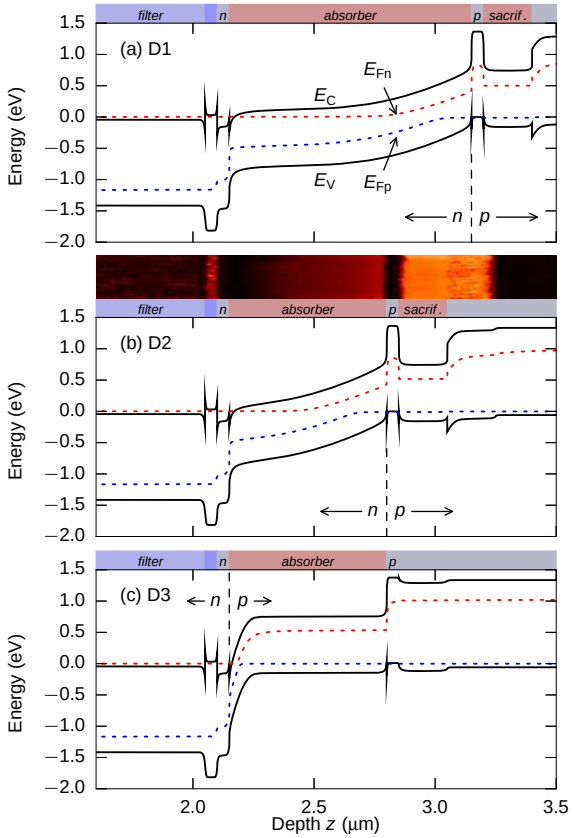

Figure 3.1: Simulated energy band diagrams of (a) D1, (b) D2, and (c) D3 at short circuit with 1000 suns illumination, AM1.5D spectrum. In (b), the scanning probe microscope tip-sample resistance, as measured with scanning spreading resistance microscopy (SSRM), is also shown as a function of position; brighter color indicates higher resistance. Scanning probe measurements were done with all device layers grounded via a layer of indium solder applied to the edge of the device.

3.3 Results

Carrier collection

A study of an un-annealed D2 wafer sample using cross-sectional scanning capacitance microscopy (SCM) indicated that the undoped material in these devices is *n*-type. This was confirmed by scanning spreading resistance microscopy (SSRM). SSRM results are incorporated in Fig. 3.1 (b), with brighter colors indicating higher resistance, and show

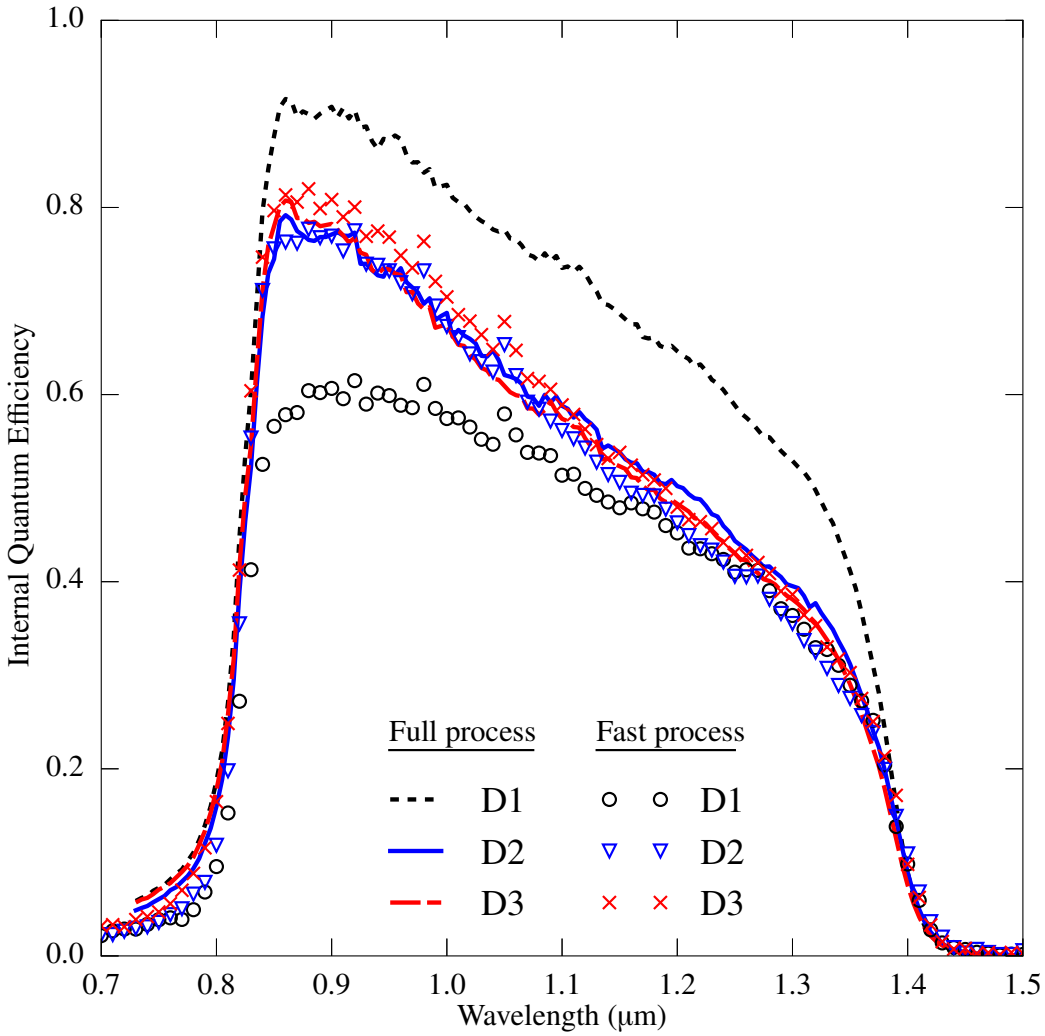

Figure 3.2: IQE of the full-process and fast-process samples.

that the material resistivity increases toward the back side of the InGaAsN(Sb) layer, hence the material is most depleted of carriers near that interface. The presence of a gradient in resistivity throughout the width of the InGaAsN(Sb) absorber indicates that there is significant depletion resulting from a strong built-in electric field over the full thickness of the absorber. Our device simulations show a similar gradient in resistivity when an *n*-type background doping of 2×10^{15} cm^{-3} is used.

External quantum efficiency (EQE) of the devices were measured with a Newport IQE-200 system. Specular and diffuse reflectivity, R_s and R_d, were also measured and used to calculate internal quantum efficiency (IQE) according to $IQE = EQE/(1 - R_s - R_d)$.

In Fig. 3.2, all samples show a steady reduction in IQE for longer wavelengths, which is expected due to the optically thin absorber. The samples show an absorption edge at 1400 nm, consistent with an effective InGaAsN(Sb) band gap of 0.90 eV. Although the AM1.5D solar spectrum provides little photon flux in the 1300 to 1400 nm range due to a water absorption line, there is still an advantage to this low band gap material in that its absorption coefficient at the relevant wavelengths of 830 - 1300 nm is increased as compared to a 1.0 eV design, for example. Data on the near-bandgap absorption coefficient of dilute nitride materials was reported by Kurtz *et al.* [107]

All of the IQE measurements show a small tail extending to photon energies well above the $Al_{0.05}Ga_{0.95}As$ band gap at 830 nm. This could be a result of luminescent coupling from the AlGaAs filter into the InGaAsN(Sb) absorber [45], and will not necessarily contribute photocurrent in an operating 4-junction device, unless the junctions with larger band gap are producing an excess of photocurrent [108].

To characterize the InGaAsN(Sb) junctions in a nearly as-grown condition with minimal annealing, a set of 'fast-process' samples were prepared from 5 mm × 5 mm dies cleaved from the as-grown wafer. These samples were prepared with ohmic indium contacts to the top and bottom faces and are sufficient for quantum efficiency measurements, but the contacts are not adequate for operation at high currents. The advantage of this process is that the contacts are formed with only a 30 s anneal at 200 °C, which we consider to be negligible in terms of its effect on the dilute nitride material.

The cap layer was not etched away for these experiments; we estimate that the cap parasitically absorbs 0.14 mA/cm^2 of the available 1-sun photocurrent, based on simulated IQE with and without the cap layer.

EQE and IQE of these samples was measured using a 4-wire connection to the device under test. The illuminating 2 mm×0.5 mm beam was positioned such that it was not incident on the top contacts. The 'fast-process' D1 samples with the 1.0 μm absorber have the lowest peak IQE, at 60%, and short-circuit current density, J_{SC} of 13.4 mA/cm^2, calculated using the IQE with reference to the AM1.5D spectrum at 100 mW/cm^2 (1 sun). These are the only samples which show significant improvement under reverse bias, where the peak IQE increases by 17% absolute at -1 V; minimal further improvement was found for larger bias. The D2 and D3 samples with the 0.65 μm thick absorber reach a peak IQE of 75% and 81%, respectively, with J_{SC} of 15.0 mA/cm^2 and 16.6 mA/cm^2 respectively. Despite the thinner absorber, these samples show higher IQE overall, and the absence of any un-collected absorption is a benefit for integration in a multi-junction device where any transmitted light may be absorbed in the next junction. The difference between the 0.65 μm and 1.0 μm absorbers is most pronounced at short wavelengths which are absorbed toward the top of the junction. Given that the absorber is most heavily depleted toward the bottom of the layer due to *n*-type background doping, it is likely that the built-in electric field is insufficient to collect carriers from the front of the thick 1.0 μm, fast-process absorber (Figure 3.1 a).

The InGaAsN(Sb) subcell was designed based on the results of simulations of complete 4-junction structures, with the intention of having an overall J_{SC} of 12.5 mA/cm^2 for the 4-junction device. Both the InGaAsN(Sb) junction and the Ge junction are intended to have J_{SC} exceeding 12.5 mA/cm^2 in order to maintain a high fill factor [103]. We have achieved this in the InGaAsN(Sb) junction, and the measured QE is consistent with our simulations which indicate ~ 13 mA/cm^2 in the Ge subcell when the 0.65 μm absorber is used. The 1 μm absorber would absorb too much and so in that case the 4J device would be limited by the bottom germanium subcell with a J_{SC} of ~ 8.3 mA/cm^2.

Comparing the 'fast process' and fully fabricated D1 samples, we observed a change in

Table 3.2: Measured parameters of the fully fabricated devices. J_{SC} is calculated by integrating the measured IQE with the AM1.5D spectrum scaled to 100 mW/cm^2.

Device	J_{SC} (mA/cm^2)	1-sun V_{OC} (V)	1000-sun V_{OC} (V)
D1	18.5	0.166	0.428
D2	15.1	0.164	0.422
D3	14.4	0.186	0.436

peak IQE from 60% to 90%, yielding a 35% improvement in J_{SC}. The thinner D2 and D3 samples showed no change with processing, and IQE is consistent with full collection of generated carriers. These observations are consistent with a *collection* length (combining the effects of drift and diffusion) of at least 0.65 μm in all of the fast-processed samples, which improved to >1 μm in the fully fabricated samples. The increased collection length could be caused by either an improved diffusion length, a change in background doping type, or a wider depletion region within the dilute nitride absorber. SSRM measurements of the full-process D1 sample show no significant changes in the resistivity profile through the sample as would be expected for the latter two possibilities, and so a change in diffusion length is indicated. We find good agreement between simulations and measurement with a *diffusion* length of 0.3 μm before annealing and >1.0 μm after annealing.

Current-voltage characterization

When integrated in a four-junction solar cell, we estimate that the complete cell would operate with $J_{SC} \sim 12.5$ mA/cm^2 and maximum-power current density $J_{MP} \sim 11.5$ mA/cm^2 under 1-sun, AM1.5D conditions, based on our previous study of photocurrent sharing between the four junctions [46]. Therefore it is important that similar current density is available from the InGaAsN(Sb) subcell; in fact it is advantageous for the InGaAsN(Sb) cell to over-produce somewhat relative to the higher junctions so that it will not have a negative impact on fill factor of the multi-junction device [46, 103]. Current densities (J) were

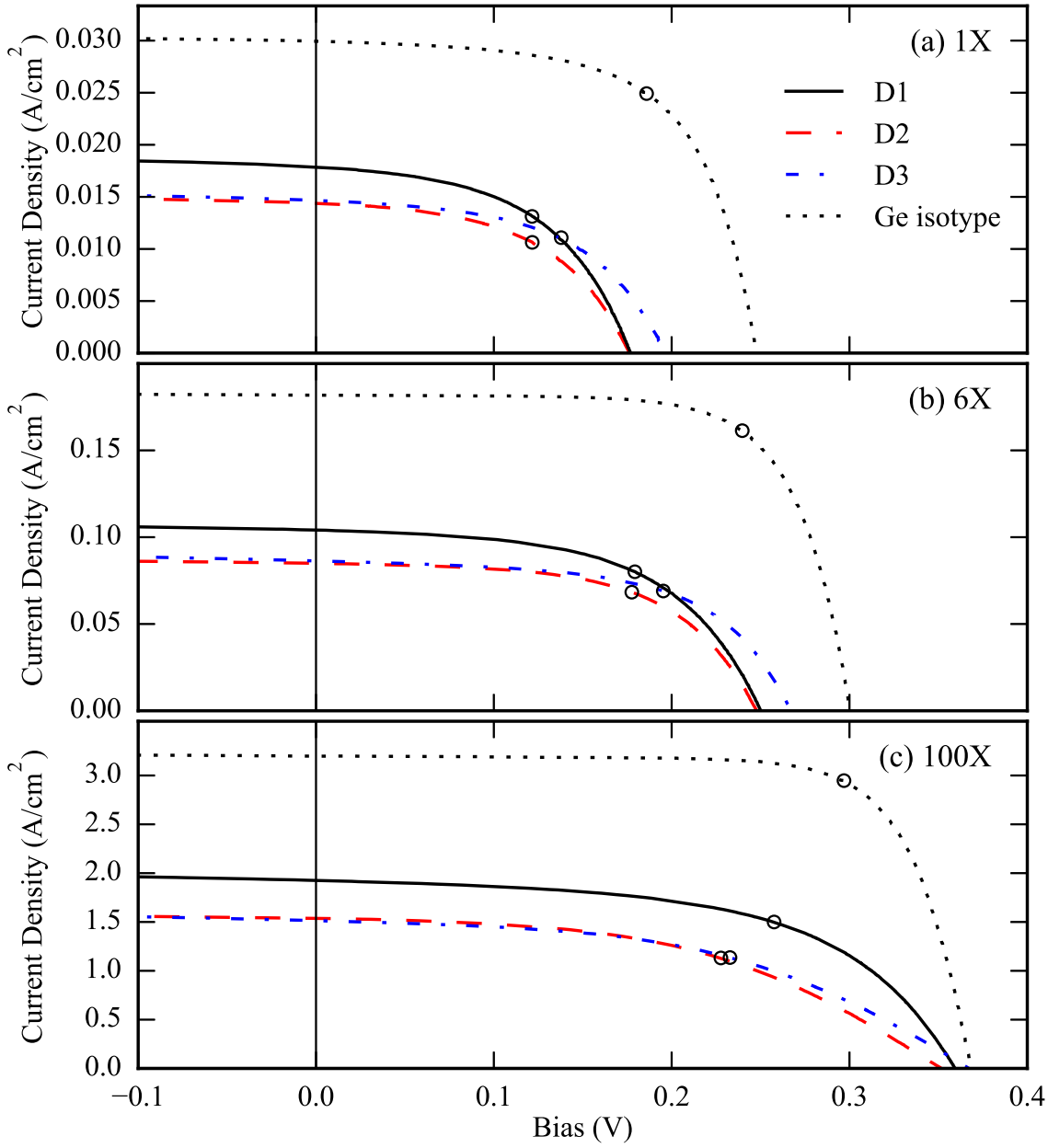

Figure 3.3: *J-V* curves of the fabricated devices at concentrations of (a) 1, (b) 6, and (c) 100 suns. The concentration is as indicated by a GaInP/GaAs/Ge reference cell; no mismatch correction has been applied. Maximum power points are indicated with black circles.

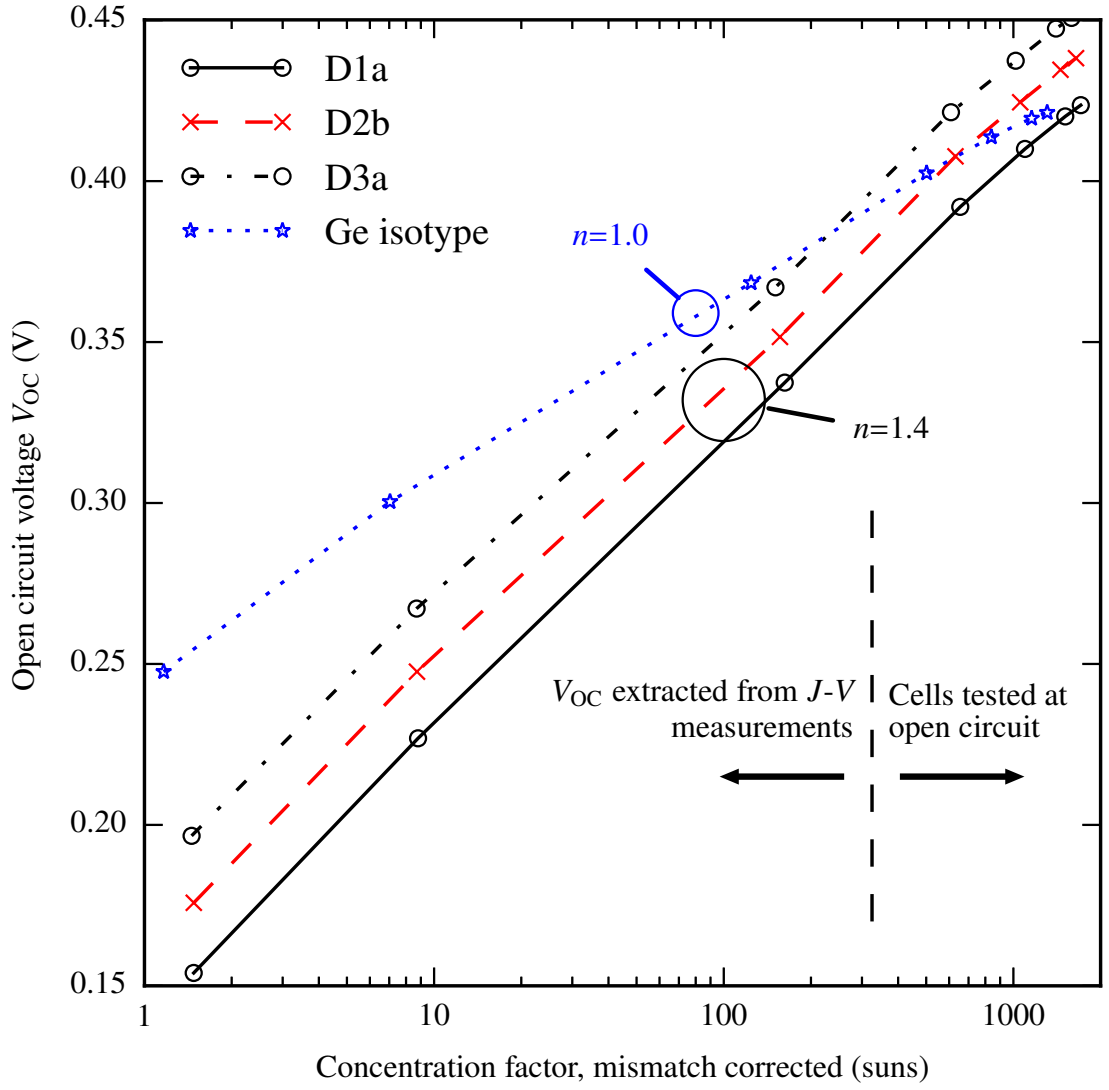

Figure 3.4: Open-circuit voltage as a function of concentration for the three designs under a xenon flash solar simulator, where 1 sun = 100 mW/cm^2.

measured across a range of bias voltages (V) at concentrations of 1, 6 and 100 suns using an Alpha-Omega Power Technologies xenon flash solar simulator. This solar simulator uses a xenon arc flash lamp to illuminate devices under test with a peak intensity which is variable between 0.5 and 4000 suns. Intensity is varied by changing the focusing optics and/or adjusting the voltage applied to the arc lamp. Optical filters provide control over the

spectrum. Flash pulses have a duration of approximately 10 µs, with a complete *J-V* curve being measured over a 0.5 µs window as the flash is at its peak. During each flash, both the device under test and a calibrated reference solar cell are illuminated and monitored. This enables corrections for variations in pulse intensity from flash to flash and also variations in intensity during the 0.5 µs measurement window.

The results are shown in Fig. 3.3. For the 0.65 µm designs D2 and D3, we find little difference in performance despite D3 being intentionally doped and having minimal electric field in the absorber (see Fig. 3.1 c), indicating that the drift-aided collection may not be important at this absorber thickness. All three designs show a significant reduction in the slope near V_{OC} which we consider to be a parasitic resistance.

We next consider the performance of the cells under high concentration. *n-i-p* junctions rely on the built-in electric field to drive carriers across the junction, but this field is reduced when the cell is operating under voltage bias. Therefore many *n-i-p* structures show a reduction in collected photocurrent as bias increases [4, 11, 109], and hence a reduction in fill factor and V_{OC}. This is evident as a small slope in the *J-V* curves near J_{SC} which is present at all concentrations. In contrast, a shunt conductance would lead to a similar slope but would have reduced impact as concentration increases.

We also see significant effects due to series resistance which reduce fill factor and efficiency at 100 suns, Fig. 3.3 (c). Consequently we find that 6X is the maximum practical concentration for these samples. We expect that the impact of series resistance, and to a lesser extent the bias-dependent carrier collection, can be reduced in an optimized device as has been demonstrated in the literature [44].

For the lower concentration measurements described above, V_{OC} values were extracted from the individual *J-V* curves. The top contacts were not optimized for large currents and so for the higher concentrations, on the order of 1000 suns, V_{OC} values were determined explicitly by testing at open circuit. All of the measured V_{OC} values are plotted in Fig. 3.4

against concentration, which has been corrected for spectral mismatch to AM1.5D [90], in order to extract the diode ideality factors n for the various designs. The Ge isotype demonstrates $n = 1$ behavior, but the three *n-i-p* designs show $n = 1.4$ behavior up to the maximum measured intensity of 1500 suns, indicating that V_{OC} is significantly influenced by recombination in the wide space charge region, at least up to the maximum measured bias of 0.45 V.

Table 3.2 summarizes J_{SC} and V_{OC} of the fully fabricated devices for reference. To illustrate what may be achieved with finished devices, which would have appropriate anti-reflection coatings, J_{SC} values are reported as the integral of device IQE with the reference spectrum, rather than extracted from the *J-V* curves. All of the J_{SC} values are adequate to exceed the expected 4-junction J_{SC} of 12.5 mA/cm^2. Simulations show that these results are consistent with $\sim$ 100% collection of carriers that are generated in the InGaAsN(Sb) absorber. D1 somewhat exceeds the needed current density and if this material quality can be achieved consistently the design could be adapted to use a larger band gap of 0.95 eV. At this point though, we do not have consistent results from sample to sample with the D1 design whereas D2 and D3 are more robust to changes in processing.

Using the 1-sun V_{OC}, the band gap-voltage offsets $W_{OC} = qE_g - V_{OC,1-sun}$ are 0.76, 0.74 and 0.71 V for the D1, D2 and D3 designs, respectively. For reference, an offset of 0.4 V is usually considered to be an indication of 'good quality' material. These values are, however, in line with some other reported InGaAsN(Sb) devices [110] and InGaAsN(Bi) devices [105]. More recently, Miyashita *et al.* have shown InGaAsN(Sb) solar cells with W_{OC} as low as 0.58 V [16]. As concentration increases, V_{OC} of the InGaAsN(Sb) devices surpasses that of our 0.67 eV Ge isotype at ~300 - 1000 suns. The D3 sample which had the lowest J_{SC} has the greatest V_{OC}. V_{OC} and fill factor will need to be improved further in order for a 4-junction device to reach a competitive level of efficiency. In particular, the apparent series resistance of these samples prevents them from being used at high concentration.

If we take our previous simulations of 4-junction cells and substitute in InGaAsN(Sb) junctions with the measured J_{SC}, V_{OC} and ideality factor as listed in 3.2 (but with no series resistance), we find efficiencies of 29.7%, 42.9% and 43.1% for D1, D2 and D3 respectively. The D1 efficiency is low, as expected, due to its optically thick absorber layer which passes insufficient light through to the bottom junction.

3.4 Conclusion

In summary, we have presented results of InGaAsN(Sb) cells which exceed the 12.5 mA/cm^2 at 1-sun needed for current matching in a four-junction, GaInP/(Al)GaAs/InGaAsN(Sb)/Ge solar cell. The cells have minimal collection losses; photons that are not collected as carriers will be transmitted through to the next lower subcell rather than being lost. The 0.65 μm design is robust against changes in background doping and annealing condition which is promising for integration into a full multijunction device. A similar design approach may be applicable to other devices such as lattice matched, InGaAsN(Sb)-based multi-band photodetectors.

Chapter 4

Luminescent Coupling

Matthew Wilkins, Christopher E. Valdivia, Ahmed M. Gabr, Denis P. Masson, Simon Fafard and Karin Hinzer

This is a reproduction of an article published in Journal of Applied Physics *in 2015 [111]. It extends the simulation method described in Chapter 2 to include effects of luminescent coupling. The computational algorithm is described in detail and the results are compared with experimental measurements of 5-junction PPCs.*

In recent years as the quality of III-V photovoltaic materials such as GaAs and $Ga_{0.5}In_{0.5}P$ have improved, the effects of photon recycling and luminescent coupling have become increasingly significant in the design of very-high efficiency photovoltaic devices. *Photon recycling* refers to emission and re-absorption, typically within a single material layer or junction, and can yield an increase in open-circuit voltage of single- and multi-junction devices [112]. *Luminescent coupling* refers to emissions of photons from one location in a

device which are re-absorbed, possibly in a different device region, and has been shown to reduce spectral sensitivity of multi-junction solar cells [29].

Techniques have been developed to quantify the degree of coupling between junctions in a multi-junction solar cell [113], and to model the effects using lumped- or distributed-parameter models [34]. Létay *et al.* have also modelled photon recycling effects in single junctions within a drift-diffusion simulator, using an iterative approach which involves running the simulator repeatedly with successive approximations of the coupled photocurrent [32, 33, 114, 115]. Luminescent coupling has also been incorporated into simulations of light-emitting diodes [116].

In this work, we present a device with five monolithically integrated GaAs junctions displaying strong effects attributed to luminescent coupling. In typical multi-junction solar cells, each junction has a different band gap, and therefore coupling proceeds in only one direction (from high to low band gap materials). However, in this device, coupling must be considered over all junction permutations. We analyze the device using a newly developed, two-step technique which incorporates the modeling of luminescent coupling [45, 46] into drift-diffusion based simulations [55, 117] in a more direct way than that used by previous methods. The details of the modeling theory are outlined in the appendix.

The device studied here is a phototransducer designed and manufactured by Azastra Opto Inc. for use as a receiver in a power-over-fiber application. These devices have a structure similar to multi-junction solar cells, but all junctions are composed of GaAs of varying thicknesses (Fig. 4.1 a). They are intended to be coupled with a laser of up to 5 W at a single wavelength, 835 nm. To date, we have measured a power conversion efficiency of $61.6 \pm 3\%$ and open-circuit voltage of 5.92 V under $\sim$ 1.3 W single-wavelength illumination [118]. In the absence of luminescent coupling the overall device current is limited by the lowest photocurrent in any of the five junctions, and so the device is sensitive to the incident wavelength and to any variations in layer thicknesses. At shorter-than-

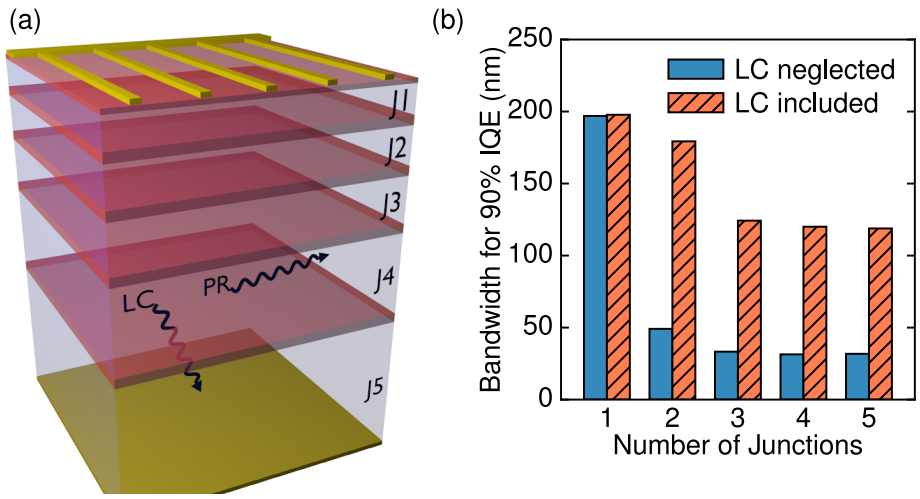

Figure 4.1: (a) General structure of the 5-junction phototransducer device. Photons are shown being emitted from junction 4 and propagating into junction 5 (luminescent coupling, LC) and being emitted from junction 4 and re-absorbed in the same junction (photon recycling, PR). (b) Simulated internal quantum efficiency bandwidth (at 90% of peak) for 1- to 5- junction phototransducer devices. Solid blue bars have luminescent coupling neglected, while hatched orange bars have luminescent coupling included in the model.

nominal wavelengths, light is absorbed strongly in the upper junctions (due to the higher absorptivity) and the lower junctions become limiting, while at longer wavelengths the upper junctions are limiting the overall device current.

In junctions able to produce higher photocurrent than the limiting one, excess photogenerated carriers will recombine either through a non-radiative or a radiative mechanism. The radiated photons may thereafter be re-absorbed within the same junction (photon recycling), a different junction (luminescent coupling), or exit the device (photoluminescence). For good-quality materials with sufficiently high internal radiative efficiency (fraction of radiative to total recombination), photon recycling leads to an accumulation of carriers and an increase in photovoltage, while luminescent coupling can help to redistribute photocurrent between the junctions more optimally, reducing the wavelength sensitivity.

The multi-junction photovoltaic device discussed here provides an excellent demonstration of photon recycling and luminescent coupling due to its limited set of relatively

well-known and characterized GaAs-based materials (enabling accurate models), and its five optically inter-coupled junctions exhibiting high internal radiative efficiency. For example, if we consider simulations of a series of devices with one to five junctions, we find that the devices become increasingly sensitive to the illuminating wavelength (Fig. 4.1 b). However, the inclusion of luminescent coupling significantly impacts the computed performance, greatly extending the range of usable wavelengths, and demonstrating the importance of including it in the numerical model.

4.1 Materials and Methods

The devices discussed here were grown by metal-organic chemical vapour deposition (MOCVD) in an Aixtron 2600 reactor, on 150 mm (100) oriented p-type GaAs substrates. The devices are 2.4 mm × 2.4 mm and have a circular aperture of 2.1 mm diameter (Fig. 4.2 a). They were fabricated with a pattern of 5 μm wide silver gridlines forming the top contact, and a two-layer anti-reflective coating optimized for transmission at 835 nm.

Efficiency of the fabricated devices was determined from current-voltage (*I*-*V*) curves measured while the device was illuminated by a fiber-coupled JDSU L4-2486 laser temperature-tuned to operate at 835 nm, using a Keithley 2420 source-measure unit, Fig. 4.2 (b). The fiber was multimode, with a 62.5 μm core diameter. Measurements were made under steady-state conditions. Device temperature was regulated at 25° C and power output from the laser was calibrated using a Thorlabs S121C silicon photodiode power sensor. Uncertainty in the measured efficiency was estimated at ±5% (relative) and was primarily limited by modal instability of the illuminating laser.

Internal quantum efficiency of the samples was measured using a Newport IQE-200 system including a chopper with digital lock-in amplifier at 87 Hz and independent measurement of specular and diffuse reflectivity. The system is calibrated using NIST traceable

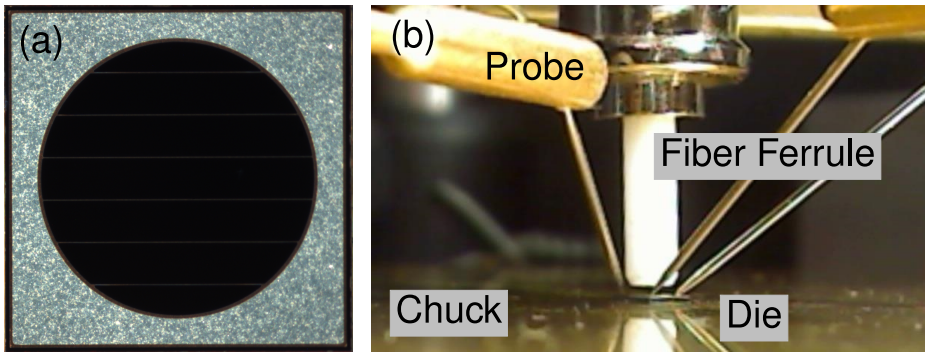

Figure 4.2: (a) Top view of a phototransducer die, including the circular aperture with 5 µm wide gridlines. (b) Four-wire *I-V* measurements were completed by contacting the top of the device by two current probes and one voltage-sense probe. The bottom of the device was contacted by the temperature-controlled, gold-plated stage. Illumination is provided by a multimode fiber-coupled laser held at a controlled height above the device.

calibration standards.

The phototransducer devices were simulated using a 2D finite-volume model in the drift-diffusion based device simulator Synopsys Sentaurus using published material parameters, and including realistic parameters for doping-dependent SRH (Shockley-Read-Hall) recombination, Auger recombination and surface recombination. Radiative recombination parameters are selected with care, as lifetimes derived from typical double heterostructure measurements may be artifically enhanced by photon recycling. Maximum SRH lifetime in GaAs was set at $\tau_{max} = 10^{-4}$ s except where otherwise noted, with the lifetime in all layers being reduced as a function of doping according to the Scharfetter relation [119]. A small interface recombination velocity of 100 cm/s was also included at all interfaces between GaAs and the adjacent layers.

The effects of photon recycling and luminescent coupling are modeled using a two-stage process. Prior to running the device simulator, coupling coefficients are calculated relating the radiative recombination rate at each mesh vertex with generation rates at all other vertices. This calculation is discussed in detail in the appendix. Then, the coupled

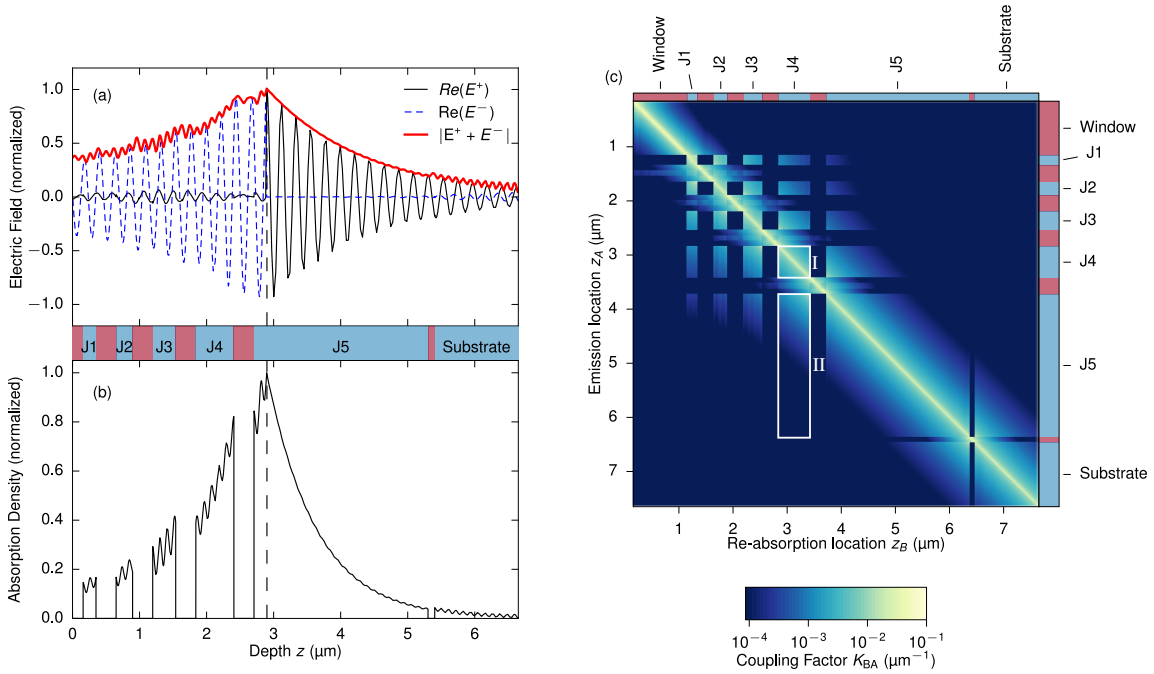

Figure 4.3: (a) Example of a TMM calculation for emission at a selected position internal to the structure (indicated by the vertical dashed line) for a single wavelength, angle of propagation, and polarization. The real parts of the forward and backward propagating field components, E^+ and E^- are shown, along with the magnitude of the total field $|E^+ + E^-|$. GaAs material layers are indicated with blue shading. The remaining layers, which have a larger band gap, are shaded in red. (b) Re-absorbed energy density as a function of position within the device for the same conditions. (c) Map of the optical coupling matrix, K for a 5-junction phototransducer device. Boxes along the diagonal indicate the strength of photon recycling, as in region I. Off-diagonal boxes indicate the strength of luminescent coupling between different layers, as in region II.

generation is added as an additional term in the continuity equation via the nonlocal recombination 'Physical Model Interface' (PMI) in Sentaurus Device. The PMI is a plug-in mechanism which enables custom code to be used in combination with the standard device solver.

4.2 Results

In cases where luminescent coupling is neglected in the analysis of multi-junction photovoltaic devices, the device short-circuit current density is often treated as being limited by the minimum of the junction current densities, $J_{SC} = \min(J_{SC,m})$ for $m = 1$ to M, where M is the number of junctions. For the phototransducer devices presented here, this approach leads to a significant underestimation of quantum efficiency away from the design wavelength. In order to model the behavior more precisely, we modify the continuity equation to incorporate a coupled generation term, G_{coupled}, which is then solved by the device simulator. We now have relations for the divergence of electron and hole carrier concentrations, n and p,

$$\begin{aligned} \nabla n &= G_{\text{ext}} + G_{\text{coupled}} - R_{\text{SRH}} - R_{\text{Auger}} - R_{\text{rad}}, \\ \nabla p &= G_{\text{ext}} + G_{\text{coupled}} - R_{\text{SRH}} - R_{\text{Auger}} - R_{\text{rad}}, \end{aligned} \tag{4.1}$$

where G_{ext} is the generation rate due to external illumination, and R_{SRH}, R_{Auger} and R_{rad} refer to rates for SRH, Auger, and radiative recombination rates, respectively. The coupled generation term at a position B is defined with

$$G_{\text{coupled}} = \int_V K_{BA} R_{\text{rad,A}} \, dA, \tag{4.2}$$

where K_{BA} is a coupling factor relating the generation rate at any location B in the device with the radiative recombination rate at a location A. This factor is calculated using a transfer matrix method (TMM) where an interface is added at the point of emission within the structure and an internal source term is added as described in the appendix. The coupled generation is integrated over all locations A within the device volume V.

Fig. 4.3 (a) shows an example of the solution of the TMM for a single wavelength, angle of emission and polarization, with emissions occurring at a selected depth near the top of the fifth GaAs n-p junction. The real parts of the forward-and backward-propagating components of the electric field are shown, along with the magnitude of the total field. In

(b), the resulting re-absorbed energy density (fraction of emitted power re-absorbed per unit distance in the z direction) is shown, with a majority of the emissions being re-absorbed in the fifth junction and significant amounts also being coupled into the other junctions. The re-absorbed energy density drops to zero in the window and tunnel junction layers which are composed of higher band gap materials.

The overall coupling coefficient between any given source point and absorption point is a weighted integral of the re-absorbed energy density over all wavelengths, emission angles and polarizations.

Fig. 4.3 (c) presents the complete coupling matrix K, relating the coupling between a point of emission z_{A} and a point of re-absorption z_{B}. The squares along the main diagonal indicate the strength of photon recycling (re-absorption of emitted photons within the same material layer where they were emitted). In all cases the photon recycling efficiency is strong, as indicated by the brightest parts of the map. There is also significant re-absorption in some boxes which lie off of the main diagonal; these represent coupling between different GaAs junctions. It should be noted that Fig. 4.3 (b) and (c) refer only to the rate with which emitted photons are re-absorbed; in order to obtain strong luminescent coupling, there must also be strong radiative emission. If carriers are being collected much faster than their recombination lifetime or if non-radiative processes dominate, then there will be little coupling even if the coupling coefficient is high.

In order to give a sense of the relative strength of coupling, a simplifying assumption can be made that the radiative recombination rate is constant throughout each junction. In this case, a coupling coefficient linking any two junctions can be calculated by integrating over the depth of the source and destination junctions, shown in Table 4.1. This assumption of uniform emission is not made for the full device simulations which are described below because the solution is handled more exactly. Having calculated the coupling matrix K, we proceed with a complete device simulation with the coupled generation included in

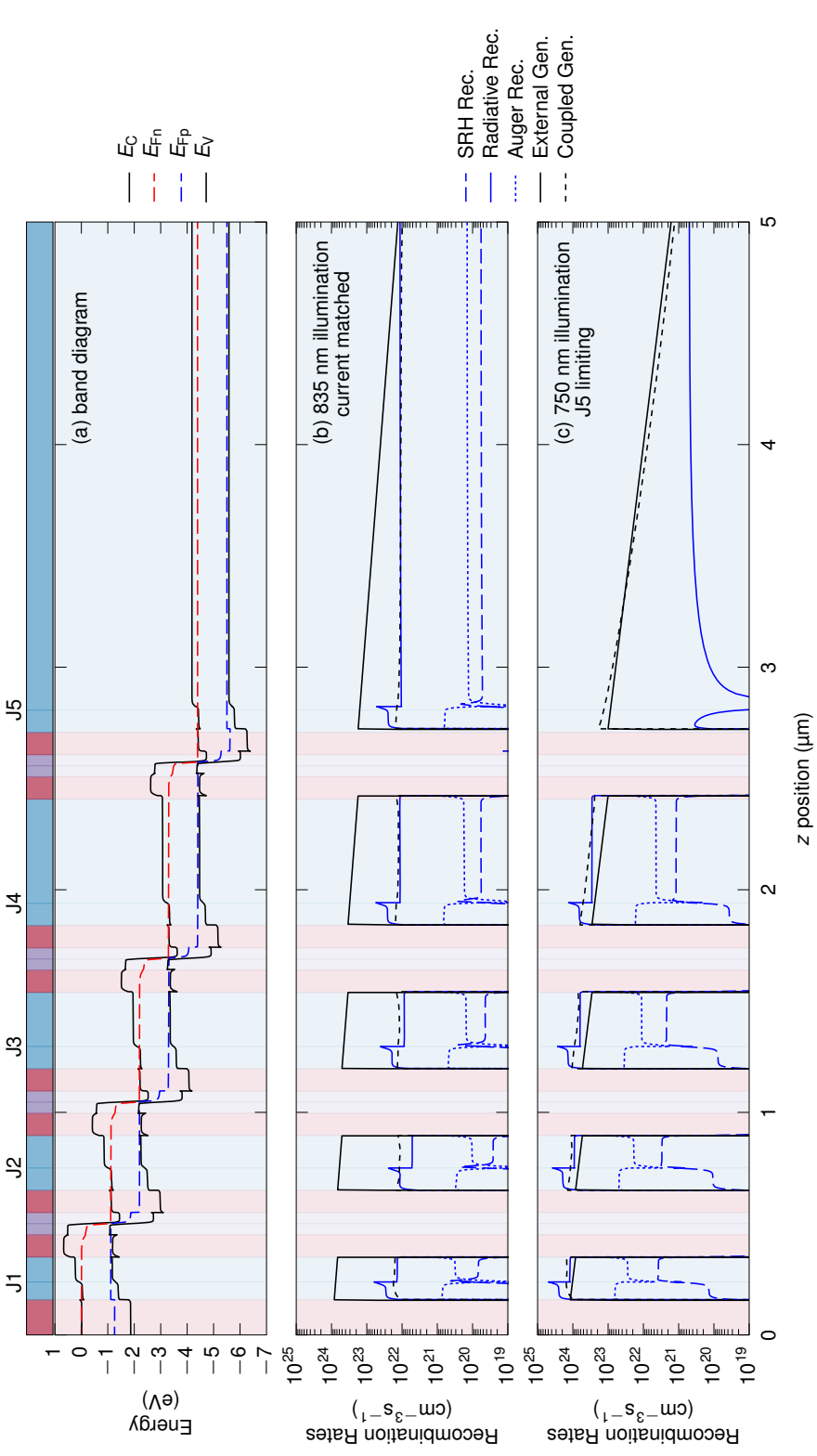

Figure 4.4: (a) Calculated energy band diagram of the 5-junction phototransducer operating at its maximum power point under 835 nm illumination. Light is incident from the left. The GaAs p-n junctions are indicated with 'J1'...'J5' and are shaded in blue; the n++-p++ tunnel junctions are shaded in purple. Generation and recombination terms are shown for the same operating conditions under illumination by (b) the design wavelength (835 nm) and (c) a wavelength causing J5 to be strongly current limiting (750 nm).

Table 4.1: Coupling coefficients indicate the coupled carrier generation rate in each junction as a fraction of radiative recombination rate in an emitting junction. The last column gives the total coupling efficiency (probability that emitted photons will be re-absorbed in any of the junctions). The highlighted diagonal values represent emission and re-absorption within the same junction.

Junction-to-junction coupling coefficients

		Re-Absorbing Junction					
		J1	J2	J3	J4	J5	Total
Emitting Junction	J1	**0.513**	0.253	0.119	0.059	0.021	0.965
	J2	0.200	**0.447**	0.212	0.083	0.027	0.969
	J3	0.067	0.151	**0.503**	0.205	0.049	0.975
	J4	0.020	0.035	0.124	**0.616**	0.185	0.980
	J5	0.002	0.003	0.006	0.041	**0.882**	0.934

the continuity equations, as in Eq. 4.1. Fig. 4.4 (a) shows the calculated cross-sectional energy band diagram for the 5-junction phototransducer while illuminated with light at its design wavelength (835 nm) and operating at the maximum-power bias voltage. The conduction band and valence band energies E_C and E_V are shown, along with the electron and hole quasi-Fermi levels E_{Fn} and E_{Fp}, respectively. In Fig. 4.4 (b), the generation and recombination terms of the continuity equation are plotted as a function of depth within the device. In this case, photogenerated carriers are generated equally and collected efficiently from all junctions so there is minimal recombination, however the radiative process is dominant compared with the Shockley-Read-Hall (SRH) and Auger processes. The radiative emissions are nearly balanced by coupled generation, leading to an increase in carrier concentrations and increased separation of the quasi-Fermi levels in each of the junctions.

In Fig. 4.4 (c), the same quantities are plotted for 750 nm illumination, which is away from the design wavelength of the device. In that case, the external photogenerated current in the bottom junction (J5) is much less than in the other junctions, leading to uncollected

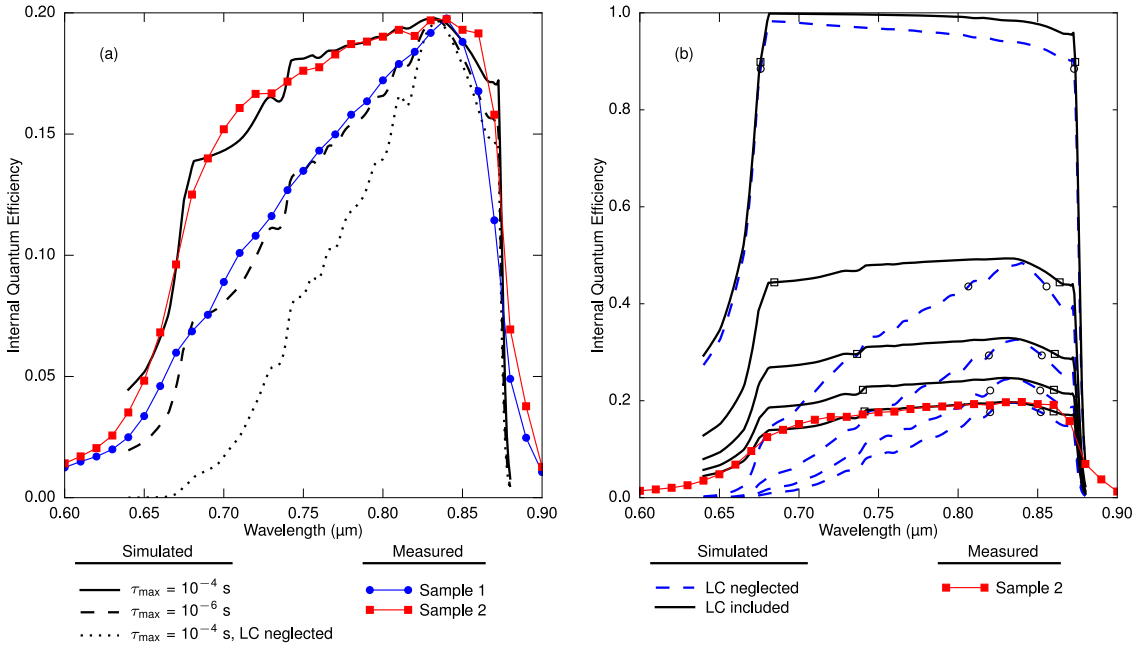

Figure 4.5: (a) Simulated and measured IQE of a five-junction phototransducer device. Photocurrent is divided over five junctions, yielding a maximum possible IQE of 0.2. (b) Simulated IQE of designs with one to five junctions. Dashed blue curves neglect luminescent coupling; solid black lines include luminescent coupling. The circles and squares indicate where each curve falls to 90% of peak. The measured IQE of Sample 2 is shown again here for reference.

photocurrent and large radiative emissions from the top four junctions. There is a net transfer of generated carriers from the top junctions into the bottom one, as evidenced by the J5 coupled generation that is much greater than the radiative emissions and comparable to the external generation in that region. From examining Fig. 4.3 (c), we can see that it is unlikely that any photon emitted from J1 or J2 would propagate all the way into J5 without being re-absorbed in one of the other GaAs regions, so this transfer relies on a very high internal radiative efficiency and good confinement of photons inside the structure to enable multiple successive re-emission and re-absorption events.

We have measured internal quantum efficiency (IQE) of two device samples from different fabrication runs (Fig. 4.5 a). The two have similar peaks in their quantum efficiencies

at 835 nm, but remarkably different IQE away from the peak despite having nominally the same layer structure. In fact, both samples have a broader IQE than would be expected if current were limited by the junction with lowest externally-generated photocurrent (i.e. without luminescent coupling, LC). Fig. 4.5 (a) also shows results of device simulations with two different values for the SRH lifetime, as well as a case where luminescent coupling has been neglected entirely. With luminescent coupling neglected, the IQE is dictated by the collected photocurrent of the bottom junction for wavelengths shorter than 835 nm, and by the collected photocurrent of the top junction for longer wavelengths. This result is independent of lifetime for $\tau_{\mathrm{max}} > 10^{-7}$ s. When luminescent coupling is included in the device simulation, we see a broadening of the IQE peak which closely resembles the broadening of the experimental device measurements. The minor discrepancy in the simulation over the wavelength range of 680-750 nm may be lessened by incorporating data from optical measurements of the as-grown epitaxial materials (e.g. absorption in the tunnel junctions) and as-deposited antireflection coating layers. Samples 1 and 2 are matched for values of $\tau_{\mathrm{max}} = 10^{-6}$ s and $\tau_{\mathrm{max}} = 10^{-4}$ s, respectively. In the latter condition, SRH and Auger recombination mechanisms have similar magnitudes, so further increases in SRH lifetime will not significantly improve performance.

As a metric to discuss the reduction in spectral sensitivity due to luminescent coupling, we consider the spectral width where the IQE exceeds 90% of its maximum (FW90M). In Fig. 4.5 (a), the FW90M of 31 nm in the simulation neglecting LC is broadened to 104 nm and 238 nm in the measurements of Samples 1 and 2, respectively.

In addition to the effect on QE, there is also a benefit to voltage of the device due to photon recycling. As was shown in Table 4.1, there is a > 40% probability that photons emitted from any of the junctions will be re-absorbed in the same junction, and > 90% probability that they are re-absorbed in one of the junctions. Combined with high internal radiative efficiency where $\tau_{\mathrm{max}} = 10^{-4}$ s, this leads to an overall increase in V_{OC} of 350 mV

for the device (70 mV per junction) under 1 W illumination compared with the case where luminescent coupling is neglected. Where $\tau_{max} = 10^{-6}$ s, the increase is 90 mV (18 mV per junction).

In the context of multi-junction solar cells, Friedman has found that the effects of photon recycling are relatively small as the coupling is uni-directional: emissions can only proceed from higher to lower band gap junctions and so there is minimal accumulation of carriers (and minimal benefit in terms of voltage) in the high-band-gap junctions [24]. Here, there is free coupling between all junctions with minimal losses, and so we find a significant voltage increase across all junctions. The fifth junction (J5) has a lower total coupling efficiency than the others, at 0.934. This is primarily because photons emitted from J5 can couple into the substrate where carriers can diffuse far from the active device layers and be 'lost'. A back reflecting structure could be helpful to prevent this, but was not included in this design.

Some researchers have used internal radiative efficiency as an input parameter to their models [27, 120]; here, the internal radiative recombination is allowed to vary freely within each layer as a function of material parameters and operating conditions, but Fig. 4.4 shows that it was typically > 90% in all GaAs layers for the SRH lifetime of $\tau_{max} = 10^{-4}$ s which matched the IQE of our Sample 1.

Applying the same analysis to simulated devices with increasing numbers of junctions we find increased spectral sensitivity, but luminescent coupling tends to mitigate this significantly, as shown in Fig. 4.5 (b) and summarized in Fig. 4.1 (b). In each case, the structure is designed to split the external optical generation evenly across all junctions at the specified illumination wavelength. The same broadening of IQE that was observed in the five-junction case is also apparent in two-, three- and four-junction designs. In the single-junction design, the thick (3.85 μm) base region and a high base doping of $9 \times 10^{17}\text{cm}^{-3}$ leads to $\sim 5\%$ loss of quantum efficiency via radiative recombination in the simulation with

luminescent coupling neglected. These losses are eliminated when LC is included in the simulation.

4.3 Conclusions

We have developed a new method for incorporating luminescent coupling and photon recycling phenomena into device simulations by adding a term to the continuity equation. This approach integrates very cleanly into the simulation process, making it possible to study these effects with no additional work required in the setup of the simulation. With the inclusion of luminescent coupling, we find very good agreement with measured five-junction devices in terms of IQE and spectral sensitivity. In general, we find that the simulation method described here is a convenient way of incorporating quantitative modeling of luminescent coupling effects into device simulations. This approach, unlike other published methods [24], avoids presupposing how these effects will manifest themselves for example in lumped parameter models as a current source term added to a particular junction. These LC effects can significantly impact the operation of photovoltaic devices through increased photovoltage, broadened quantum efficiency, and reduced sensitivity to current matching. In addition to photovoltaics, this technique can be applied to light emitting diodes, lasers and integrated photonic systems.

Acknowledgements

The authors would like to thank CMC Microsystems Inc. for providing facilities used in this project. The authors also thank the Natural Sciences and Engineering Research Council (NSERC), Ontario Centers of Excellence (OCE) and the Canada Research Chairs program for funding support. D.M. and S.F. are co-founders of Azastra Opto Inc., which is the

provider of the phototransducer device samples tested in this work.

4.A Angle of propagation in an absorbing medium

Consider a plane wave within an absorbing layer of a multi-layer stack, propagating at some angle to the normal. Since the magnitude of the electromagnetic wave must be uniform in the lateral direction, the planes of constant phase and of constant magnitude are in different directions, i.e. we are dealing with a non-uniform plane wave.

We'll assume here that the interface normals are oriented in the $\hat{z}$ direction, and the direction of propagation is in the x-z plane, though the same argument will hold for other azimuthal angles. Following a similar line of argument as Orfanidis [121], a non-uniform plane wave can be expressed as

$$\mathrm{E}(\mathrm{r}, t) = \mathrm{E}_0 e^{j\mathrm{k}\cdot\mathrm{r}} e^{-j\omega t},$$

where the complex wave vector k is defined in terms of two real vectors as $\mathrm{k} = \mathrm{k}_1 + j\mathrm{k}_2$. For consistency, the wave equation requires

$$\mathrm{k}\cdot\mathrm{k} = (\mathrm{k}_1 + j\mathrm{k}_2)(\mathrm{k}_1 + j\mathrm{k}_2) = \frac{(2\pi n_c)^2}{\lambda^2},$$
$$\mathrm{k}_1\cdot\mathrm{k}_1 - \mathrm{k}_2\cdot\mathrm{k}_2 + 2j\mathrm{k}_1\cdot\mathrm{k}_2 = \frac{4\pi^2}{\lambda^2}(n^2 - \kappa^2 + 2jn\kappa),$$

where $n_c = n + j\kappa$ is the complex index of refraction, and λ is the wavelength in vacuum. Equating real and imaginary parts,

$$|\mathrm{k}_1|^2 - |\mathrm{k}_2|^2 = \frac{4\pi^2}{\lambda^2}(n^2 - \kappa^2), \tag{4.3}$$

$$\mathrm{k}_1\cdot\mathrm{k}_2 = \frac{4\pi^2}{\lambda^2} n\kappa. \tag{4.4}$$

The time-independent part of the plane wave then expands to

$$\mathrm{E}(\mathrm{r}) = \mathrm{E}_0 e^{j\mathrm{k}_1\cdot\mathrm{r}} e^{-\mathrm{k}_2\cdot\mathrm{r}}.$$

In an absorbing medium, k_1 and k_2 may be oriented in different directions, resulting in different normals for the planes of constant phase and planes of constant magnitude. In particular, in a problem which is uniform in the $\hat{\mathrm{x}}$ direction, the k_2 vector which defines the attenuation of the wave must be oriented in the direction of the interface normal (assumed to be $\hat{\mathrm{z}}$): $\mathrm{k}_2 \cdot \hat{\mathrm{x}} = 0$. For waves propagating in a direction θ with respect to the z axis, (4.3) can be re-arranged as

$$|\mathrm{k}_1|^2 = \frac{4\pi^2}{\lambda^2}(n^2 - \kappa^2) + |\mathrm{k}_2|^2. \tag{4.5}$$

Squaring (4.4) and substituting (4.5),

$$|\mathrm{k}_1|^2|\mathrm{k}_2|^2\cos^2\theta = \left(\frac{4\pi^2}{\lambda^2}n\kappa\right)^2, \tag{4.6}$$

$$|\mathrm{k}_2|^4 + \left[\frac{4\pi^2}{\lambda^2}(n^2 - \kappa^2)\right]|\mathrm{k}_2|^2 - \left(\frac{4\pi^2}{\lambda^2\cos^2\theta}n\kappa\right)^2 = 0,$$

$$|\mathrm{k}_2|^2 = \frac{-\frac{4\pi^2}{\lambda^2}(n^2 - \kappa^2) \pm \sqrt{\left[\frac{4\pi^2}{\lambda^2}(n^2 - \kappa^2)\right]^2 + 4\left(\frac{4\pi^2}{\lambda^2\cos^2\theta}n\kappa\right)^2}}{2}.$$

$|\mathrm{k}_2|$ must be real and positive. The vector k_2 is then $|\mathrm{k}_2|\hat{z}$. $|\mathrm{k}_1|$ is given by (4.5) or (4.6), and the vector is in the direction θ. Finally, we note that the complex-valued angle of incidence of a wave with wave vector k is found from

$$\mathrm{k} \cdot \hat{z} = |\mathrm{k}| \cos\zeta,$$

$$\zeta = \cos^{-1}\frac{\mathrm{k} \cdot \hat{z}}{|\mathrm{k}|}.$$

For materials with extinction coefficient equal to zero, ζ will be the same as the angle of propagation θ. But where emissions originate from a material with non-zero extinction coefficient the complex-valued angle ζ must be used as the angle of incidence in Snell's law and to calculate Fresnel's reflectivity and transmissivity coefficients r and t.

4.B Transfer matrix method (TMM) for an internal source

As noted above, we avoid problems which can arise from interfacing regions of ray optics and regions of wave optics by treating the entire structure, including the emitting layer, with a self-consistent wave optics approach. In order to do this, we adapt the TMM for the case of emissions from a position within a planar layer stack. In the usual TMM approach, the phasors representing the magnitude of forward- and backward-propagating electric fields at the interfaces of a multi-layer stack are related using matrices (Fig. 4.6). We refer to propagation from left to right as 'forward' and right to left as 'backward'. The fields at the left and right edges of a layer i are related by a propagation matrix P_i,

$$\begin{bmatrix} E_{i\mathrm{l}}^{+} \\ E_{i\mathrm{l}}^{-} \end{bmatrix} = \begin{bmatrix} e^{-jk_{zi}d_i} & 0 \\ 0 & e^{jk_{zi}d_i} \end{bmatrix} \begin{bmatrix} E_{i\mathrm{r}}^{+} \\ E_{i\mathrm{r}}^{-} \end{bmatrix},$$

$$\begin{bmatrix} E_{i\mathrm{l}}^{+} \\ E_{i\mathrm{l}}^{-} \end{bmatrix} = \mathrm{P}_i \begin{bmatrix} E_{i\mathrm{r}}^{+} \\ E_{i\mathrm{r}}^{-} \end{bmatrix}.$$

The subscript i refers to the layer number, and l and r refer to the left and right edges of the layer. Hence E_{il}^{+} is the phasor representing the forward-propagating z-component of the field at the left side of layer i, k_{zi} is the z-component of the wave vector in layer i, and d_i is the thickness of layer i. The fields on the left and right of an interface are related by

$$\begin{bmatrix} E_{i-1\mathrm{r}}^{+} \\ E_{i-1\mathrm{r}}^{-} \end{bmatrix} = 1/t_{i-1,i} \begin{bmatrix} 1 & r_{i-1,i} \\ r_{i-1,i} & 1 \end{bmatrix} \begin{bmatrix} E_{i\mathrm{l}}^{+} \\ E_{i\mathrm{l}}^{-} \end{bmatrix}$$

$$\begin{bmatrix} E_{i-1\mathrm{r}}^{+} \\ E_{i-1\mathrm{r}}^{-} \end{bmatrix} = \mathrm{D}_{i-1,i} \begin{bmatrix} E_{i\mathrm{l}}^{+} \\ E_{i\mathrm{l}}^{-} \end{bmatrix},$$

where $r_{i-1,i}$ and $t_{i-1,i}$ are the Fresnel reflection and transmission coefficients between layers $i-1$ and i [121]. As an example, consider the layer stack in Fig. 4.6. The fields at the far left and right edges of the stack are related by

$$\begin{bmatrix} E^+_{-1\mathrm{r}} \\ E^-_{-1\mathrm{r}} \end{bmatrix} = \mathrm{D}_{-1,0}\mathrm{P}_0\mathrm{D}_{0,1}\mathrm{P}_1\mathrm{D}_{1,2}\mathrm{P}_2\mathrm{D}_{2,3}\mathrm{P}_3\mathrm{D}_{3,4} \begin{bmatrix} E^+_{4\mathrm{l}} \\ E^-_{4\mathrm{l}} \end{bmatrix}.$$

Now let us look at a case where a wave is being emitted from a position z_A within layer i=1 (Fig. 4.7). We split the propagation matrix P_i into matrices for the left and right side of z_A, and relate fields immediately to the left and right side of the newly created source interface as

$$\begin{bmatrix} E^+_{\mathrm{Al}} \\ E^-_{\mathrm{Al}} \end{bmatrix} = \begin{bmatrix} E^+_{\mathrm{Ar}} \\ E^-_{\mathrm{Ar}} \end{bmatrix} - \begin{bmatrix} E_\mathrm{s} \\ 0 \end{bmatrix}, \quad 0 \leqslant \theta < \pi/2 \tag{4.7}$$

$$\begin{bmatrix} E^+_{\mathrm{Al}} \\ E^-_{\mathrm{Al}} \end{bmatrix} = \begin{bmatrix} E^+_{\mathrm{Ar}} \\ E^-_{\mathrm{Ar}} \end{bmatrix} - \begin{bmatrix} 0 \\ E_\mathrm{s} \end{bmatrix}, \quad \pi/2 \leqslant \theta \leqslant \pi \tag{4.8}$$

where E_s is the strength of the field source at z_A, and l and r refer to the left and right sides of the source interface, respectively. We can solve for the fields emitted from the left and right sides of the stack, and then use those values to find the field at an arbitrary location in

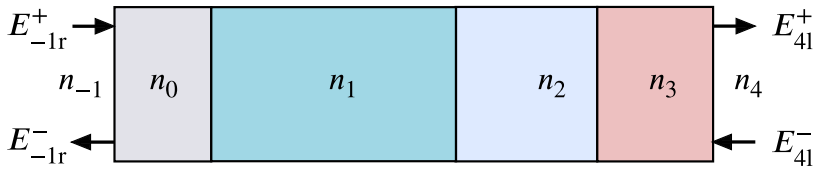

Figure 4.6: Example of terminology for the conventional TMM calculation, in the case of a 4-layer material stack.

the stack. For the portion to the left of the source we write

$$\begin{bmatrix} E^+_{-1\mathrm{r}} \\ E^-_{-1\mathrm{r}} \end{bmatrix} = \mathrm{D}_{-1,0}\mathrm{P}_0\mathrm{D}_{0,1} \begin{bmatrix} e^{-jk_{yi}z_\mathrm{A}} & 0 \\ 0 & e^{jk_{zi}z_\mathrm{A}} \end{bmatrix} \begin{bmatrix} E^+_{\mathrm{Al}} \\ E^-_{\mathrm{Al}} \end{bmatrix}$$
$$= \mathrm{L} \begin{bmatrix} E^+_{\mathrm{Al}} \\ E^-_{\mathrm{Al}} \end{bmatrix},$$

where we have defined L to contain all of the matrices to the left of the source interface. With no wave incident on the left side of the stack, $E^+_{-1r} = 0$:

$$\begin{bmatrix} 0 \\ E^-_{-1\mathrm{r}} \end{bmatrix} = \begin{bmatrix} L_{11} & L_{21} \\ L_{12} & L_{22} \end{bmatrix} \begin{bmatrix} E^+_{\mathrm{Al}} \\ E^-_{\mathrm{Al}} \end{bmatrix},$$
$$0 = L_{11}E^+_{\mathrm{Al}} + L_{12}E^-_{\mathrm{Al}},$$
$$\frac{E^+_{\mathrm{Al}}}{E^-_{\mathrm{Al}}} = \frac{-L_{12}}{L_{11}}. \tag{4.9}$$

Similarly for the right side,

$$\begin{bmatrix} E^+_{\mathrm{Ar}} \\ E^-_{\mathrm{Ar}} \end{bmatrix} = \begin{bmatrix} e^{-jk_{zi}(d_i - z_\mathrm{A})} & 0 \\ 0 & e^{jk_{zi}(d_i - z_\mathrm{A})} \end{bmatrix} \mathrm{D}_{1,2}\mathrm{P}_2\mathrm{D}_{2,3}\mathrm{P}_3\mathrm{D}_{3,4} \begin{bmatrix} E^+_{4\mathrm{l}} \\ E^-_{4\mathrm{l}} \end{bmatrix}$$
$$= \mathrm{N} \begin{bmatrix} E^+_{4\mathrm{l}} \\ E^-_{4\mathrm{l}} \end{bmatrix}.$$

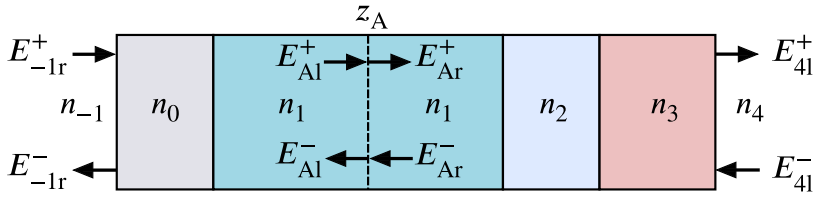

Figure 4.7: Nomenclature for the internal-source TMM calculation, with emissions from a depth z_A within layer 1.

And with $E^-_{4l} = 0$,

$$\begin{bmatrix} E^+_{Ar} \\ E^-_{Ar} \end{bmatrix} = \begin{bmatrix} N_{11} & N_{21} \\ N_{12} & N_{22} \end{bmatrix} \begin{bmatrix} E^+_{4l} \\ 0 \end{bmatrix}.$$

$$\frac{E^+_{Ar}}{E^-_{Ar}} = \frac{N_{11}}{N_{21}} \tag{4.10}$$

Applying (4.7) for a forward-propagating wave,

$$E^+_{Al} + E_s = \frac{N_{11}}{N_{21}} E^-_{Al}$$

and then substituting (4.9),

$$\frac{-L_{12}}{L_{11}} E^-_{Al} + E_s = \frac{N_{11}}{N_{21}} E^-_{Al},$$

$$\frac{L_{12}}{L_{11}} E^-_{Al} + \frac{N_{11}}{N_{21}} E^-_{Al} = E_s,$$

$$(L_{12}N_{21} + L_{11}N_{11}) E^-_{Al} = L_{11}N_{21}E_s.$$

Finally we arrive at

$$E^-_{Al} = \frac{L_{11}N_{21}}{L_{12}N_{21} + L_{11}N_{11}} E_s, \text{ and} \tag{4.11}$$

$$E^+_{Al} = \frac{-L_{12}N_{21}}{L_{12}N_{21} + L_{11}N_{11}} E_s. \tag{4.12}$$

These last expressions (4.11) and (4.12) can be computed directly by assuming a value of unity for E_s, and from there the forward and backward field components on left and right sides of the source can be found readily. The P_i and D_i matrices can then be used to determine the electric field components at arbitrary positions throughout the stack. Similarly for a backward propagating wave we can find that

$$E^-_{Al} = \frac{-L_{11}N_{11}}{L_{11}N_{11} + L_{12}N_{21}} E_s,$$

$$E^+_{Al} = \frac{L_{12}N_{11}}{L_{11}N_{11} + L_{12}N_{21}} E_s.$$

It should be noted that the transfer matrix method can suffer from issues with numerical precision in problems with highly absorbing layers. These result in matrix elements with very large and small magnitudes. Often, this problem can be addressed by recognizing that a particular layer will (in effect) completely absorb the wave entering it from the source. This layer can then be treated as a 'semi-infinite' layer bounding the stack on that side, and so the P_i matrix representing propagation through that layer (and others beyond it) can be omitted from the process of assembling the L and N matrices. Typically this decision must be made separately for every wavelength and emission angle. The TMM calculation has also been implemented using 256-bit complex floating-point numbers, i.e. each complex number is represented by a 128-bit real part and a 128-bit imaginary part. However, this on its own is not sufficient to provide an accurate solution in the case of a thick absorbing substrate.

4.C Re-absorbed energy density at a given position

In order to find the re-absorbed energy density (fraction of the emitted energy absorbed per unit distance) at a given position z_B, we first find a solution of the TMM as described in Appendix 4.B and evaluate the forward and backward components of the electric field, E^+ and E^- at z_B. The Poynting vector, S can also be evaluated at z_B, and the negative derivative of the Poynting vector gives the re-absorbed energy density. We use the same method described by Byrnes [122].

TE polarization.

Following Byrnes, we begin by writing out the electric and magnetic fields E and H at the position of interest,

$$\mathrm{E} = E^+ \hat{\mathrm{y}} + E^- \hat{\mathrm{y}}$$

$$\mathrm{H} \propto n_\mathrm{c}\, E^+(-\cos\zeta\ \hat{\mathrm{x}} + \sin\zeta\ \hat{\mathrm{z}}) + n_\mathrm{c}\, E^-(\cos\zeta\ \hat{\mathrm{x}} + \sin\zeta\ \hat{\mathrm{z}})$$

$$\mathrm{S}\cdot\hat{\mathrm{z}} = \frac{1}{2}\mathrm{Re}\left[\hat{\mathrm{z}}\cdot(\mathrm{E}^*\times\mathrm{H})\right] \propto \mathrm{Re}\left[(E^{+*} + E^{-*})(E^+ - E^-)\, n_\mathrm{c}\cos\zeta\right]$$

We evaluate the power emitted from the source using the $\hat{z}$ component of the Poynting vector, $\mathrm{S}\cdot\hat{z}$, evaluated immediately to the left and right of the source interface. The power density emitted by the source is

$$S_\mathrm{in} = (\mathrm{S}_\mathrm{Ar} - \mathrm{S}_\mathrm{Al})\cdot\hat{\mathrm{z}}. \tag{4.13}$$

This result will be used to scale each of the left-and right-propagating solutions to the required emitted power.

The negative derivative of $\mathrm{S}\cdot\hat{\mathrm{z}}$ is the absorbed power per unit distance in the z direction. Again following Byrnes, we normalize this for unit input power density,

$$a \equiv \frac{1}{P_\mathrm{in}}\frac{d}{dz}(\mathrm{S}\cdot\hat{\mathrm{z}}) = |E^+ + E^-|^2\ \mathrm{Im}(n_\mathrm{c}\, k_z\cos\zeta)/S_\mathrm{in}.$$

We refer to this quantity a as the 'absorbed energy density', with units of inverse distance.

TM polarization.

Similarly for TM polarization,

$$\mathrm{S}\cdot\hat{\mathrm{z}} \propto \mathrm{Re}\left[(E^+ + E^-)(E^{+*} - E^{-*})\, n_\mathrm{c}\cos\zeta^*\right]$$

and

$$a = \mathrm{Im}\left[n_\mathrm{c}\cos\zeta^*\,(k_z\,|E^+ - E^-|^2 - k_z^*|E^+ + E^-|^2)\right]/S_\mathrm{in}.$$

4.D Generation due to coupling

Consider a photon emission from point A in layer i, at position z_A. Assuming isotropic emission, the rate of photon emission in a direction (θ, ϕ), where θ is the polar angle relative to the surface normal and ϕ is the azimuthal angle, will be $1/4\pi R_A$ per steradian, and will be evenly split between TE and TM polarizations. R_A is the radiative recombination rate, which can be calculated from the electron and hole densities n and p, with $R = B_{rad}(np - n_{i,eff}^2)$. $n_{i,eff}$ is the effective intrinsic carrier concentration in the emitting layer. The normalized energy distribution of the emissions is [27]

$$\hat{S}(E) \approx \frac{\alpha(E)\, n_c^2(E)\, E^2 \exp(-E/kT)}{\int_0^\infty \alpha(E)\, n_c^2(E)\, E^2 \exp(-E/kT)\, dE}.$$

Let's consider the coupled generation at a point of absorption, B. In order to avoid treating the full complexity of a 2D mesh, we'll assume photons are redistributed and re-absorbed uniformly in the lateral direction; this is reasonable if a device's gridlines are small compared with either the carrier diffusion lengths or with the optical absorption lengths, and if the device is uniformly illuminated. We have already shown the absorbed energy density $a(\theta, \phi, E)$ giving the fraction of emissions from a location z_A that will be re-absorbed per unit thickness in a thin layer at z_B. Then we can write

$$G_B(\theta, \phi, E)W = a(\theta, \phi, E)\, \hat{S}_A(E)\, R_A\, V_A$$

to represent the optical generation rate at B originating from recombination in a small volume (i.e. a mesh element) V at position A. The variable W refers to the surface area of the device being simulated. This will be integrated over θ, ϕ, and E and summed over TE and TM polarizations to get the total optical coupling factor K_{BA} between mesh vertices at

A and B:

$$\frac{G_{\mathrm{B}}}{R_{\mathrm{A}}} = \frac{1}{8\pi W} \int_0^{\infty} \int_0^{\pi} \int_0^{2\pi} \Big[a_{\mathrm{TE}}(\theta, \phi, E) + a_{\mathrm{TM}}(\theta, \phi, E) \Big] \hat{S}_{\mathrm{A}}(E)\, V_{\mathrm{A}}\, d\phi \sin\theta\, d\theta\, dE$$

$$K_{\mathrm{BA}} \equiv \frac{G_{\mathrm{B}}}{R_{\mathrm{A}} V_{\mathrm{A}}} = \frac{1}{4\, W} \int_0^{\infty} \int_0^{\pi} \Big[a_{\mathrm{TE}}(\theta, \phi, E) + a_{\mathrm{TM}}(\theta, \phi, E) \Big] \sin\theta\, d\theta\, \hat{S}_{\mathrm{A}}(E)\, dE.$$

Here the limits of integration in energy are given as (0,∞), but in fact $\hat{S}_{\mathrm{A}}(E)$ only holds a significant value over a range of a few kT above and below the emitting band gap and this can be used to reduce the limits of integration in E. Prior to running the device simulator, we calculate the square optical coupling matrix, K containing coupling coefficients K_{BA} for all combinations of A and B. In theory, for a mesh with N vertices the matrix would be of size $N \times N$, but we can omit coupling coefficients for layer combinations with minimal coupling, for example emissions from a layer i to a layer j with

$$\int_0^{\infty} \alpha_j(E)\, \hat{S}_i(E)\, dE << 1/d_j,$$

With α_j being the absorption coefficient in layer j, d_j the thickness of layer j, and $\hat{S}_i(E)$ the luminescent emission spectrum in layer i. It is likely that many coefficients will be very small, and so it should be possible to omit many coefficients with minimal effect on the accuracy of the calculation.

4.E Integration with the device simulator

The model is integrated into Senaturus using the 'nonlocal generation-recombination' physical model interface (PMI) [75]. This is implemented as a C++ class which is compiled

into a shared object file and loaded by Senaturus when needed. The PMI code defines a class which performs several functions: As noted earlier, the radiative recombination rate at vertex B is given by:

$$R_{\mathrm{B}} = B_{\mathrm{rad,B}}(np - n_{\mathrm{i,eff}}^2).$$

The optical generation rate at B due to optical coupling is

$$G_{\mathrm{coupled}} = \sum_{A=0}^{N} K_{\mathrm{BA}}\ B_{\mathrm{rad,A}}(n_{\mathrm{A}}p_{\mathrm{A}} - n_{\mathrm{i,eff,A}}^2)\ V_A.$$

And so the net recombination current due to radiative recombination and optically coupled generation is

$$R_{\mathrm{elec,B}} = R_{\mathrm{hole,B}} = R_{\mathrm{rad,B}} - G_{\mathrm{coupled,B}}.$$

The optical coupling PMI must also provide Jacobian matrices for the dependencies of the electron and hole recombination rates. In this model, the dependencies are the electron and hole densities, so four Jacobian matrices can be provided:

$$\frac{dR_{\mathrm{elec,B}}}{dn_{\mathrm{A}}} = \frac{dR_{\mathrm{hole,B}}}{dn_{\mathrm{A}}} = \delta_{\mathrm{A,B}}\ B_{\mathrm{rad,B}}\ p_{\mathrm{B}} - \sum_{i=0}^{N} K_{\mathrm{BA}}\ B_{\mathrm{rad,A}}\ p_{\mathrm{A}}\ V_{\mathrm{A}},$$

$$\frac{dR_{\mathrm{elec,B}}}{dp_{\mathrm{A}}} = \frac{dR_{\mathrm{hole,B}}}{dp_{\mathrm{A}}} = \delta_{\mathrm{A,B}} B_{\mathrm{rad,B}} n_{\mathrm{B}} - \sum_{i=0}^{N} K_{\mathrm{BA}}\ B_{\mathrm{rad,A}}\ n_{\mathrm{A}}\ V_{\mathrm{A}}.$$

The method described above can significantly increase the computational cost of a simulation. In the implementation discussed here, several steps can be taken to minimize this cost: (1) the coupling coefficients are calculated only once for any given combination of z_{A} and z_{B}, which is particularly efficient if the mesh is well structured; (2) the calculation of coupling coefficients is done in parallel, using all available processors; (3) the Sentaurus device simulation is also executed in parallel, with each device region being handled by a separate thread; and (4) in the case of steady-state simulations, the off-diagonal elements of the Jacobians are omitted. This last measure vastly reduces memory requirements and the size

of the matrices which must be handled by the non-linear solver. The off-diagonal elements of the Jacobians cannot be omitted in the case of transient (time-dependent) simulations.

Chapter 5

Luminescent coupling in 12-junction PPCs

Matthew Wilkins, Christopher E. Valdivia, Sanmeet Chahal, Masanori Ishigaki, Denis P. Masson, Simon Fafard and Karin Hinzer

This is a reproduction of an article presented at SPIE Photonics West in San Francisco, February 2016, describing the extension of the luminescent coupling model to 12-junction devices. In the process, some improvements were made to our device modeling process which made the model much more predictive. In particular, in the previous chapter an unexpectedly long minority carrier lifetime was required to achieve agreement between simulated and modeled quantum efficiency. After revising our optical properties of the AlGaAs layers used in this work, we were able to use lifetimes derived from measurements of single-junction devices to predict the quantum efficiency of 12-junction devices. The model including luminescent coupling provided a close match to measured performance with no fitting required.

5.1 Introduction

Monolithic, multi-junction phototransducers are used to provide optical-to-electrical power conversion with output voltages of several volts from a single device [39]. They have applications in power-over-fiber systems and for optically isolated power supplies [118]. A specific example of this is the switching power converter using modern SiC MOSFETs. These converters operate most efficiently with a higher gate voltage slew rate (dV/dt) than more conventional Si insulated gate bipolar transistors (IGBTs) [123]. In order to achieve this high slew rate, and also to minimize electromagnetic interference (EMI), isolated power supplies with minimal capacitive coupling are needed for each of the high-side transistor gate drivers. This requirement could be met with a high-power optocoupler incorporating a 12 V phototransducer.

We are reporting on a phototransducer device from Azastra Opto Inc. using their Vertical Epitaxial HeteroStructure Architecture (VEHSA) technology [124], containing 12 partially absorbing GaAs junctions and providing over 14 V at open circuit [20]. Given that we have 12 junctions of the same material but different thicknesses, it is interesting to consider photon recycling and luminescent coupling phenomena. Where GaAs junctions are producing more photocurrent than the limiting junction, the excess current recombines primarily through radiative recombination, leading to the emission of photons at or above the GaAs band gap energy. These emitted photons can be re-absorbed in the same junction where they were emitted (photon recycling) leading to increased carrier densities and voltage. Alternatively, they can be absorbed in another junction (luminescent coupling) which may help to equalize photocurrent between junctions and reduce wavelength sensitivity.

These effects have been studied previously in single junction [27, 114, 115, 120, 125] and

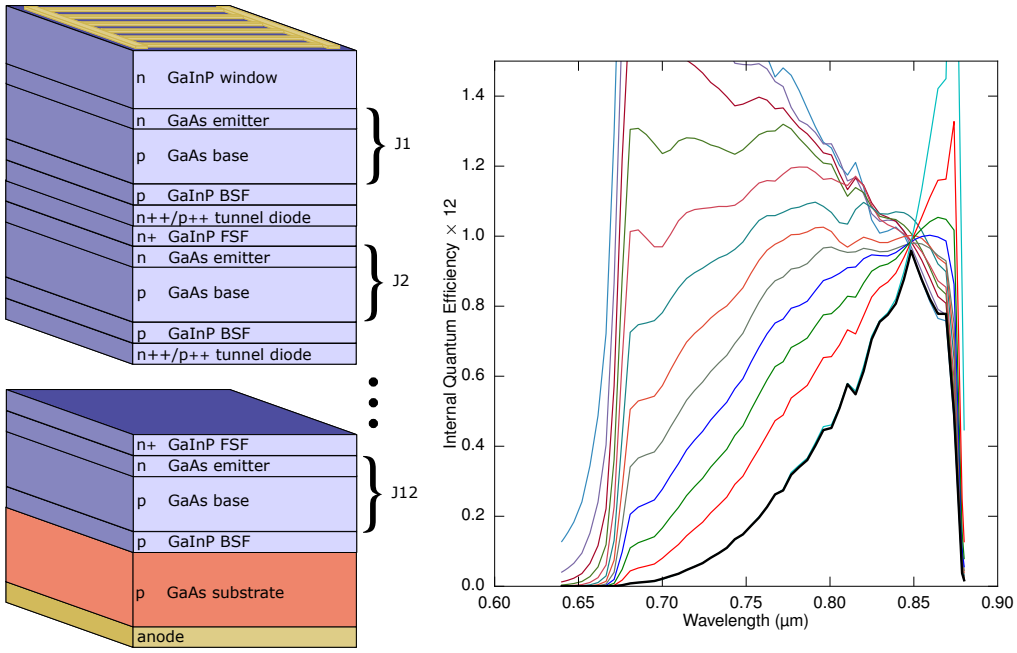

Figure 5.1: (a) General structure of the 12-junction VEHSA phototransducer (PT12). (b) Simulated quantum efficiency in the absence of any luminescent coupling. The heavy black line is the overall device quantum efficiency, and the thinner lines show photogenerated currents in each junction.

multi-junction [24, 26, 29, 34, 108, 113] solar cells, but in those cases the coupling is usually limited to one direction (from a higher-bandgap to a lower-bandgap subcell) and emissions from any subcell are coupled only to the next lower bandgap. By contrast, in the devices studied here emissions can be coupled into all other junctions due to the equal bandgaps and the fact that most junctions are optically thin (semi-transparent).

5.2 12-junction phototransducer

The device structure is illustrated in Figure 5.1 (b), with individual junctions labeled J1, J2, etc. It resembles a multi-junction solar cell, except that it is designed to operate with monochromatic illumination at a wavelength of 850 nm. For that reason, all junctions are

of the same material (GaAs), and sharing of photocurrent between junctions is achieved by varying the thickness of each junction. An ideal device, then, should have a quantum efficiency of 1/12 at 850 nm. At wavelengths other than the design point, we can expect that the junction photocurrents will be unequal with current being limited to the lowest photocurrent. This would lead to reduced short-circuit current and power conversion efficiency (Figure 5.1 b). The devices have an aperture of 2.1 mm diameter and are optimized for 1 to 5 W incident optical power. They have been shown to have 14.5 V open-circuit voltage and have demonstrated >60% power conversion efficiency when measured up to 3 W of optical input at a wavelength of ~ 850 nm [20, 21].

5.3 Luminescent coupling

We have developed a method for incorporating the modeling of photon recycling and luminescent coupling phenomena into a drift-diffusion based device simulation [45,46,111]. Prior to running the simulation, a coupling coefficient K_{BA} is calculated to determine the fraction of luminescent emissions emitted from a depth A within the device which will be re-absorbed at any other point B. The calculation is done using a transfer matrix method technique allowing for emissions from locations within the layer stack [111].

The coupling factor K_{BA} is plotted in Figure 5.2. As might be expected, the strongest coupling is found in the squares along the diagonal indicating photon recycling (re-absorption in the same layer as the emission). Light-coloured rectangles above the main diagonal indicate coupling in the downward direction, from J1 into J3 for example. For convenience, this coupling matrix is approximated with per-junction coefficients, giving the ratio of generation current to radiative recombination current in any combination of junctions, presented in Table 5.1. The rightmost column gives the sum of the coefficients for a given emitting junction. These totals are all less than 1, indicating that some emitted light escapes

the device entirely or is absorbed in layers other than the photovoltaic junctions. It should be noted that the coupling factor K_{BA} refers only to efficiency with which emitted light is coupled; some layers may have a large K_{BA}, but will not emit light at all due to having low internal radiative efficiency or low carrier concentrations. These factors are accounted for in the next step, the device simulation. The simulations are run in Synopsys Sentaurus, using a custom plug-in module which adds an extra generation term to the electron and hole continuity equations to account for the coupled generation. Complete details of the luminescent coupling model are presented in reference [111]. Sentaurus includes several non-radiative recombination mechanisms, and so the non-linearity of coupling due to competition between radiative and non-radiative mechanisms [26, 35] is implicitly included, and is accounted for on an element-by-element basis. The 'maximum' lifetime for the Shockley-Read-Hall (SRH) process was calibrated against samples of individual subcells at 200 ns. This value is reduced using a doping-dependent model according to the doping in each layer.

5.4 Results

Measured quantum efficiency of the 12-junction phototransducer devices is much broader than predicted by simulations that neglect luminescent coupling (Figure 5.3), with a significant response extending all the way to the absorption band edge of the window layer at ~ 650 nm. At 90% of the peak value, the width of the QE response is 84 nm, 4.0 times the width that we calculate without luminescent coupling. The QE measurements were done with a relatively low beam intensity yielding only 1.8 V of open-circuit voltage on the full device, while individual junctions were found to break down at >6 V of reverse bias, so we discard the possibility that some junctions are in reverse breakdown in the measurement.

When luminescent coupling is included in the simulation we also see a significant

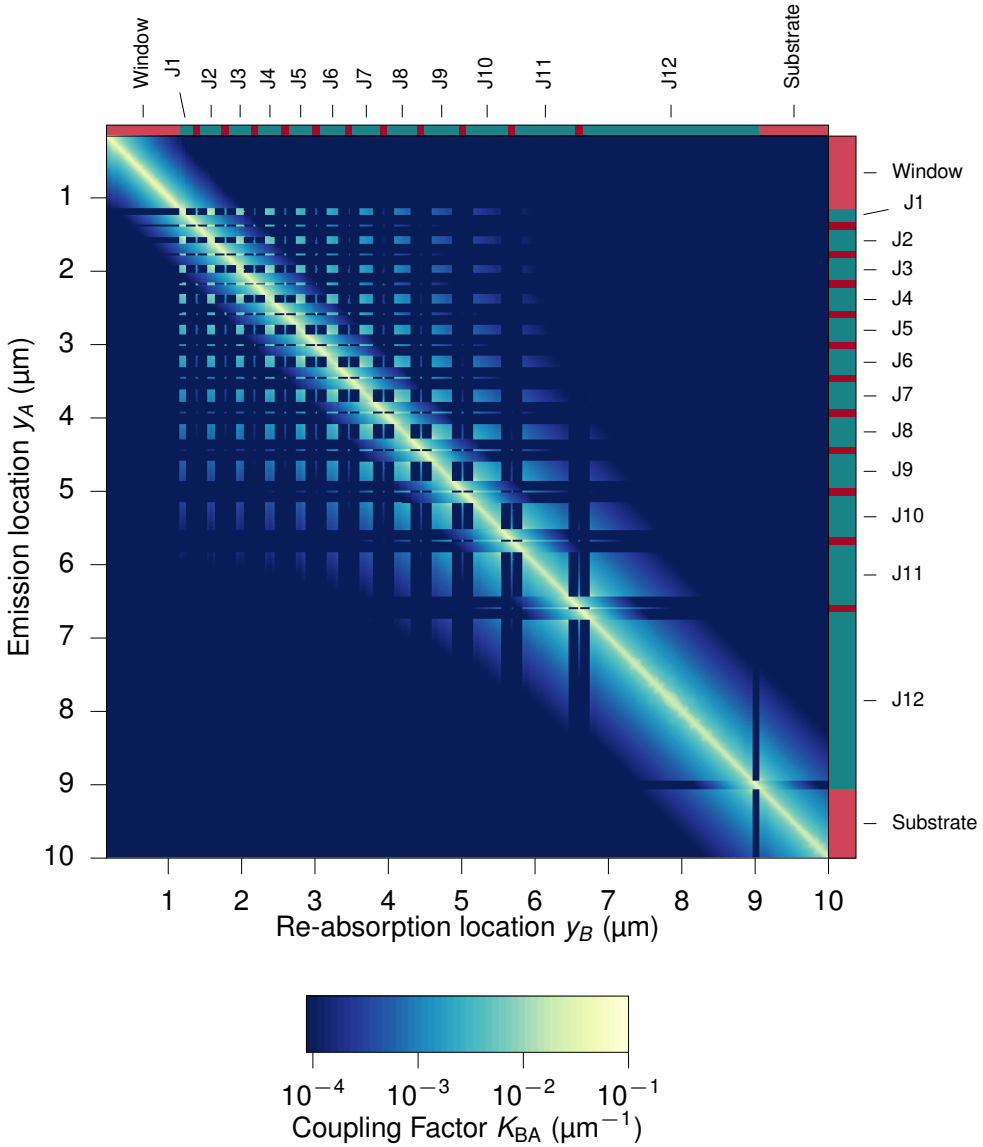

Figure 5.2: The coupling factor K_{BA} is plotted for all emission locations y_{A} and re-absorption locations y_{B}. Values are highest along the main diagonal, indicating re-absorption near the point of emission (photon recycling). Light colored boxes away from the diagonal indicate luminescent coupling between different regions.

Table 5.1: Coupling coefficients indicate the coupled carrier generation rate in each junction as a fraction of radiative recombination rate in an emitting junction. The last column gives the total coupling efficiency (probability that emitted photons will be re-absorbed in any of the junctions). The highlighted diagonal values represent emission and re-absorption within the same junction.

Junction-to-junction coupling coefficients

		Re-Absorbing Junction												
		J1	J2	J3	J4	J5	J6	J7	J8	J9	J10	J11	J12	Total
Emitting Junction	J1	**0.33**	0.20	0.12	0.08	0.06	0.05	0.03	0.03	0.02	0.01	0.01	0.00	0.94
	J2	0.15	**0.31**	0.16	0.10	0.07	0.05	0.04	0.03	0.02	0.01	0.01	0.00	0.94
	J3	0.08	0.15	**0.28**	0.15	0.09	0.06	0.04	0.03	0.02	0.01	0.01	0.00	0.94
	J4	0.06	0.08	0.13	**0.28**	0.15	0.09	0.06	0.04	0.03	0.02	0.01	0.00	0.95
	J5	0.04	0.05	0.07	0.13	**0.30**	0.15	0.08	0.05	0.03	0.02	0.01	0.00	0.95
	J6	0.02	0.03	0.04	0.07	0.13	**0.32**	0.16	0.08	0.05	0.03	0.02	0.01	0.95
	J7	0.02	0.02	0.03	0.04	0.06	0.13	**0.34**	0.17	0.08	0.04	0.02	0.01	0.96
	J8	0.01	0.01	0.01	0.02	0.03	0.06	0.14	**0.38**	0.18	0.08	0.04	0.01	0.96
	J9	0.01	0.01	0.01	0.01	0.02	0.03	0.05	0.14	**0.43**	0.19	0.07	0.02	0.97
	J10	0.00	0.00	0.00	0.01	0.01	0.01	0.02	0.04	0.13	**0.51**	0.19	0.04	0.97
	J11	0.00	0.00	0.00	0.00	0.00	0.00	0.01	0.01	0.03	0.12	**0.63**	0.18	0.98
	J12	0.00	0.00	0.00	0.00	0.00	0.00	0.00	0.00	0.00	0.01	0.05	**0.89**	0.95

broadening in the QE response, which shows good agreement with the measured QE as shown in Figure 5.3. No parameter fitting was needed to obtain this agreement; all material parameter values were obtained from the literature except the SRH lifetime which was determined from individual subcell devices. There remains a small discrepancy between measured and simulated data between 650 and 750 nm though, which seems to indicate that our model has an excess of absorption in the AlGaAs interconnecting layers. In *J-V* curve calculations, open-circuit voltage is increased by 580 mV (48 mV per junction) when luminescent coupling and photon recycling are included in the limit of high internal radiative

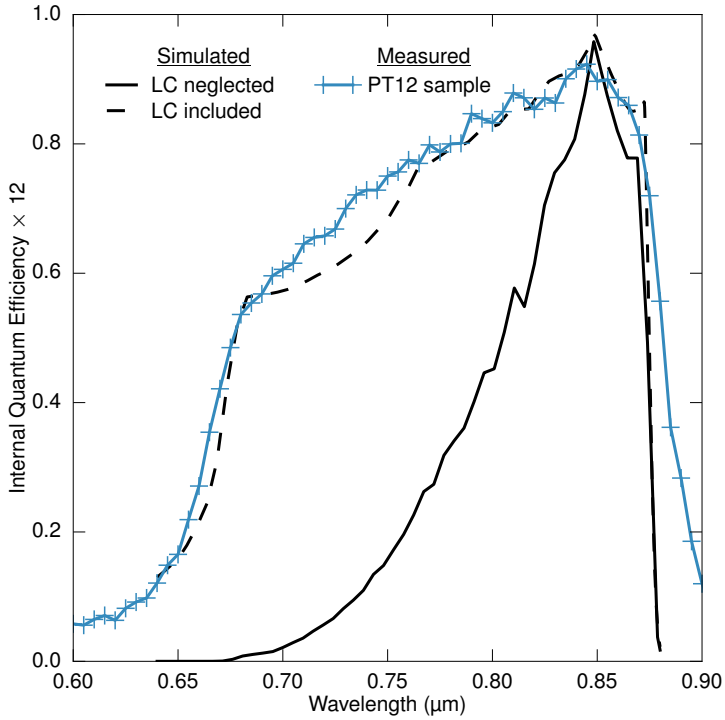

Figure 5.3: Internal quantum efficiency of the full device from measurements (blue), plus simulations without luminescent coupling (solid black), and with luminescent coupling (dashed black).

efficiency. This is consistent with results from very high quality GaAs single junctions. Using the 200 ns SRH lifetime which was found for the single junctions, photon recycling yields a 240 mV increase in open-circuit voltage (20 mV per junction), contributing 1.7% of the total V_{OC}.

Chapter 6

Applications of PPCs

Matthew Wilkins, Masanori Ishigaki, Christopher E. Valdivia, Philippe-Olivier Provost, Denis P. Masson, Simon Fafard and Karin Hinzer

This article discusses the application of 12- and 20-junction photonic power converters in power electronic circuits. The PPCs are coupled to a vertical-cavity surface emitting laser (VCSEL) array where they can provide a ripple-free power supply as well as galvanic isolation and high immunity to EMI. It has not yet been accepted for publication.

Recent advances in multi-junction photonic power converters (PPCs) have enabled monolithic GaAs photovoltaic (PV) devices with 5, 12 or 20 p-n junctions vertically stacked for an open-circuit voltage up to 23 V [22], and tenfold higher power densities compared to previous designs. Power conversion efficiency demonstrated by these PPCs reaches >60-65% [20, 22, 118] under single-wavelength illumination, at average power densities [22] up to 150 W/cm^2. Here, we couple such a device with a diode laser to yield a step-up DC voltage converter with very high impedance to conducted electromagnetic interference

(EMI) and without ripple. We demonstrate the use of this laser/PPC pair as a regulated photonic boost converter producing a regulated 12 V output from 3.3 V input, and find no measurable ripple. For a second application, we use the laser/PPC to power a 650 V MOSFET gate driver requiring high galvanic isolation. In that case we measure a 20 dB reduction in EMI current conducted from the power circuit into the low-voltage control systems.

Photonic power converters are photovoltaic devices designed for producing power under illumination by a laser or a light-emitting diode. They have been proposed in the past for power-over-fiber and other systems needing extreme galvanic isolation, but they could also be used in much more ubiquitous applications for DC power supplies in instrumentation, power electronics and other systems. Since most power supply requirements call for a voltage of several volts, it is advantageous to connect several PV junctions in series to produce the desired output. In some cases this has been done by segmenting a single planar junction into pie-shaped mesas which are isolated and connected in series via microfabrication [38, 126, 127]. More recently, vertically-stacked PPCs with a structure similar to that of multi-junction solar cells have been demonstrated, with two [36, 37], 5, 12 and 20 junctions [20, 21]. This vertical structure enables high conversion efficiencies and high power densities.

Coupling of laser and PPC

Since the absorption coefficient is wavelength dependent, PPCs with the vertical architecture must be designed for optimal operation at a specific wavelength. Photocurrent is generated equally in each of the N series junctions through a careful choice of layer thicknesses. Starting from the top, each optically-thin junction is designed to absorb $(1 - t)/N$ of the incident light. A small fraction, t <1%, passes through all junctions without being absorbed.

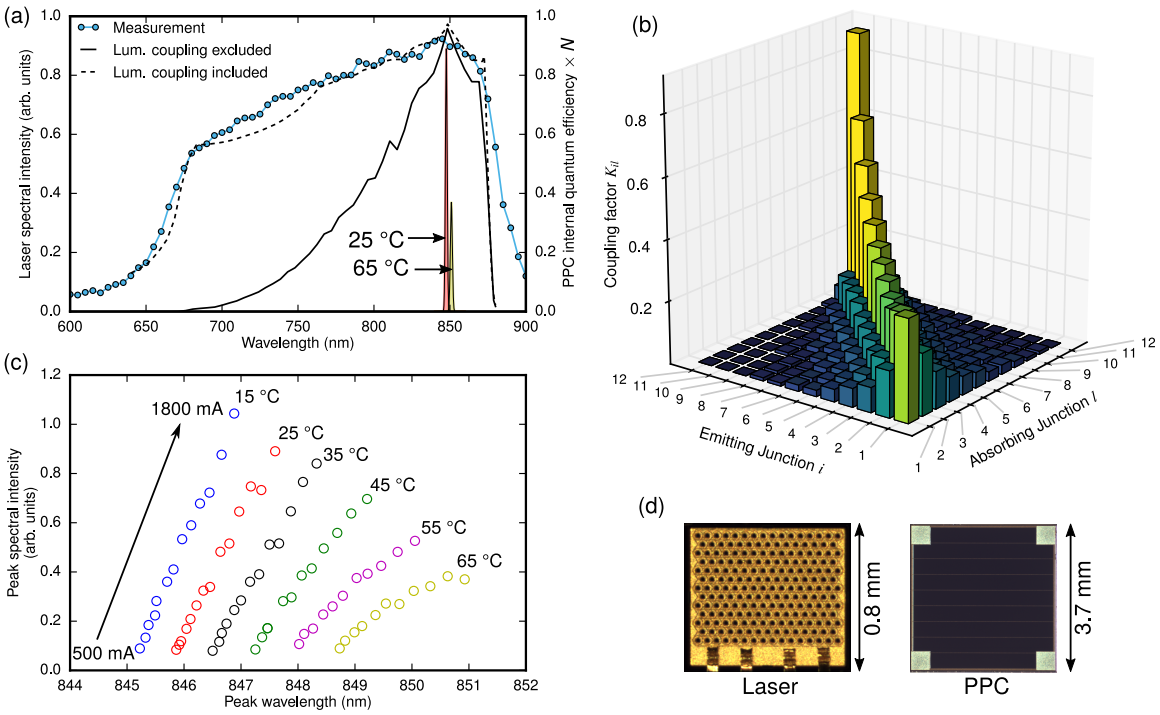

Figure 6.1: Wavelength-matching of the laser diode and PPC. (a) Measured internal quantum efficiency of the N=12 junction PPC (blue dots), compared to simulations including (dashed) and excluding (solid) the effects of luminescent coupling. Measured laser emission spectra are shown at two temperatures. (b) Coupling factors K_{il} indicate the fraction of emissions from a junction i that will be absorbed in junction l. The main diagonal gives the probability that emissions are re-absorbed in the junction where they were emitted (photon recycling). This probability is highest in the junctions near the bottom which are thickest, and also rises near the top where there is an internal reflection from the top surface of the PPC. (c) Laser wavelength and peak intensity for varying temperature and applied current. (d) Top-view images of the laser array and PPC.

Measured internal quantum efficiency for the N=12 PPC is shown in Fig. 6.1a, along with emission spectra from a matching laser diode.

We might expect that this wavelength sensitivity would increase for increasing N, however experiments have shown essentially no change in wavelength response for 5, 6, 12 or 20-junction devices [22]. This is explained through the phenomenon of luminescent coupling [27, 31, 33]: where one junction is absorbing more than its share of incident photons, the excess is re-emitted as photons with energy near the material band gap.

These photons are re-absorbed in the other junctions, leading to an efficient re-distribution of photocurrent between the junctions [40, 111, 128]. A coupling coefficient K_{il} can be calculated, giving the fraction of emitted photon flux from a given junction i which will be re-absorbed in another junction l. These coefficients are plotted for the 12-junction device in Fig. 6.1b. The total photocurrent density in junction l is then $J_{\mathrm{ph},l} + \sum_i K_{il} J_{\mathrm{rad},i}$, where $J_{\mathrm{ph},l}$ is the photocurrent density in junction l due to light incident on the PPC, and $J_{\mathrm{rad},i}$ is the recombination current density via radiative processes in junction i. Although the coupling is strongest between junctions near the diagonal (i.e. between junctions that are located close together), there can be a significant transfer of photocurrent between distant junctions through multi-step processes. Photons emitted from any junction have a >94% probability of being re-absorbed rather than escaping the device.

This redistribution of light and resultant photogeneration yields a broadened internal quantum efficiency, shown for a 12-junction PPC in Fig. 6.1a. With luminescent coupling excluded from the simulation, the device's short-circuit current is limited by the p-n junction with the lowest photogenerated current, leading to a strong sensitivity to wavelength (-1.1%/nm) near the design point of 850 nm. When the effects of luminescent coupling are included, this sensitivity is reduced to -0.4%/nm and closely follows experiment. In Fig. 6.1a we also show measured spectra of a laser diode array at temperatures of 25°C and 65°C. The current- and temperature-dependence of the emission peak are in Fig. 6.1c. Although the laser is nominally well-matched to the PPC, the laser shifts by 1.4 nm/A and 0.08 nm/°C. Consequently, reduced wavelength sensitivity due to luminescent coupling is important to maintain high efficiency of operation without temperature stabilization of either the laser or the PPC.

The laser and the PPC are separated by an air gap of 3 mm. The laser diode emits with a peak electrical-to-optical efficiency of 42%. Current-voltage and efficiency characteristics are shown in Fig. 6.2a and b. The photovoltaic power converter used here has 12 GaAs

junctions and provides a voltage of 14.5 V under open-circuit conditions and 12.4 V at maximum power. At 25°C, optical-to-electrical power conversion efficiency is 55% with 1 W of optical power, and is >50% over a wide range of optical power up to at least 150 W/cm^2 (Fig. 6.2c).

Combined, the laser diode array and PPC provide a step-up in voltage from 2.5 V to 14 V. The laser can be operated at DC (Fig. 6.3a), producing no high-frequency switching and hence no internally generated EMI. Alternatively, it can be regulated in a pulse mode such that it operates at its maximum efficiency independent of the load at the output. Overall the coupled laser/PPC pair has an efficiency of 23%.

Ripple-free boost converter

Conventional technology for step-up DC/DC conversion requires a 'boost converter' circuit as shown in Fig. 6.3b where a voltage is applied to an inductor to establish a current, and the current is then switched to charge a capacitor. This leads to a characteristic 'ripple' in the output voltage as the regulator switches on and off. Additionally, there is a 'ringing' of the circuit at its resonant frequency, forced by the switching impulses.

As our baseline for comparison, we assembled a switching boost converter with this topology, described in greater detail in the Methods section. Noise and ripple of this circuit are shown in Fig. 6.3c and d. When the L-C filter is bypassed, we measure a root-mean-square (RMS) ripple of 2.48 mV (35.9 mV peak to peak), tabulated in Fig. 6.1. The ripple is reduced to 0.49 mV RMS (7.76 mV peak to peak) with the L-C filter active.

For our photonics-based topology, a diode laser was coupled to a 12 V photonic power converter and connected to the output of a linear regulator to produce a step-*up* converter (Fig. 6.3a) that is free of ripple, ringing and EMI emissions. It converts the 3.3 to 3.7 V commonly available from a single lithium polymer (Li-Po) battery cell to a regulated 12 V

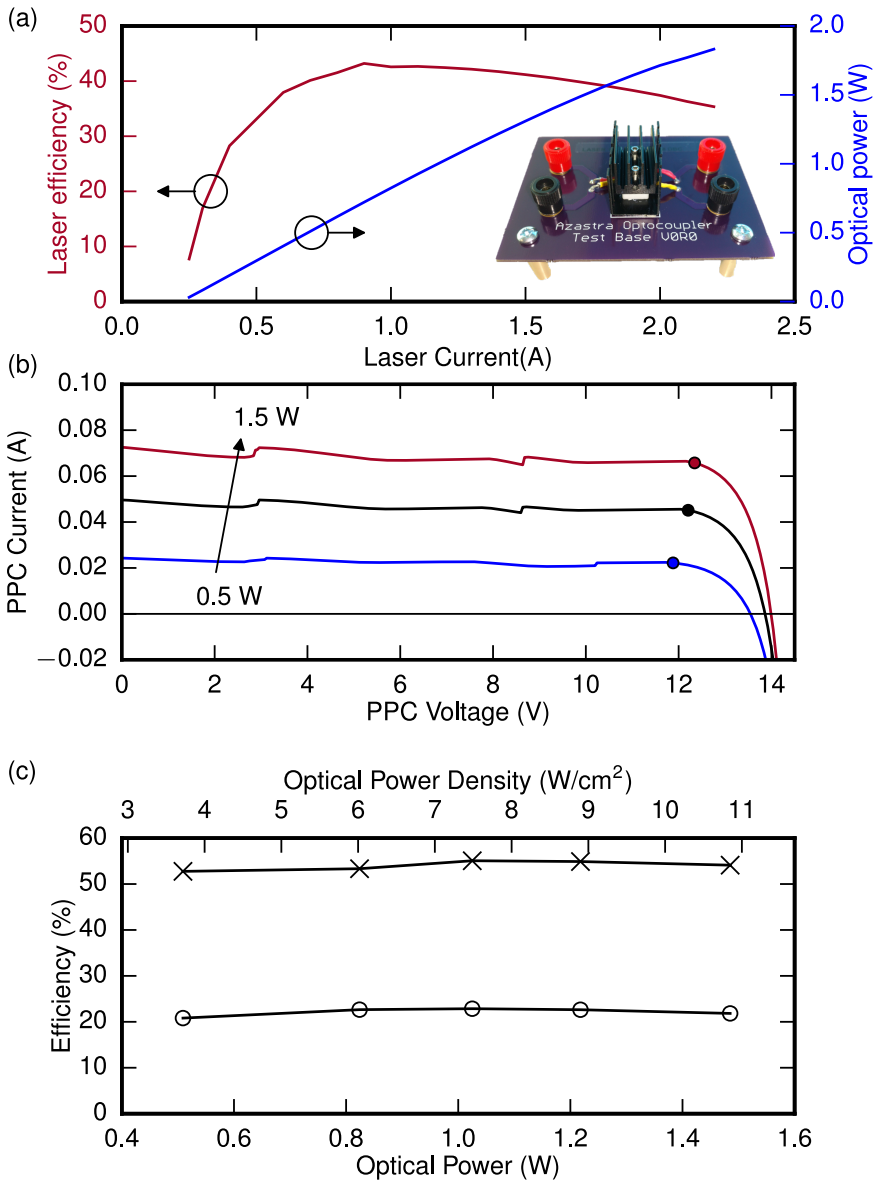

Figure 6.2: Terminal characteristics of the optically isolated DC power supply. (a) Laser diode efficiency and optical power for a nominally 1 W laser diode array at 25°C. Inset: image of the coupled laser/PPC package. (b) Currrent-voltage characteristics for the PPC at the same temperature for illumination of 0.5, 1 and 1.5 W and (c) efficiency of the PPC (×) and the complete power converter (∘) are shown as a function of optical power and optical power density on the bottom and top scales, respectively.

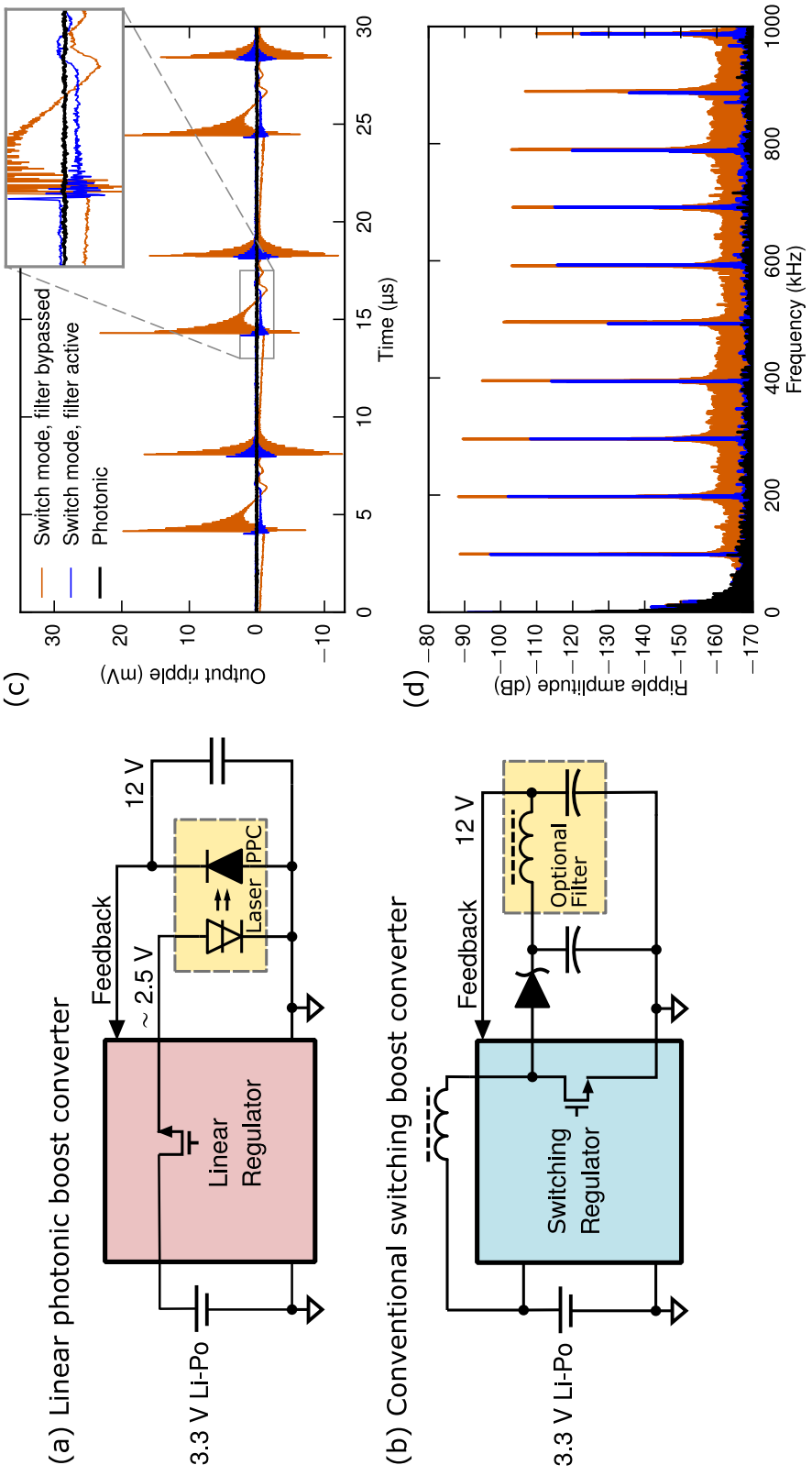

Figure 6.3: Performance of a regulated boost converter. (a) Photonic boost converter topology. (b) Conventional switching boost converter topology. The L-C filter at the output is optional. (c) Ripple of the switching and photonic boost converters in the time domain. (d) FFT of the same data, referenced to the 12 V DC output voltage. The noise floor is higher in the orange dataset because a different gain setting was required. (e) Power draw and output ripple of the two boost converter designs.

	Power Draw (W)		Ripple (mV)	
	No load	With load	RMS	p-p
Switching, filter bypassed	0.044	0.56	2.48	35.9
Switching, filter active	0.044	0.56	0.49	7.76
Photonic	0.92	3.4	<0.045	<0.33

Table 6.1: Power draw and output ripple of the two boost converter designs.

output. Feedback from the output allows the regulator to control current to the laser diode and maintain the required output voltage. With no load, the converter draws 280 mA which is just below lasing threshold; with a 330 Ω resistive load the current draw is 986 mA. Using an oscilloscope sampling at 2×10^9 samples/s and limited to 20 MHz analog bandwidth, we were unable to detect any ripple above the 0.33 mV peak-peak (0.045 mV RMS) background noise of our instrument. This data is shown in Fig. 6.3c (time domain) and Fig. 6.3d (frequency domain).

In the frequency domain (Fig. 6.3d), the switching circuit produces harmonics at multiples of the switching frequency, 100 kHz. In contrast, the photonic boost converter shows no significant frequency content over the 50 kHz - 20 MHz range.

Photonically isolated gate drive power supply

Next we consider a second application in power electronics. Wide bandgap transistors, and particularly SiC metal-oxide-semiconductor field-effect transistors (MOSFETs), are increasingly available and are being integrated into power electronics systems [129–133]. The small gate capacitance and the majority-carrier nature of SiC MOSFETs promises fast switching times and reduced switching losses when compared with established technology based on silicon transistors. These increases in switching speed come with increased EMI and gate instability [134].

The power supply to the gate driver typically is isolated using a transformer which has a larger stray capacitance and offers a path for conducted EMI. To investigate the impact of a *photonic* power supply to the gate driver on switching performance and EMI, we used a double-pulse test setup [134–136] (Fig. 6.4a-c). The setup simulates one leg of a three-leg power inverter, comparable to what is used in hybrid-electric vehicle drive systems. We establish a 90 A current in the load inductor and then measure waveforms during a single on/off pulse lasting 0.67 µs. The gate drive power supply is used to provide an isolated 13 V to the MOSFET gate driver.

As the MOSFET Q_1 switches as in Fig. 6.5a, its source and drain terminals undergo rapid changes in potential. The output sides of the gate drive optoisolator and its power supply are also subjected to these potential swings. Both devices have a finite capacitance between the input and output C_{gd} and C_{ps}, and so in a simplistic analysis any switching event must lead to a common-mode EMI current from the outputs back to the low-voltage control circuitry at the inputs,

$$i_{CM} = (C_{gd} + C_{ps})\, dV_{DS}/dt. \tag{6.1}$$

For the photonic power supply, the stray capacitance between laser and PPC chips is only 60 fF; the capacitance between heatsinks on the laser and PPC sides is larger for a total C_{ps}=0.4 pF. As a benchmark, we also tested a more conventional supply with a DC/DC converter integrated circuit where isolation is provided by a transformer. This solution has a larger capacitance C_{ps} of 40 pF, due to primary and secondary winding of the transformer being wound in close proximity on a magnetic core.

Switching behavior is shown in Fig. 6.5a-c. The drain-source voltage across the SiC MOSFET, V_{DS} is plotted in (d). Large switching transients are produced at turn-off and settle out after 0.3 µs. In Fig. 6.5b we show a common-mode EMI current measured on the power supply cable leading to the digital control electronics which generate switching signals for

the MOSFET. With the transformer-based power supply the EMI current reaches a peak of 0.64 A, while the photonic circuit reaches 0.25 A peak. A third measurement with the current probe removed from the wires shows a peak of 0.1 A, indicating that the measurements are partly obscured by EMI picked up directly by the instrument. However, the background signal is consistent, and smaller than either of the EMI current measurements.

A frequency analysis of the EMI currents is shown in Fig. 6.5c. The photonic-based gate drive power supply reduces EMI by 20 to 30 dBμA over the 0 to 10 MHz range. The largest peak in the EMI from the transformer-based power supply, 96 dBμA at 5.3 MHz, is reduced by 38 dBμA with the photonic power supply (a factor of 80 reduction). With both the transformer-based and photonic power supplies, we find peaks at 45 MHz and 65 MHz; these peaks are largely unaffected by the choice of power supply and may be coupled through the optoisolator, C_{gd}. Hence the gate drive power supply capacitance C_{ps} is no longer the most significant path for conducted EMI in the photonic configuration.

In summary, PPCs enable the creation of a unique class of step-*up* voltage converters which have practical output voltage in the range of 5, 12, or 24 V while causing no ripple, ringing or EMI. We have demonstrated a photonic boost converter with no measurable ripple. When compared with a switching boost converter, we found a 60 to 80 dB reduction in harmonic content over a broad frequency range. We also demonstrated an isolated DC supply applicable to electric vehicle applications which reduces EMI conducted to the signal-level electronics. It provides a 20 dB improvement, again limited primarily by measurement noise. These emerging applications leverage the significant advances in laser diode and multi-junction solar cell technology developed in recent years, and are a potential new market for photonic devices.

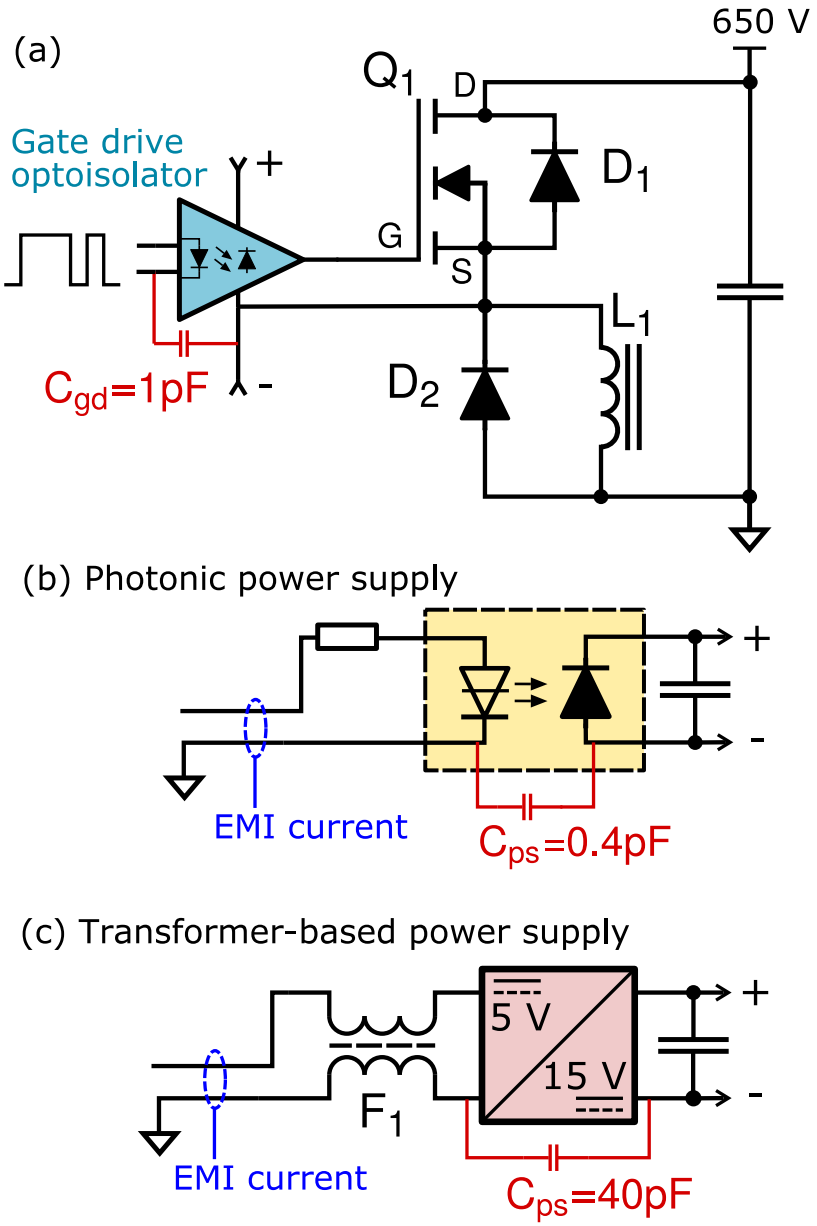

Figure 6.4: (a) Double-pulse switching circuit used to test the effects of different gate drive power supplies. Parasitic capacitances which provide a path for EMI currents are shown in red. (b) Optically isolated power supply, which provides a floating power supply for the gate drive optoisolator, and (c) conventional DC/DC converter with transformer isolation.

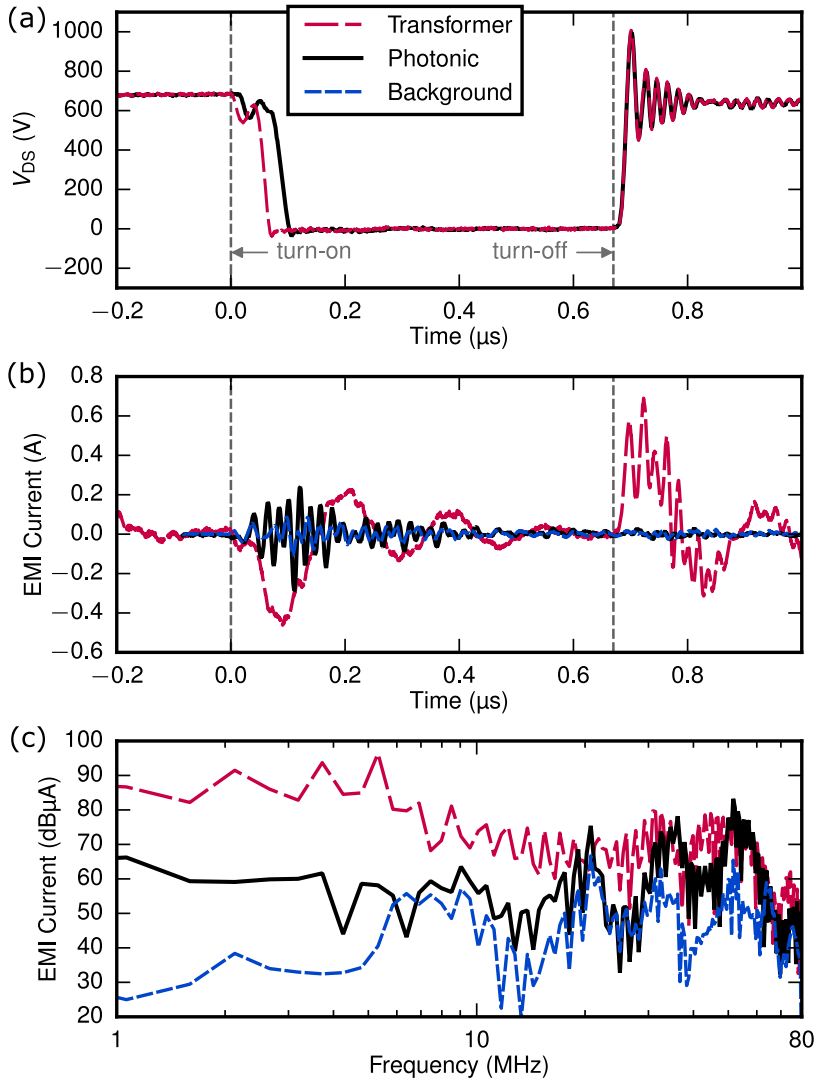

Figure 6.5: (a) Switching waveforms using conventional and optically-isolated gate power supplies. (b) Measured EMI currents through the transformer-based and photonic power supplies. A reference measurement with the current probe disconnected is also shown. (c) Frequency-domain representation of the EMI current.

Methods

Laser and PPC devices The laser used is a commercially available vertical-cavity surface-emitting laser (VCSEL) array emitting nominally 1 W at 850 nm. The PPCs are designed and manufactured by Azastra Opto Inc. based on the vertical epitaxial heterostructure architecture (VEHSA). A schematic of their layer structure is shown in Fig. 6.6. An anti-reflective coating tuned to the laser wavelength is applied.

Quantum efficiency External quantum efficiency (EQE) of the PPC was measured using a Newport IQE-200 system with a 300 W xenon lamp. Specular and diffuse reflectance, R_s and R_d respectively, were measured using the same instrument and internal quantum efficiency was calculated as $IQE = EQE/(1 - R_\mathrm{s} - R_\mathrm{d})$. In this case specular reflectance is nearly zero at the laser wavelength. EQE and IQE are nearly identical except for the small amount of diffuse reflectance due to gridlines.

Simulation of PPCs The simulated IQE results and the coupling factors in Fig. 6.1 were calculated using a drift-diffusion based solver as described in reference [128]. Details of the luminescent coupling calculations are given in reference [111]. An overview of our process for device simulations can be found in reference [56].

Photonic boost converter circuit The circuit uses a RichTek RT9183 linear regulator. It was designed based on recommendations of the manufacturer, with the exception that feedback was provided from the 12 V output of the photonic power converter. Measurements of this circuit and the switching boost converter circuit were made with an Agilent 6014A oscilloscope at 2×10^9 samples/s, with boxcar averaging for improved vertical resolution. Some specific frequencies were identified which were present at consistent levels in all three measurements, as well as in a reference measurement taken with the boost converter powered off. These noise sources are presumed to be internal to the oscilloscope or supporting equipment and the corresponding frequencies are removed from Fig. 6.3d for

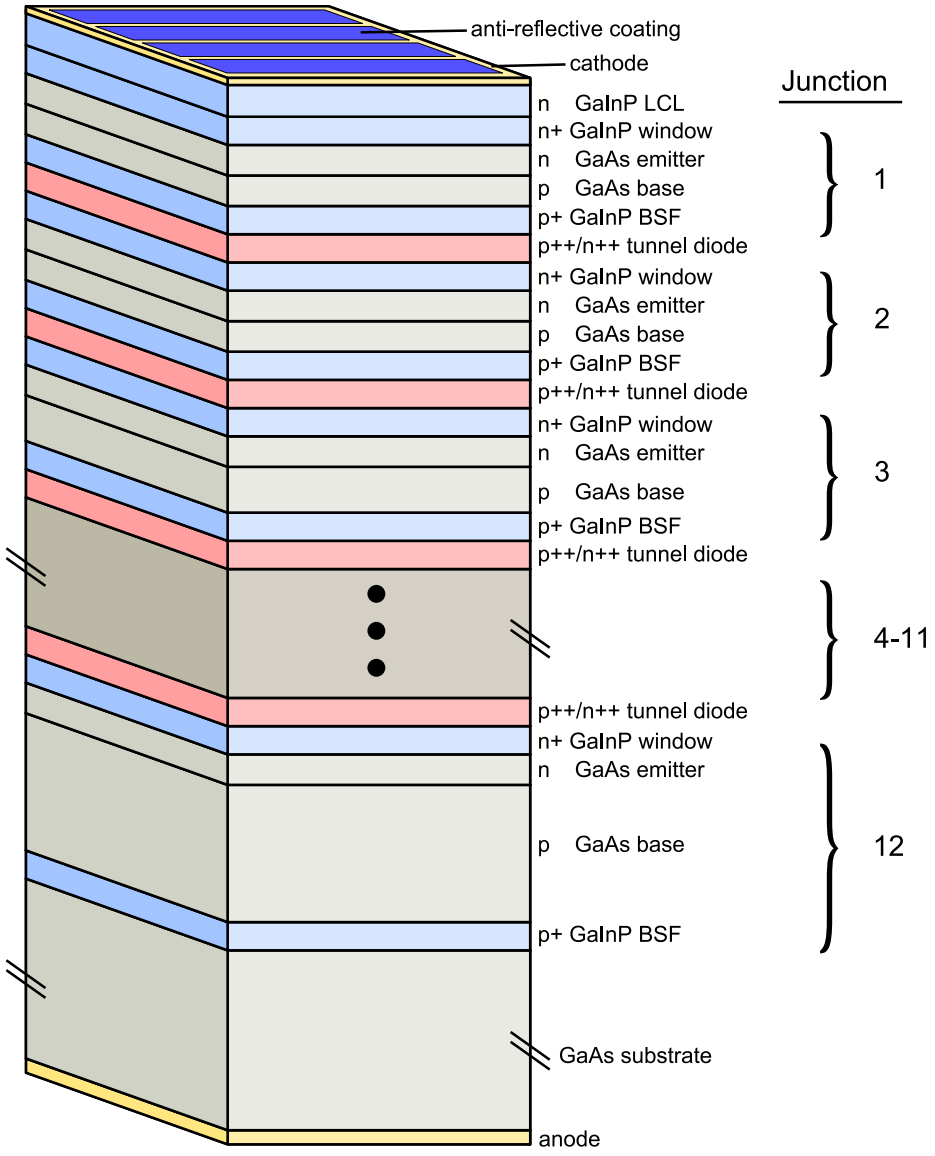

Figure 6.6: Layer structure of the 12-junction PPC.

clarity.

Switching boost converter circuit The switching boost converter is based on a Linear Technologies LT1171 regulator, and again was designed following manufacturer's guidelines for boost converter applications. Switching frequency is 100 kHz. The circuit includes an output L-C filter with a cutoff frequency of 5 kHz.

Gate drive circuit The gate drive application was tested using the half-bridge circuit shown in Fig. 6.4a, with the gate drive signal optocoupler powered using either a conventional DC/DC converter or a photonic power converter (Fig. 6.4b and c respectively.) No gate resistors are used to limit the switching slew rate, which is desirable for high efficiency in power electronic circuits, but leads to harsh switching transients and potential problems with EMI.

The MOSFET is a Cree SiC device with breakdown voltage of 1200 V and 120 A current capability. When the MOSFET Q_1 is turned on for an initial 60 µs, the DC voltage is applied to the load inductor L_1 and the inductor current increases linearly to ~ 90 A. At this point the gate is switched off, on and off again providing switching events to be studied. As Q_1 is switched off, the inductor current freewheels through the diode D_2. The MOSFET is controlled by an optoisolated gate driver with a CMOS totem pole output stage. The optoisolator, in turn, requires an isolated power supply of >13 V.

The transformer-based gate drive power supply (Fig. 6.4b) is based on the Delta SA01S0515A DC/DC converter. For supply voltages V_{DC} >75 V, the stray capacitance of this device is sufficient to cause the SiC MOSFET to fail to turn off because the gate potential cannot rise quickly enough to maintain a positive potential relative to the source terminal. This is addressed by adding a common mode filter F_1 with 200 Ω impedance to common-mode currents at 1 MHz.

Chapter 7

Discussion and Conclusions

The solar power industry has grown dramatically in recent years, from 2.6 GW of installed capacity worldwide in 2007 to 65 GW in 2016 [137]. This has been accompanied by an ongoing drop in the price of traditional non-concentrating silicon photovoltaics and a consolidation of the industry towards that technology. There has been a significant restructuring within the CPV industry, with two of the largest CPV manufacturers, Soitec and Suncore, ceasing production in 2015.

Despite this, CPV projects can be economical in the right circumstances [2]. A single CPV plant with 100 MW capacity has reportedly been completed in Datong, China in 2016 [138] at a cost of US$1.05/W, making it competitive with the US$1.77/W benchmark reported by the National Renewable Energy Laboratory (NREL) [6] for utility-scale PV plants. Interestingly, two Canadian companies, STACE [139] and Morgan Solar [140], have recently announced plans for new CPV production totalling >20 MW per year. This means that a large part of the worldwide CPV module production capacity could soon be based in Canada. In order for CPV technology to remain competitive, and possibly gain a larger share of the market for solar energy systems, efficiency must continue to improve towards a target of 50% at the cell level and 40% at the CPV module level [7, 141].

Efforts to develop multi-junction photovoltaics of any type can benefit greatly from the ability to perform accurate device simulations and to compare the performance of prototype devices against those simulations. The simulation process outlined in chapter 2 enables many different measurable quantities to be compared with experiment, as well as the extraction of many quantities which cannot be directly measured on a solar cell. This chapter should be an excellent starting point for researchers needing to simulate multijunction photovoltaic devices. The technique of plotting all losses in quantum efficiency is particularly useful and can help to identify deficiencies in a particular design.

One of the avenues towards 50% efficient cells that has been identified in the past is the use of dilute nitride materials such as InGaAsN(Sb) to make a 4-junction MJSC [7]. The simulation techniques of chapter 2 were used to design a set of single junction InGaAsN(Sb)cells, as described in chapter 3. Based on this we were able to estimate the material parameters (background doping and diffusion length) present in the dilute nitride material, as well as the performance of a 4-junction structure using these cell designs. Work is continuing on this effort; a set of 4-junction solar cell wafers have been grown by a MOCVD/MBE/MOCVD process and are now in fabrication prior to testing. In order to achieve high performance devices though, there will need to be more optimization of the growth of dilute nitride material specifically for this application, both to maintain crystal quality on a germanium substrate and to achieve the longest possible diffusion lengths.

Several publications in 2012-2014 [24,25,27,120] highlighted the significance of photon recycling and luminescent coupling in the performance of III-V solar cells and the ways in which devices can be optimized if these effects are taken into consideration. However, they also highlighted the fact that virtually all existing tools for drift-diffusion based device simulations neglect these effects. Synopsys Sentaurus does include an option to include photon recycling in LED models, but it is not applicable to solar cells. One effort had been reported previously to include photon recycling in single-junction solar cell simulations, but

the algorithm was not published in detail and the effects were not integrated into the device solver; instead the simulation had to be run numerous times with successive estimates of the coupled optical generation rate.

The methodology detailed in chapter 4 enables these effects to be modeled directly in a commercial device simulator, without any need to for iterative runs of the simulator. It was initially tested with 3- and 4-junction solar cell models as well as single junction cell models. All of the theory needed to implement the model is presented, and there are some improvements in the theory over prior work. The coupling calculations are treated with a modified transfer matrix method which allows for emissions from arbitrary positions within the device. Previous analytical and numerical models had used a mix of ray optics in the emitting region and wave optics in the remaining regions, causing some inaccuracies at the region boundaries.

While the model was very successful, initially no devices were available to us where an experimentally measurable effect could be unequivocally attributed to luminescent coupling. This changed when the first five-junction PPCs were produced by Azastra Opto Inc. in 2014; with five GaAs junctions generating different amounts of photocurrent depending on wavelength, these were an ideal test for the model. The first simulations as shown in chapter 4 were able to reproduce the measured quantum efficiency characteristic, as well as the change in shape depending on material quality. This fit was achieved by varying the internal radiative efficiency of the device (the fraction of radiative vs. total recombination).

We were later able to improve on this result significantly in chapter 5 by using sample devices representing each of the five individual junctions of the 5-junction PPC, to calibrate parameters for each of the recombination processes present in the GaAs material. With this calibration done, we were able to run the simulation and achieve an excellent agreement with experimentally measured quantum efficiency of newly available 12-junction devices, with no fitting required at all and with a much more realistic set of material parameters

compared with what was used in chapter 4. This ability to produce accurate results without fitting is a very important point, as it is an indication of how reliable the simulation can be as predictive and quantitative tool. One further step would be to improve simulations in order to accurately model the 'stepped' shape of some measured PPC *J-V* curves under mismatched illumination. This is due to some junctions being under heavy reverse bias and would require a careful calibration of the reverse breakdown mechanisms in GaAs.

Finally in chapter 6, we studied two applications where PPCs can be used. The new generation of vertically stacked PPCs have 40% (relative) higher efficiency, ten times more optical power density, and up to twice the output voltage of the previous 'pie architecture' technology. In step-up DC/DC conversion, we showed a simple method to provide a step up in voltage from 3 V DC to 12 V while producing no ripple or EMI. We also used a laser/PPC pair to provide the power needed to switch a SiC MOSFET controlling a 650 V, 90 A circuit of the type that is used in hybrid and electric vehicles. Again, this yields a significant reduction in EMI conducted from the high-voltage electronics into the vehicle's signal level analog and digital subsystems.

As the leading technology for high-efficiency photovoltaics, there has been a very large amount of effort devoted to research on multi-junction solar cells over the past 20 years. The new interest in CPV evidenced by projects completed and announced this year is very encouraging, as is the opportunity to put the technology to use in new applications.

Bibliography

[1] Martin A. Green, Keith Emery, Yoshihiro Hishikawa, Wilhelm Warta, and Ewan D. Dunlop. Solar cell efficiency tables (version 48). *Progress in Photovoltaics: Research and Applications*, 24(7):905–913, 2016.

[2] Simon P. Philipps, Andreas W. Bett, Kelsey Horowitz, and Sarah R. Kurtz. Current status of concentrator photovoltaic (CPV) technology. Technical report, Fraunhofer ISE/NREL, 2016.

[3] Gerardo L. Araújo and Antonio Martí. Absolute limiting efficiencies for photovoltaic energy conversion. *Solar Energy Materials and Solar Cells*, 33(2):213–240, 1994.

[4] Jenny Nelson. *Physics of Solar Cells*. Imperial College Press, London, 2003.

[5] Frank Dimroth, Thomas N. D. Tibbits, Markus Niemeyer, Felix Predan, Paul Beutel, Christian Karcher, Eduard Oliva, Gerald Siefer, David Lackner, Peter Fus-Kailuweit, Andreas W. Bett, Rainer Krause, Charlotte Drazek, Eric Guiot, Jocelyne Wasselin, Aurelie Tauzin, and Thomas Signamarcheix. Four-junction wafer-bonded concentrator solar cells. *IEEE Journal of Photovoltaics*, 6(1):343–349, 2016.

[6] Donald Chung, Carolyn Davidson, Ran Fu, Kristen Ardani, and Robert Margolis. U.S. Photovoltaic Prices and Cost Breakdowns: Q1 2015 Benchmarks for Residential, Commercial, and Utility-Scale Systems. Technical Report September, National Renewable Energy Laborator (NREL), 2015.

[7] R. R. King, D. Bhusari, D. Larrabee, X.-Q. Liu, E. Rehder, K. Edmondson, H. Cotal, R. K. Jones, J. H. Ermer, C. M. Fetzer, D. C. Law, and N. H. Karam. Solar cell generations over 40% efficiency. *Progress in Photovoltaics: Research and Applications*, 20(6):801–815, sep 2012.

[8] R. R. King, D. Bhusari, A. Boca, D. Larrabee, X. Liu, W. Hong, C. M. Fetzer, D. C. Law, and N. H. Karam. Band gap-voltage offset and energy production in next-generation multijunction solar cells. *Progress in Photovoltaics: Research and Applications*, 19:797–812, 2011.

[9] Sarah R. Kurtz, P. Faine, and J. M. Olson. Modeling of two-junction, series-connected tandem solar cells using top-cell thickness as an adjustable parameter. *Journal of Applied Physics*, 68(4):1890–1895, 1990.

[10] Angèle Reinders, Pierre Verlinden, Wilfried van Sark, and Alexandre Freundlich. *Photovoltaic Solar Energy: From Fundamentals to Applications*. Wiley, 2017.

[11] Daniel J. Friedman and Sarah R. Kurtz. Breakeven criteria for the GaInNAs junction in GaInP/GaAs/GaInNAs/Ge four-junction solar cells. *Progress in Photovoltaics: Research and Applications*, 10(5):331–344, aug 2002.

[12] David B. Jackrel, Seth R. Bank, Homan B. Yuen, Mark A. Wistey, James S. Harris, Aaron J. Ptak, Steven W. Johnston, Daniel J. Friedman, and Sarah R. Kurtz. Dilute nitride GaInNAs and GaInNAsSb solar cells by molecular beam epitaxy. *Journal of Applied Physics*, 101(11):114916, 2007.

[13] Vijit Sabnis, Homan Yuen, and Mike Wiemer. High-efficiency multijunction solar cells employing dilute nitrides. *8th International Conference on Concentrating Photovoltaic Systems, AIP Conf. Proc.*, 1477(1):14–19, 2012.

[14] Arto Aho. *Dilute nitride multijunction solar cells grown by molecular beam epitaxy*. Ph.d. thesis, Tampere University of Technology, 2015.

[15] Naoya Miyashita, Nazmul Ahsan, Makoto Inagaki, Muhammad Monirul Islam, Masafumi Yamaguchi, and Yoshitaka Okada. High electron mobility in Ga(In)NAs films grown by molecular beam epitaxy. *Applied Physics Letters*, 101(22):222112, 2012.

[16] Naoya Miyashita, Nazmul Ahsan, and Yoshitaka Okada. Generation and collection of photocarriers in dilute nitride GaInNAsSb solar cells. *Progress in Photovoltaics: Research and Applications*, 24:28–37, 2016.

[17] J. A. Gupta, Z. R. Wasilewski, B. J. Riel, J. Ramsey, G. C. Aers, R. L. Williams, G. I. Sproule, A. Perovic, D. D. Perovic, T. Garanzotis, and A. J. SpringThorpe. Compositional control in molecular beam epitaxy growth of GaN_yAs_{1-y} on GaAs (001) using an Ar/N_2 RF plasma. *Journal of Crystal Growth*, 242:141–154, 2002.

[18] J. A. Gupta, G. I. Sproule, X. Wu, and Z. R. Wasilewski. Molecular beam epitaxy growth of 1.55 μm GaInNAs(Sb) double quantum wells with bright and narrow photoluminescence. *Journal of Crystal Growth*, 291(1):86–93, 2006.

[19] Xia Zhang. *Dilute Nitride Long Wavelength Semiconductor Diode Lasers*. PhD thesis, University of Ottawa, 2007.

[20] Simon Fafard, Mark C. A. York, Francine Proulx, Christopher E. Valdivia, Matthew M. Wilkins, Richard Arès, Vincent Aimez, Karin Hinzer, and Denis P.

Masson. Ultrahigh efficiencies in vertical epitaxial heterostructure architectures. *Applied Physics Letters*, 108(7):071101, feb 2016.

[21] Simon Fafard, Francine Proulx, Mark C. A. York, Matthew M. Wilkins, Christopher E. Valdivia, Michal Bajcsy, Dayan Ban, Abdelatif Jaouad, Boussairi Bouzazi, Richard Arès, Vincent Aimez, Karin Hinzer, and Denis P. Masson. Advances with vertical epitaxial heterostructure architecture (VEHSA) phototransducers for optical to electrical power conversion efficiencies exceeding 50 percent. In *Proc. SPIE 9743*, 2016.

[22] Simon Fafard, Francine Proulx, Mark C. A. York, L. S. Richard, Philippe-Olivier Provost, Richard Arès, Vincent Aimez, and Denis P. Masson. High-photovoltage GaAs vertical epitaxial monolithic heterostructures with 20 thin p/n junctions and a conversion efficiency of 60%. *Applied Physics Letters*, 109(13):131107, 2016.

[23] Mico Perales, Mei-huan Yang, Cheng-liang Wu, Chin-wei Hsu, Wei-sheng Chao, Kun-hsien Chen, and Terry Zahuranec. Characterization of high performance silicon-based VMJ PV cells for laser power transmission applications. In *Proc. of SPIE vol. 9733*, page 97330U, 2016.

[24] Daniel J. Friedman, John F. Geisz, and Myles A. Steiner. Analysis of multijunction solar cell current-voltage characteristics in the presence of luminescent coupling. *IEEE Journal of Photovoltaics*, 3(4):1429–1436, 2013.

[25] J. F. Geisz, M. A. Steiner, I. García, S. R. Kurtz, and D. J. Friedman. Enhanced external radiative efficiency for 20.8% efficient single-junction GaInP solar cells. *Applied Physics Letters*, 103(4):041118, 2013.

[26] Myles A. Steiner and John F. Geisz. Non-linear luminescent coupling in series-connected multijunction solar cells. *Applied Physics Letters*, 100(25):251106, 2012.

[27] M. A. Steiner, J. F. Geisz, I. García, D. J. Friedman, A. Duda, and S. R. Kurtz. Optical enhancement of the open-circuit voltage in high quality GaAs solar cells. *Journal of Applied Physics*, 113(12):123109, 2013.

[28] Iván García, John Geisz, Myles Steiner, Jerry Olson, Daniel Friedman, and Sarah Kurtz. Design of Semiconductor-Based Back Reflectors for High V_{oc} Monolithic Multijunction Solar Cells. In *Proceedings of the 37th IEEE Photovoltaic Specialists Conference*, Austin, TX, 2012.

[29] Daniel J. Friedman, John F. Geisz, and Myles A. Steiner. Effect of luminescent coupling on the optimal design of multijunction solar cells. *IEEE Journal of Photovoltaics*, 4(3):986–990, 2014.

[30] Ryan M. France, John F. Geisz, Iván García, Myles A. Steiner, William E. McMahon, Daniel J. Friedman, Tom E. Moriarty, Carl Osterwald, J. Scott Ward, Anna Duda, Michelle Young, and Waldo J. Olavarria. Design flexibility of ultra-high efficiency 4-junction inverted metamorphic solar cells. In *2015 IEEE 42nd Photovoltaics Specialists Conference*, pages 1–3, 2015.

[31] John F. Geisz, Myles A. Steiner, Iván García, Ryan M. France, Daniel J. Friedman, and Sarah R. Kurtz. Implications of redesigned, high-radiative-efficiency GaInP junctions on III-V multijunction concentrator solar cells. *IEEE Journal of Photovoltaics*, 5(1):418–424, 2015.

[32] G. Létay, M. Hermle, and A. W. Bett. Simulating single-junction GaAs solar cells including photon recycling. *Progress in Photovoltaics: Research and Applications*, 14(8):683–696, 2006.

[33] A. W. Walker, O. Höhn, D. N. Micha, L. Wagner, H. Helmers, A. W. Bett, and F. Dimroth. Impact of photon recycling and luminescence coupling on III - V photovoltaic devices. In *Proc. SPIE vol. 9358*, pages 11–13, 2015.

[34] Jieyang Jia, Ferran Suarez, Taner Bilir, Vijit Sabnis, and James Harris. 3-D modeling of luminescent coupling effects in multijunction concentrator solar cells. In *AIP Conference Proceedings*, volume 1616, pages 3–7, 2014.

[35] Jieyang Jia, Yu Miao, Yangsen Kang, Yijie Huo, Mojgan Mazouchi, Yusi Chen, Li Zhao, Huiyang Deng, Pakapol Supaniratisai, Sara H. AlQahtani, and James S. Harris. Bias-dependence of luminescent coupling efficiency in multijunction solar cells. *Optics Express*, 23(7):A219, 2015.

[36] J. Schubert, E. Oliva, F. Dimroth, W. Guter, R. Loeckenhoff, and A. W. Bett. High-voltage GaAs photovoltaic laser power converters. *IEEE Transactions on Electron Devices*, 56(2):170–175, 2009.

[37] S. Kasimir Reichmuth, Henning Helmers, Simon P. Philipps, Michael Schachtner, Gerald Siefer, and Andreas W. Bett. On the temperature dependence of dual-junction laser power converters. *Progress in Photovoltaics: Research and Applications*, 25(1):67–75, 2017.

[38] Lukas Wagner, Andreas W. Bett, and Henning Helmers. On the alignment tolerance of photovoltaic laser power converters. *Optik - International Journal for Light and Electron Optics*, 131:287–291, 2017.

[39] Denis P. Masson, Francine Proulx, and Simon Fafard. Pushing the limits of concentrated photovoltaic solar cell tunnel junctions in novel high-efficiency GaAs phototransducers based on a vertical epitaxial heterostructure architecture. *Progress in Photovoltaics: Research and Applications*, 23(12):1687–1696, 2015.

[40] Francine Proulx, Mark C. A. York, Philippe-Olivier Provost, Richard Arès, Vincent Aimez, Denis P. Masson, and Simon Fafard. Measurement of strong photon recycling in ultra-thin GaAs n/p junctions monolithically integrated in high-photovoltage vertical epitaxial heterostructure architectures with conversion efficiencies exceeding 60%. *Physica Status Solidi - Rapid Research Letters*, 6(November):1–4, 2016.

[41] Sanmeet Chahal, Matthew M. Wilkins, Denis P. Masson, Simon Fafard, Christopher E. Valdivia, and Karin Hinzer. 20-junction photonic power converter performance under non-uniform illumination calculated by 3D distributed circuit model. In *Proc. SPIE Photonics West 2017*, San Francisco, CA, 2017.

[42] Martin A. Green. *Third Generation Photovoltaics*. Springer, Sydney, 2003.

[43] R. R. King, N. H. Karam, J. H. Ermer, N. Haddad, P. Colter, T. Isshiki, H. Yoon, H. L. Cotal, D. E. Joslin, D. D. Krut, R. Sudharsanan, K. Edmondson, B. T. Cavicchi, and D. R. Lillington. Next-generation, high-efficiency III-V multijunction solar cells. In *Conference Record of the Twenty-Eighth IEEE Photovoltaic Specialists Conference*, pages 998–1001, Anchorage, AK, 2000. IEEE.

[44] Jeff Allen, Vijit Sabnis, Mike Wiemer, and Homan Yuen. 44%-efficiency triple-junction solar cells. In *9th International Conference on Photovoltaic Systems (CPV-9), AIP Conf. Proc.*, Miyazaki, Japan, 2013.

[45] Matthew M. Wilkins, Ahmed M. Gabr, Anna H. Trojnar, Henry P. Schriemer, and Karin Hinzer. Effects of luminescent coupling in single- and 4-junction dilute nitride solar cells. In *Proc. of the 40th Photovolt. Spec. Conf.*, pages 6–9, Denver, CO, 2014.

[46] Matthew M. Wilkins, Ahmed M. Gabr, Pratibha Sharma, Henry P. Schriemer, Simon Fafard, and Karin Hinzer. 4-junction solar cells with dilute nitrides: optimization

with luminescent coupling. In *Proceedings of the 29th EU PVSEC*, Amsterdam, NL, 2014.

[47] Daniel J. Friedman and Jerry M. Olson. Analysis of Ge junctions for GaInP/GaAs/Ge three-junction solar cells. *Progress in Photovoltaics: Research and Applications*, 9(3):179–189, may 2001.

[48] D. J. Friedman, J. M. Olson, S. Ward, T. Moriarty, K. Emery, S. R. Kurtz, A. Duda, R. R. King, H. L. Cotal, D. R. Lillington, J. H. Ermer, and N. H. Karam. Ge concentrator cells for III-V multijunction devices. In *Conference Record of the Twenty-Eighth IEEE Photovoltaic Specialists Conference*, pages 965–967. IEEE, 2000.

[49] I. García, C. Algora, I. Rey-Stolle, and B. Galiana. Study of non-uniform light profiles on high concentration III-V solar cells using quasi-3D distributed models. In *2008 33rd IEEE Photovolatic Specialists Conference*, pages 1–6. IEEE, 2008.

[50] Pratibha Sharma, Alexandre W. Walker, Jeffrey F. Wheeldon, Karin Hinzer, and Henry P. Schriemer. Enhanced efficiencies for high concentration, multijunction PV systems by optimizing grid spacing under nonuniform illumination. *International Journal of Photoenergy*, 2014:582083, 2014.

[51] D.L. Scharfetter and H.K. Gummel. Large-signal analysis of a silicon Read diode oscillator. *IEEE Transactions on Electron Devices*, ED-16(1):64–77, jan 1969.

[52] Randolph E Bank, Donald J Rose, and Wolfgang Fichtner. Numerical Methods for Semiconductor Device Simulation. *IEEE Transactions on Electron Devices*, ED-30(9):1031–1041, 1983.

[53] W. Fichtner, D.J. Rose, and R.E. Bank. Semiconductor device simulation. *IEEE Transactions on Electron Devices*, 30(9):1018–1030, sep 1983.

[54] Vassil Palankovski and Rüdiger Quay. *Analysis and Simulation of Heterostructure Devices*. Springer-Verlag, Vienna, 2004.

[55] J. Piprek. *Semiconductor optoelectronic devices: Introduction to physics and simulation*. Academic Press, San Diego, CA, 2003.

[56] Matthew M. Wilkins and Karin Hinzer. Multi-junction Solar Cells. In J. Piprek, editor, *Handbook of Optoelectronic Device Simulation*, chapter 40. Taylor & Francis, 2017.

[57] Synopsys Inc. Simulation of a GaAs / GaInP Dual-Junction Solar Cell, 2012.

[58] Crosslight Software Inc. Application Note: Compound Solar Cells, 2009.

[59] Silvaco Inc. Application Note: EQE of III-V Tandem Cell, 2015.

[60] Tasmiat Rahman and Kristel Fobelets. Efficient tool flow for 3D photovoltaic modelling. *Computer Physics Communications*, 193:124–130, 2015.

[61] W. E. McMahon, J. M. Olson, J. F. Geisz, and D. J. Friedman. An examination of 1D solar cell model limitations using 3D SPICE modeling. In *38th IEEE Photovoltaic Specialists Conference*, pages 002088–002091. IEEE, 2012.

[62] D. E. Aspnes, S. M. Kelso, R. A. Logan, and R. Bhat. Optical properties of $Al_xGa_{1-x}As$. *Journal of Applied Physics*, 60(2):754, 1986.

[63] H. C. Casey, D. D. Sell, and K. W. Wecht. Concentration dependence of the absorption coefficient for n- and p-type GaAs between 1.3 and 1.6 eV. *Journal of Applied Physics*, 46(1):250–257, 1975.

[64] E. F. Schubert. *Physical Foundations of Solid-State Devices*. Rensselaer Polytechnic Institute, 2006.

[65] Aleksandra B. Djurišić, Aleksandar D. Rakić, Paul C. K. Kwok, E. Herbert Li, Marian L. Majewski, and Jovan M. Elazar. Modeling the pptical constants of $Al_xGa_{1-x}As$ alloys. *Journal of Applied Physics*, 86(1):445–451, 1999.

[66] Aleksandra B. Djurišić, Aleksandar D. Rakić, Paul C. K. Kwok, E. Herbert Li, and Martin L. Majewski. Modeling the optical constants of GaP, InP, and InAs. *Journal of Applied Physics*, 85(7):3638–3642, 1999.

[67] A. B. Djurišić, Y. Chan, and E. Herbert Li. The model dielectric function: application to GaSb and InP. *Semiconductor Science and Technology*, 16(11):902–908, 2001.

[68] Hirokazu Kato, Sadao Adachi, Hiroshi Nakanishi, and Kouji Ohtsuka. Optical Properties of $(Al_xGa_{1-x})_{0.5}In_{0.5}P$ Quaternary Alloys. *Japanese Journal of Applied Physics*, 33:186–192, 1994.

[69] Mathias Schubert, J. A. Woollam, G. Leibiger, B. Rheinlander, I. Pietzonka, T. Sab, and V. Gottschalch. Isotropic dielectric functions of highly disordered $Al_xGa_{1-x}InP$ ($0 \leq x \leq 1$) lattice matched to GaAs. *Journal of Applied Physics*, 86(4):2025–2033, 1999.

[70] Aleksandar Rakić, Aleksandra B. Djurišić, Jovan M. Elazar, and Marian L. Majewski. Optical properties of metallic films for vertical-cavity optoelectronic devices. *Applied Optics*, 37(22):5271–5283, 1998.

[71] Aleksandra B. Djurišić, Y. Chan, and E. Herbert Li. Progress in the room-temperature optical functions of semiconductors. *Materials Science and Engineering R*, 38:237–293, 2002.

[72] ASTM International. ASTM G173-03: Standard Tables for Reference Solar Spectral Irradiances: Direct Normal and Hemispherical on 37 degree Tilted Surface. Technical report, ASTM International, 2012.

[73] Pietro P. Altermatt, Jürgen O. Schumacher, Andres Cuevas, Mark J. Kerr, Stefan W. Glunz, Richard R. King, Gernot Heiser, and Andreas Schenk. Numerical modeling of highly doped Si:P emitters based on Fermi-Dirac statistics and self-consistent material parameters. *Journal of Applied Physics*, 92(6):3187, 2002.

[74] Pietro P. Altermatt. Models for numerical device simulations of crystalline silicon solar cells - a review. *Journal of Computational Electronics*, 10(3):314–330, 2011.

[75] Synopsys Inc. *Sentaurus Device User Guide, vK-2015*. Synopsys Inc., 2015.

[76] I. Vurgaftman, J. R. Meyer, and L. R. Ram-Mohan. Band parameters for III-V compound semiconductors and their alloys. *Journal of Applied Physics*, 89(11):5815, 2001.

[77] Irina A. Buyanova and Weimin M. Chen, editors. *Physics and Applications of Dilute Nitrides*. Taylor & Francis, 2004.

[78] J. Wu, W. Shan, and W. Walukiewicz. Band anticrossing in highly mismatched III-V semiconductor alloys. *Semiconductor Science and Technology*, 17(8):860–869, 2002.

[79] I. Vurgaftman and J. R. Meyer. Band parameters for nitrogen-containing semiconductors. *Journal of Applied Physics*, 94(6):3675, 2003.

[80] Guido Masetti, Maurizio Severi, and Sandro Solmi. Modeling of carrier mobility against carrier concentration in arsenic-doped, phosphorus-doped, and boron-doped silicon. *IEEE Transactions on Electron Devices*, ED-30(7):764–769, 1983.

[81] Narain D. Arora, John R. Hauser, and David J. Roulston. Electron and hole mobilities in silicon as a function of concentration and temperature. *IEEE Transactions on Electron Devices*, ED-29(2):292–295, 1982.

[82] Dietmar Schroeder. *Modelling of Interface Carrier Transport for Device Simulation*. Springer-Verlag, Wien, 1994.

[83] S. R. Kurtz, J. M. Olson, D. J. Friedman, J. F. Geisz, A. E. Kibbler, and K. A. Bertness. Passivation of Interfaces in High-Efficiency Photovoltaic Devices. In *Materials Research Society Spring Meeting*. NREL, 1999.

[84] Wolfgang Guter and Andreas W. Bett. IV-Characterization of devices consisting of solar cells and tunnel diodes. In *IEEE 4th World Conference on Photovoltaic Energy Conversion*, pages 749–752. IEEE, 2006.

[85] S. M. Sze and Kwok K. Ng. *Physics of Semiconductor Devices*. Wiley-Interscience, Hoboken, NJ, 3rd edition, 2007.

[86] Alex W. Walker, Olivier Thériault, Matthew M. Wilkins, Jeffrey F. Wheeldon, and Karin Hinzer. Tunnel-junction-limited multijunction solar cell performance over concentration. *IEEE Journal of Selected Topics in Quantum Electronics*, 19(5):4000508, 2013.

[87] Jeffrey F. Wheeldon, Christopher E. Valdivia, Alexandre W. Walker, Gitanjali Kolhatkar, Abdelatif Jaouad, Artur Turala, Bruno Riel, Denis P. Masson, Norbert Puetz, Simon Fafard, Richard Arès, Vincent Aimez, Trevor J. Hall, and Karin Hinzer. Performance comparison of AlGaAs, GaAs and InGaP tunnel junctions for concentrated multijunction solar cells. *Progress in Photovoltaics: Research and Applications*, 19(4):442–452, 2010.

[88] S. P. Philipps, M. Hermle, G. Létay, and W. Guter. Numerical simulation and modeling of III-V multi-junction solar cells. In *23rd European Photovoltaic Solar Energy Conference*, pages 1–5, Valencia, Spain, 2008.

[89] Kazushige Horio and Hisayoshi Yanai. Numerical modeling of heterojunctions including the thermionic emission mechanism at the heterojunction interface. *IEEE Transactions on Electron Devices*, 37(4):1093–1098, 1990.

[90] K. Emery, M. Meusel, R. Beckert, F. Dimroth, A. W. Bett, and W. Warta. Procedures for evaluating multijunction concentrators. In *Conference Record of the Twenty-Eighth IEEE Photovoltaic Specialists Conference*, pages 1126–1130. IEEE, 2000.

[91] Sadao Adachi. *Optical Constants of Crystalline and Amorphous Semiconductors*. Springer US, Boston, MA, 1999.

[92] Edward D. Palik, editor. *Handbook of Optical Constants of Solids*. Academic Press, 1998.

[93] M. Levinshtein, S. Rumyantsev, and M. Shur, editors. *Handbook Series on Semiconductor Parameters, vol. 2: Ternary And Quaternary III-V Compounds*. World Scientific, 1999.

[94] M. Sotoodeh, A. H. Khalid, and A. A. Rezazadeh. Empirical low-field mobility model for III-V compounds applicable in device simulation codes. *Journal of Applied Physics*, 87(6):2890, 2000.

[95] John Fontanella, Carl Andeen, and Donald Schuele. Low-frequency dielectric constants of α-quartz, sapphire, MgF_2, and MgO. *Journal of Applied Physics*, 45(7):2852–2854, 1974.

[96] D. R. Lide, editor. *CRC Handbook of Chemistry and Physics*. CRC Press, 86th edition, 2005.

[97] Jesus M. Siqueiros, Roberto Machorro, and Luis E. Regalado. Determination of the optical constants of MgF_2 and ZnS from spectrophotometric measurements and the classical oscillator method. *Applied optics*, 27(12):2549–2553, 1988.

[98] J. R. Devore. Refractive indices of rutile and sphalerite. *Journal of the Optical Society of America*, 41(6):416, 1951.

[99] Jan Kischkat, Sven Peters, Bernd Gruska, Mykhaylo Semtsiv, Mikaela Chashnikova, Matthias Klinkmüller, Oliana Fedosenko, Stephan Machulik, Anna Aleksandrova, Gregorii Monastyrskyi, Yuri Flores, and W. Ted Masselink. Mid-infrared optical properties of thin films of aluminum oxide, titanium dioxide, silicon dioxide, aluminum nitride, and silicon nitride. *Appl. Opt.*, 51(28):6789–6798, 2012.

[100] S. Fahy and E. P. O'Reilly. Intrinsic limits on electron mobility in dilute nitride semiconductors. *Applied Physics Letters*, 83(18):3731–3733, 2003.

[101] Antti Tukiainen, Arto Aho, Gabriele Gori, Ville Polojärvi, Mariacristina Casale, Erminio Greco, Riku Isoaho, Timo Aho, Marianna Raappana, Roberta Campesato, and Mircea Guina. High-efficiency GaInP/GaAs/GaInNAs solar cells grown by combined MBE-MOCVD technique. *Progress in Photovoltaics: Research and Applications*, 24(7):914–919, jul 2016.

[102] Matthew M. Wilkins, Alexandre W. Walker, Jeffrey F. Wheeldon, Gilbert Arbez, Henry P. Schriemer, and Karin Hinzer. Design constraints of *n-p* InGaAsN dilute nitride sub-cells for 3- and 4- junction solar cell applications under concentrated illumination. In *Proceedings of the 39th IEEE Photovoltaics Specialists Conference*, Tampa, 2013.

[103] Gilbert Arbez, Alexandre W. Walker, Matthew M. Wilkins, Jeffrey F. Wheeldon, Robert Li, Anna H. Trojnar, Karin Hinzer, and H. P. Schriemer. 4 Junction dilute nitride solar cell optimization: Comparing current matching approaches in detailed balance algorithms. In *Proceedings of the 39th Photovoltaic Specialists Conference*, Tampa, FL, 2013.

[104] Sarah R. Kurtz, Richard R. King, Daniel Law, Aaron Ptak, John Geisz, and Nasser H. Karam. Effects of *in situ* annealing on GaInNAs solar cells. In *Proceedings of the 39th Photovoltaic Specialists Conference*, 2013.

[105] A. J. Ptak, R. France, C.-S. Jiang, and R. C. Reedy. Effects of bismuth on wide-depletion-width GaInNAs solar cells. *Journal of Vacuum Science & Technology B: Microelectronics and Nanometer Structures*, 26(3):1053–1057, 2008.

[106] A. J. Ptak, D. J. Friedman, S. R. Kurtz, R. C. Reedy, M. Young, D. B. Jackrel, H. B. Yuen, S. R. Bank, M. A. Wistey, and J. S. Harris. Calcium impurities in enhanced-depletion-width GaInNAs grown by molecular-beam epitaxy. *Journal of Vacuum Science & Technology B: Microelectronics and Nanometer Structures*, 24(3):1540, 2006.

[107] Sarah R. Kurtz, J. F. Geisz, D. J. Friedman, J. M. Olson, A. Duda, N. H. Karam, R. R. King, J. H. Ermer, and D. E. Joslin. Modeling of electron diffusion length in GalnAsN solar cells. In *Conference Record of the Twenty-Eighth IEEE Photovoltaic Specialists Conference*, pages 1210–1213, 2000.

[108] Daniel Derkacs, D. Taner Bilir, and Vijit A. Sabnis. Luminescent coupling in GaAs/GaInNAsSb multijunction solar cells. *IEEE Journal of Photovoltaics*, 3(1):520–527, 2013.

[109] M. Wolf. Drift fields in photovoltaic solar energy converter cells. *Proceedings of the IEEE*, 51(5):674–693, 1963.

[110] A. J. Ptak, D. J. Friedman, and Sarah Kurtz. Effects of temperature, nitrogen ions, and antimony on wide depletion width GaInNAs. *Journal of Vacuum Science & Technology B: Microelectronics and Nanometer Structures*, 25(3):955, 2007.

[111] Matthew M. Wilkins, Christopher E. Valdivia, Ahmed M. Gabr, Denis P. Masson, Simon Fafard, and Karin Hinzer. Luminescent coupling in planar opto-electronic devices. *Journal of Applied Physics*, 118(14):143102, 2015.

[112] Myles A. Steiner, John F. Geisz, Daniel J. Friedman, Anna Duda, Waldo J. Olavarria, Michelle Young, Darius Kuciauskas, and Sarah R. Kurtz. Effects of internal luminescence and internal optics on V_{oc} and J_{sc} of III-V solar cells. *IEEE Journal of Photovoltaics*, 3(4):1437–1442, 2013.

[113] M. A. Steiner, J. F. Geisz, T. E. Moriarty, R. M. France, W. E. McMahon, J. M. Olson, S. R. Kurtz, and D. J. Friedman. Measuring IV curves and subcell photocurrents in the presence of luminescent coupling. *IEEE Journal of Photovoltaics*, 3(2):879–887, 2013.

[114] G. Létay, M. Breselge, and A. W. Bett. Calculating the generation function of III-V solar cells. In *3rd World Conference on Photovoltaic Energy Conversion*, pages 741–744, 2003.

[115] J. L. Balenzategui and A. Martí. Detailed modelling of photon recycling: Application to GaAs solar cells. *Solar Energy Materials and Solar Cells*, 90(7-8):1068–1088, 2006.

[116] Wei-Choon Ng and Gergö Létay. A generalized 2D and 3D white LED device simulator integrating photon recycling and luminescent spectral conversion effects. In *Proceedings of SPIE*, volume 6486, pages 1–10, 2007.

[117] Joachim Piprek, editor. *Optoelectronic Devices: Advanced Simulation and Analysis*. Springer, New York, 2006.

[118] Christopher E. Valdivia, Matthew M. Wilkins, Boussairi Bouzazi, Abdelatif Jaouad, Vincent Aimez, Richard Arès, Denis P. Masson, Simon Fafard, and Karin Hinzer. Five-volt vertically-stacked, single-cell GaAs photonic power converter. In Alexandre Freundlich, Jean-François Guillemoles, and Masakazu Sugiyama, editors, *Proc. SPIE 9358*, volume 9358, page 93580E, 2015.

[119] J. G. Fossum, R. P. Mertens, D. S. Lee, and J. F. Nijs. Carrier recombination and lifetime in highly doped silicon. *Solid-State Electronics*, 26(6):569–576, 1983.

[120] Owen D. Miller, Eli Yablonovitch, and Sarah R. Kurtz. Strong internal and external luminescence as solar cells approach the Shockley-Queisser limit. *IEEE Journal of Photovoltaics*, 2(3):303–311, July 2012.

[121] S. Orfanidis. *Electromagnetic Waves and Antennas*. Rutgers University, 2010.

[122] Steve J. Byrnes. TMM library manual v0.1.2. Technical report, 2012.

[123] Rohm Semiconductor Co. Ltd. SiC Power Devices and Modules. Technical Report August, 2014.

[124] Mark C. A. York, Francine Proulx, Denis P. Masson, Abdelatif Jaouad, Boussairi Bouzazi, Richard Arès, Vincent Aimez, and Simon Fafard. Thin n/p GaAs junctions for novel high-efficiency phototransducers based on a vertical epitaxial heterostructure architecture. *MRS Advances*, pages 1–10, 2016.

[125] J. E. Parrott. Radiative recombination and photon recycling in photovoltaic solar cells. *Solar Energy Materials and Solar Cells*, 30(3):221–231, 1993.

[126] Rafael Peña, Carlos Algora, and Ignacio Anton. GaAs multiple photovoltaic converters with and efficiency of 45% for monochromatic illumination. In *IEEE 3rd World Conference on Photovoltaic Energy Conversion*, pages 228–231, Osaka, Japan, 2003.

[127] Rafael Peña and Carlos Algora. One-watt fiber-based power-by-light system for satellite applications. *Progress in Photovoltaics: Research and Applications*, 20(1):117–123, 2012.

[128] Matthew M. Wilkins, Christopher E. Valdivia, Sanmeet Chahal, Masanori Ishigaki, Denis P. Masson, Simon Fafard, and Karin Hinzer. Performance impact of luminescent coupling on monolithic 12-junction phototransducers for 12 V photonic power systems. In *Proc. SPIE vol. 9743*, San Francisco, CA, 2016.

[129] Jacek Rabkowski, Dimosthenis Peftitsis, and Hans-Peter Nee. Silicon carbide power transistors: A new era in power electronics is initiated. *IEEE Industrial Electronics Magazine*, 6(2):17–26, 2012.

[130] Juergen Biela, Mario Schweizer, Stefan Waffler, and Johann W. Kolar. SiC versus Si - Evaluation of potentials for performance improvement of inverter and DC-DC converter systems by SiC power semiconductors. *IEEE Transactions on Industrial Electronics*, 58(7):2872–2882, 2011.

[131] Hans-Peter Nee, Johann W. Kolar, Peter Friedrichs, and Jacek Rabkowski. Editorial: Special Issue on Wide Bandgap Power Devices and Their Applications, 2014. *IEEE Transactions on Power Electronics*, 29(5):2153–2154, 2014.

[132] Jacek Rabkowski. Power Converters with Silicon Carbide Devices. In *14th Biennial Baltic Electronics Conference (BEC2014)*, pages 7–16, Tallinn, Estonia, 2014.

[133] Alexander Anthon, Zhe Zhang, and Michael A. E. Andersen. Comparison of a state of the art Si IGBT and next generation fast switching devices in a 4 kW boost converter. In *2015 IEEE Energy Conversion Congress and Exposition (ECCE)*, pages 3003–3011. IEEE, sep 2015.

[134] Helong Li and Munk Nielsen Stig. Challenges in switching SiC MOSFET without ringing. In *PCIM Europe Conference Proceedings*, pages 989–994, Nuremberg, 2014.

[135] B. Callanan. SiC MOSFET Double Pulse Fixture. Technical Report February, Cree, Inc., 2011.

[136] Christina DiMarino, Zheng Chen, Milisav Danilovic, Dushan Boroyevich, Rolando Burgos, and Paolo Mattavelli. High-temperature characterization and comparison of 1.2 kV SiC power MOSFETs. In *2013 IEEE Energy Conversion Congress and Exposition, ECCE*, pages 3235–3242, 2013.

[137] Junko Movellan. The 2016 Global PV Outlook : US, Asian Markets Strengthened by Policies to Reduce CO2. *Renewable Energy World*, pages 1–7, 2016.

[138] Brian Publicover. United Photovoltaics completes 100MW CPV plant for state pilot in China. *RECHARGE*, page 1, 2016.

[139] Mariyana Yaneva. Canadian STACE buys solar business of French Soitec - report. *SeeNews Renewables*, pages 1–2, 2016.

[140] Tyler Hamilton. Morgan Solar, One of the Last Remaining Concentrating PV Firms, Wins 10MW Project. *Greentech Media*, 2016.

[141] Daniel J. Friedman, Richard R. King, Richard M. Swanson, Jennifer McJannet, and Don Gwinner. Editorial: Toward 100 Gigawatts of Concentrator Photovoltaics by 2030. *IEEE Journal of Photovoltaics*, 3(4):1460–1463, 2013.